UNIVERSIDADE
BEIRA INTERIOR

Experimental Analysis of the Discharge and Flow Coefficients of a Multi-valve Internal Combustion Engine

Simão Tiago Livramento Henriques

Dissertação para obtenção do Grau de Mestre em
Engenharia Aeronáutica
(Ciclo de estudos integrado)

Orientador: Prof. Doutor Francisco Miguel Ribeiro Proença Brójo

Abril de 2020

Dedication

To my parents, Agostinho and Cesaltina, and my sister, Daniela.

”Learn from yesterday, live for today, hope for tomorrow.
The important thing is not to stop questioning”

Albert Einstein

Acknowledgements

The realization of this dissertation was an ongoing challenge for me since the work involved a lot of practical habits that I was not used to and a huge dedication as well as patience to overcome the problems that came along. This work could not be accomplished without the guidance, support, and encouragement of some important persons which I will always be grateful for.

To Professor Francisco Brójo, my project supervisor, a special thank you for providing me the required materials and equipment to carry on the experiment and your guidance over the most difficult and critical moments which powered me back again to the right path. Furthermore, I also would like to appreciate your availability, wise suggestions and the teaching of some practical techniques which I certainly will be using in the future.

My deepest thank to Sr. Rui Paulo, Dr. João Correia, Dr. Nuno Sérgio and the technician João for every advice, support, and transmitted knowledge over the most varied areas, since wood structures, engine disassembly and welding techniques to the manufacturing of 3d pieces, stepper motor basics, and tinning of wires.

I also would like to thank my friends, Miguel Duarte, Emanuel Camacho, Emanuel Castanho and Hugo Rocha for their support and encouragement throughout the work. Without them, it would be extremely hard to ever finish the proposed work, therefore, a huge thank you guys.

Last but not least, I want to thank my family for their support and encouragement words in the course of the dissertation. In particular, to my parents who always believed in me and made this possible.

Resumo

A procura de novas formas de reduzir emissões e o consumo de combustíveis fósseis em todo o mundo tornou-se mais urgente que nunca, uma vez que o principal desafio do século atual é apontado como sendo as alterações climáticas. Os motores de combustão interna são responsáveis por grande parte das emissões emitidas e, por este motivo, tem vindo a ser feita uma procura constante a fim de se conseguir obter uma melhor eficiência nos motores. A solução para alcançar um melhor desempenho de motor pode estar no estudo do fluxo de ar a atravessar o sistema de admissão uma vez que, através deste estudo, vários fatores e fenómenos que limitam significativamente a respirabilidade do motor, e consequentemente, a sua eficiência são identificados. O conjunto porta-válvula é o local do sistema de admissão que mais restringe o fluxo de ar, deste modo, este desempenha um papel importante ao permitir que o caudal de ar na admissão seja admitido pelo cilindro. A fim de medir a eficiência do processo de indução, coeficientes de descarga e fluxo são definidos e investigados sob diferentes condições de entrada. Neste sentido, foi realizada uma investigação experimental com o objetivo de estudar a respirabilidade de um motor de ignição por faísca com múltiplas válvulas por cilindro durante o processo de admissão. Este estudo foi realizado no laboratório de Propulsão da Universidade da Beira Interior. Para tal, o efeito de adicionar um corpo de borboleta ao sistema de admissão e desativar uma válvula de admissão são analisados em condições estáticas e dinâmicas. Foram testados quatro ângulos de acelerador: 30, 50, 70, e 90º, bem como uma configuração sem borboleta de admissão. Os testes experimentais foram conduzidos num banco de ensaios estático/dinâmico em termos de coeficientes de descarga e fluxo adimensionais, a fim de compreender se o desempenho dinâmico do conjunto porta-válvula pode ser previsto através de coeficientes de descarga e fluxo estáticos. Ao longo dos testes, a queda de pressão foi mantida constante a 13 kPa e o levantamento da válvula variou entre 0.5 mm a 8.4 mm. Durante cada medição, o caudal de ar, a temperatura de admissão, a pressão a montante da válvula e a pressão a jusante da mesma foram registadas. A investigação realça a influência do levantamento da válvula na respirabilidade do motor. Além disso, demonstra que a adição de um corpo de borboleta ao sistema de admissão resulta numa redução da capacidade de admitir ar por parte do motor em comparação à configuração sem borboleta. Este estudo também evidência que a desativação de uma válvula, em motores com duas válvulas de admissão por cilindro, tem como resultado a obtenção de maiores coeficientes de descarga, enquanto que a configuração de duas válvulas resulta em coeficientes de fluxo mais elevados. O impacto da velocidade da árvore de cames na respirabilidade do motor é avaliado em termos de coeficientes de descarga e fluxo médios. Os resultados mostram que os coeficientes de descarga e fluxo diminuem ligeiramente à medida que a velocidade da árvore de cames aumenta. No geral, foi alcançada uma boa concordância entre os resultados estáticos e os dinâmicos, provando que os coeficientes estáticos podem prever com uma boa precisão o comportamento dinâmico da porta e da válvula de admissão.

Palavras-chave

Motor de combustão interna, Sistema de admissão, Coeficiente de descarga, Coeficiente de fluxo, Caudal de ar.

Abstract

The search for newer ways to reduce emissions and fossil fuel consumption worldwide has become more urgent than ever since climate change was identified as the main challenge of the current century. Internal Combustion Engines (ICEs) are responsible for a large portion of emissions and, for this reason, a constant search for engine efficiency improvement has been made. The key to achieve an improved engine performance might be lying in the study of the airflow across the intake system since several factors and phenomena which considerably limit engine breathing and efficiency are identified. Being the major inlet flow restriction, the port-valve assembly plays an important role in allowing the airflow to be drawn into the cylinder. In order to measure how efficient the induction process is, discharge and flow coefficients are defined and investigated under different intake conditions. In this sense, an experimental investigation aiming at the study of the fluid dynamic efficiency of a multi-valve Spark-Ignition (SI) engine during the induction stroke was carried out at the Propulsion laboratory of the University of Beira Interior (UBI). To this purpose, the effect of adding a throttle body to the inlet system and deactivating one inlet valve are analysed under static and dynamic conditions. Four throttle plate angles: 30, 50, 70, and 90º were tested along with an inlet configuration without a throttle plate. The experimental tests were conducted at a steady/unsteady flow rig in terms of dimensionless discharge and flow coefficients, in order to understand if the dynamic performance of the port-valve assembly can be predicted through steady discharge and flow coefficients. Throughout the tests, the pressure drop was kept constant at 13 kPa and the valve lift varied from 0.5 mm to 8.4 mm. During each measurement, the air mass flow, inlet temperature, valve upstream pressure and cylinder pressure are registered. The investigation highlights the influence of valve lift on engine breathing. Moreover, it demonstrates that adding a throttle body into the inlet system will result in reduced engine breathability in comparison to a configuration without a throttle plate. This study also indicates that deactivating one inlet valve, in multi-valve engines, leads to higher discharge coefficients, while the conventional configuration results in higher flow coefficients. The impact of the camshaft velocity on engine breathing is evaluated in terms of mean discharge and flow coefficients. The research shows that the discharge and flow coefficients decrease slightly as the camshaft velocity increases. Overall, a good agreement between static and dynamic results was achieved, proving that steady coefficients can predict with good accuracy the unsteady behaviour of the intake port and valve.

Keywords

Internal combustion engine, Intake system, Discharge coefficient, Flow coefficient, Airflow.

Contents

List of Figures

List of Tables

List of Acronyms

ABDC	After Bottom Dead Center
ATDC	After Top Dead Center
BBDC	Before Bottom Dead Center
BDC	Bottom Dead Center
BTDC	Before Top Dead Center
CAD	Computed-Aided Design
CI	Compression-Ignition
EVC	Exhaust Valve Closing
EVO	Exhaust Valve Opening
ICE	Internal Combustion Engine
IVO	Intake Valve Opening
IVC	Intake Valve Closing
LDA	Laser Doppler Anemometry
MAF	Mass Air Flow
MAP	Manifold Absolute Pressure
OHC	Overhead Camshaft
OHV	Overhead Valve
PET	Polyethylene Terephthalate
PLA	Polylactic Acid
PVC	Polyvinyl Chloride
RR	Rolls-Royce
SI	Spark-Ignition
TDC	Top Dead Center
TIG	Tungsten Inert Gas
UBI	University of Beira Interior
USB	Universal Serial Bus
VVT	Variable Valve Timing
WOT	Wide Open Throttle
WWI	World War One

Nomenclature

η_v	Volumetric efficiency	[$-$]
$\dot{m}_a$	Air mass flow rate	[kg/s]
ρ_{int}	Intake air density	[kg/m^3]
V_d	Displacement volume	[m^3]
N	Engine speed	[rps]
p_{int}	Air intake pressure	[Pa]
R_{air}	Gas constant for dry air	[J/kgK]
T_{int}	Air intake temperature	[K]
Re	Reynolds number	[$-$]
U	Airflow velocity	[m/s]
D_p	Inlet pipe diameter	[m]
μ	Dynamic viscosity of the fluid	[$N.s/m^2$]
D	Valve head diameter	[m]
L_v	Valve lift	[m]
w	Valve seat width	[m]
β	Valve seat angle	[$\circ$]
D_{is}	Inner seat diameter	[m]
D_s	Valve stem diameter	[m]
C_d	Discharge coefficient	[$-$]
$\dot{m}_{act}$	Actual mass flow rate	[kg/s]
$\dot{m}_i$	Ideal mass flow rate	[kg/s]
$C_{d_{exp}}$	Experimental discharge coefficient	[$-$]
A_r	Reference area	[m^2]
p_0	Pressure upstream the inlet valve	[Pa]
p_c	Cylinder pressure	[Pa]
γ	Specific heat ratio	[$-$]
$C_{d_{chok}}$	Experimental discharge coefficient under choking conditions	[$-$]
A_c	Valve curtain area	[m^2]
A_s	Valve seat area	[m^2]
A_e	Valve effective flow area	[m^2]
$C_{f_{exp}}$	Experimental flow coefficient	[$-$]
y_f	Filter value	[kg/s]
α	Damping coefficient	[$-$]
β_f	Filter constant	[$-$]
T	Filter response time	[$-$]
K	Filter gain	[$-$]
y_s	Signal value	[kg/s]
$C_{d_{mean}}$	Average discharge coefficient	[$-$]
$C_{f_{mean}}$	Mean flow coefficient	[$-$]
α_{IVC}	Cam IVC angle	[$\circ$]
α_{IVO}	Cam IVO angle	[$\circ$]

s	Standard deviation	[−]
x_i	Certain measurement	[−]
$\bar{x}$	Measurements average	[−]
N_{sensor}	Number of measurements	[−]
$\sigma_{\bar{x}}$	Standard deviation of the mean	[−]

Chapter 1

Introduction

1.1 Motivation

Nowadays, emissions from burned fossil fuels and coal increase by each year, leading to the rise of greenhouse gases which contribute to the meltdown of polar ice caps and climate change. These two serious problems will have a large effect on people's lives since the latter can decrease the food availability, which might result in food shortage and the former will increase the average level of seawater, leading to the flooding of coastal cities and the disappearance of islands. Therefore, it becomes urgent to study ways of reducing as much as possible emissions and fuel consumption in piston engines.

Even though ICEs are responsible for a considerable portion of those emissions, the use of this kind of engines transformed and made our lives easier by doing most of the heavy lifting and enabling humankind to fly and move across vast distances in a short period of time. In order to counteract this emissions trend, this dissertation focus on the study of the fluid dynamic efficiency of alternative ICEs during the intake stroke since some reduction in both fuel consumption and emissions along with an improvement in engine performance can be attained by optimizing the intake phase [1].

Piston engines have always been used in the automotive and aviation industry, especially in propeller-powered air vehicles, representing the majority of engines used today. Since its beginning, these engines have been developed and improved to meet emissions requirements in order to reduce their environmental impact. However, these emissions obligations set by legislation become increasingly restrictive as the global concern for pollution increases, leaving a low margin for performance and emissions improvements to engine builders. To make the most of this narrow range of improvement, it is important to understand the principles of operation of these engines and to find relationships among the most dominant engine performance parameters which allow the optimization of engine efficiency, emissions, and fuel consumption.

The study of how the air is drawn into the cylinder, in particular, the interaction between the airflow, the surfaces of the valves and the intake duct walls, allows to identify factors that significantly limit engine performance and reduce their influence throughout the intake procedure, optimizing the combustion process, leading to greater engine efficiency and power together with fewer emissions and lower fuel consumption. The design and sizing of the intake manifold, port, and valve emerge as a solution to counteract the negative effects of these limitations, as they control the airflow or the air-fuel mixture that gets in the cylinder and contributes to the production of power. In this sense, it is interesting to investigate the behaviour of discharge and flow coefficients at various engine rotations and valve lifts in several engines, in order to find the conditions under which these coefficients are maximized and evaluate different valve strategies which according to some experimental studies may improve engine efficiency.

1.2 Main Goals

The present dissertation focuses on the experimental determination and analysis of the discharge and flow coefficients of a multi-valve engine. This way, the impact of intake valve motion in the performance and efficiency of alternative ICEs can be known and studied. Furthermore, it is aimed to evaluate both previous parameters for three different intake valve lifts strategies: standard (both intake valves open), deactivated (only one inlet valve open) and asymmetric (both inlet valves open with 10º of difference from each other), in order to assess which camshaft setting provides more advantages in terms of efficiency.

For each camshaft configuration, a throttle plate is added to the inlet system in order to study the effect of several throttle plate angles on the engine breathability. Besides that, a clean configuration (without any airflow blockage) is also investigated to compare an engine with carburettor and a Compression-Ignition (CI) engine in terms of engine breathing.

It is planned to perform tests under steady and unsteady conditions to compare the differences between discharge and flow coefficients obtained in a motionless and a real engine operating condition. In addition, it is aimed to study the influence of suction pressure on the discharge and flow coefficient for the different throttle plate and valve lift configurations.

To this purpose, it is intended to design and build a test bench, capable of providing trustable discharge and flow coefficient values under both test conditions and for the different valve and inlet configurations. The desired parameters are determined through a set of sensors placed on the inlet system and engine block together with an electric motor. As a secondary goal, it is aimed to design and build a custom power supply to power the motor and assist in future works.

In order to better understand the inlet flow behaviour over the entire inlet system, especially at the inlet port and valve, as well as the factors which affect the flow, it is required to gather information about the principles which rule the intake flow through the port-valve assembly. This way, the results obtained can be compared to the literature. Since this work focuses mostly in the intake stroke of piston engines, an enhanced understanding of the operation principles of piston engines is a must.

As a final goal, this work also intends to test several engines and various intake valves so that several discharge and flow coefficients can be determined and registered in a database. Thus, this database can be used in a valve sizing program for ICEs in order to provide an easier way to know the study parameters for a given valve or engine.

1.3 Document Overview

The entire document is divided into 6 main chapters. Each one is dedicated to different contents involved in this work.

The current chapter presents the motivation behind the development of this work, as well as the objectives that the author intends to achieve with this dissertation.

The second chapter summarizes the main principles and concepts of ICEs. It starts by making a historical review of piston engines, where the major breakthroughs achieved during the development of alternative ICEs are highlighted. Furthermore, the operating and theoretical cycles associated with these engines are also discussed in order to better understand the principles behind piston engines.

The third chapter comprehends the theoretical concepts regarding the airflow flowing over the intake system, giving a special focus to the port-valve assembly. Besides that, the main factors which affect engine breathability are discussed and the major characteristics of valve systems are reviewed. At the end of the chapter, several studies related to this work are presented to identify the behaviour of the discharge and flow coefficients under different conditions and allow an improved design of ports and valves.

The fourth chapter describes the entire procedure involved in the manufacture and assembly of the required components and exposes the different problems found which resulted in constant modifications.

The fifth chapter presents a summarized description of the experimental work, as well as the connections and location of sensors and the electrical motor in the experimental apparatus. In addition, it comprehends the results obtained and their discussion.

The final chapter makes a general overview of the work, highlighting the accomplished objectives along with the conclusions achieved from the obtained results. In order to continue this type of study, it is also presented several future work proposals.

Chapter 2

Internal combustion engine basics

This chapter begins with the historical development of internal combustion engines, where the major breakthroughs related to this kind of engines in the aviation industry are highlighted. Followed the historical context, it is shown how engines can be classified according to several features. Lastly, the main theoretical contents regarding piston engines such as the operating cycles and the ideal cycles are presented, where more focus is given to the four-stroke working cycle and the idealized spark ignition cycle.

2.0.1 History

The origin of the ICE is quite hard or perhaps impossible to pinpoint, however, it seems that the experiments of Christiaan Huygens with gunpowder engines, in the early 17th century, were the first sign that someone had approached a working engine [2]. In his engine, the cylinder, closed by a free piston, had a combustion chamber at its lower end where the gunpowder and air stood. Once the ignition process starts, the piston moves to the top of the cylinder, uncovering exhaust ports and allowing combustion gases to escape. Seconds later, the piston goes downwards due to its own weight and to the cooling of the residual gases [2].

Prior to about the middle of the 19th century, with the unfolding of the industrial revolution, external combustion engines like the steam engines and hot air engines, began to be widely used, leading to the forgetfulness of ICEs [3]. In this kind of engines, high pressure is admitted into a reciprocating piston-cylinder assembly and as the steam expands to lower pressure, part of the thermal energy is transformed into work transmitted to the piston. The piston movement is then converted into rotary motion by a crankshaft system resulting in engine work.

Steam engines were suggested to power aeroplanes after being successfully implemented in ships, locomotives and cars. However, after many failed attempts performed by various inventors, it became clear that steam-powered engines were too heavy and couldn't produce enough power to allow the flight of an aircraft [4]. This fact led to the development of far more powerful and lower weight ICEs, in the late 19th century, which eventually would mark the end of steam engines in aviation [5].

Throughout the late 18th and early 19th century, several proposals regarding ICEs were being made until eventually, in 1858, ICEs became a reality when Étienne Lenoir developed the first practical two-stroke engine [6]. During the intake stroke, a mixture of gas and air is inhaled by the engine and ignited by a spark, resulting in a cylinder pressure increase which forces the piston downwards producing work. The combustion products are then extracted through the exhaust valve during the exhaust stroke [7].

Years after, in 1861, Alphonse Beau de Rochas conceived and patented the concept of a four-stroke engine and, later on, Otto developed the Otto Silent Engine, presented in Figure 2.1, the

first practical four-stroke cycle engine in 1876 [7, 8]. His engine was much lighter and smaller than its atmospheric type predecessor, being at least 25% more efficient [2, 8].

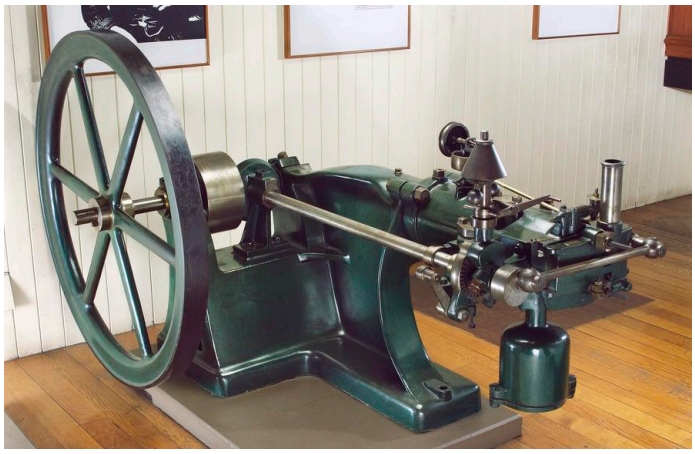

Figure 2.1: Otto Silent engine [9].

Thereupon Otto Silent Engine, two-stroke engines began to be developed and, in 1878, it is invented and built the first practical two-stroke engine by Sir Dugald Clerk [10]. Years later, Gottlieb Daimler and Wilhelm Maybach took Otto's ICE a step further, creating a high-speed four-stroke gasoline-fuelled engine, in which, the liquid fuel is vaporized and mixed with the intake air in a carburettor before the charge enters into the combustion chamber [7]. The most significant differences from other engines were the valve operation and the scavenging process. The inlet valve was automatic, being driven by intake depression, whereas the exhaust valve was operated by a face cam machined in the flywheel face [2].

By 1892, after years of development work, the modern CI engine that had been developed by Rudolf Diesel is produced [6]. His concept of initiating combustion by injecting liquid fuel into air heated only by compression allowed a much higher efficiency than the steam and SI engines used at that time. It was a four-stroke engine using direct injection of liquid-fuel into the combustion chamber, with a high compression ratio, resulting in autoignition of the air-fuel mixture [7, 8].

The discovery of oil fields and the invention of practical versions of two-stroke and four-stroke engines promoted the development of ICE technology in air navigation [4, 6]. These engines were lighter, more mobile, more reliable, and easier to start than steam engines. The majority of gasoline engines for aviation had several pistons, each shuttling back and forth within its own cylinder, being the piston movement transmitted to the crankshaft by the connecting rod which drives the propeller [11].

The beginning of the 20th century was marked by the first powered flight of Orville and Wilbur Wright in 1903 [4]. This revolutionary achievement was made using an engine designed, built and developed in following flights by their mechanic employee Charles Taylor and themselves. It was a four-cylinder water-cooled horizontal engine, with automatic inlet valves, that produced 12 hp and stood the Wright Flyer in the air for 12 s [4]. Wright's engine together with Langley full-scale engine, probably set the beginning of the age of the ICE in aeronautics [5].

Shortly after Wright's achievement, several other aircraft had been successfully designed, built and flown, as various monetary prizes were being offered for setting new records for speed, altitude and endurance [4]. As aircraft designers and builders were developing new air vehicles, they realized the need for greater power and more efficient engines. Thus, aircraft designers began to focus especially on aircraft engine manufacturers and on the automotive industry in search of the best power plants.

Laurent and Louis Seguin were the first to notice the possibilities of rotary engines in aviation with the development of the Gnome rotary engine based on Farwell's rotary engine design in 1907 [4]. It was an air-cooled rotary engine which produced 50 hp and weighed 78 kg [4]. In this type of engines the crankshaft doesn't move and is fixed to the aircraft, while the cylinders and the external casing, where the propeller is firmly attached, rotates [12]. By 1914, a wide range of rotary engines was developed, making them extremely popular during the first years of World War One (WWI). The Gnome, shown in Figure 2.2, was the first of a long line of ever more powerful wartime engines, introducing air cooling as a way to eliminate the plumbing and lighten its own weight [11]. Well-known fighter planes such as German's Fokker DR-1 and Britain's Sopwith Camel were powered by this type of engine [12].

Figure 2.2: Gnome rotary engine [13].

Despite their popularity in the war, rotary engines had some problems which made engine designers return to the water-cooled V type engines [5]. During the WWI, several water-cooled engines emerged, of which stands out the Liberty and the Hispano Suiza V-8. Its success started a revolution in liquid-cooled engine design, which resulted in the Rolls-Royce (RR) Kestrel and Merlin series engines [5].

After WWI several major breakthroughs were achieved which promoted the development of more efficient, low weight, powerful engines and enabled a better understanding of how fuels affect combustion. These advances made possible the use of better fuels and improved engine compression ratios. At this time, air-cooled radial engines appeared as a more reliable and lightweight engine [11]. These new engines were arranged so that its cylinders extend radially outward from its hub. The first really successful radial engine was the Pratt & Whitney Wasp

which developed 425 hp, in 1927 [5].

As years went by, aircraft designers move to the next step of engine development, fly at high altitudes, since power plants were getting powerful enough [11]. Furthermore, flying high would give some advantage over opponents and allowed to fly faster and go farther, because at high altitudes the air is thinner and consequently the drag is less. However, high altitude flight had a major drawback which was the significant decrease in engine power as the aircraft climbs. So, in order to overcome this shortcoming, designers fitted the engines with a supercharger which increases the air density and pressure, forcing more air through the engine, enabling it to produce full power at high altitudes [11].

The advances in supercharging, knock resistant fuels, cooling systems and detail design were applied in World War II aircraft engines, resulting in an astonishing improvement of liquid-cooled and air-cooled engines performance [5, 11]. The Merlin series engines, one of which is shown in Figure 2.3, were built by RR and had a big influence in the outcome of the war since they powered many ally fighters and bombers like the Havilland Mosquito, P-51 Mustang, Spitfire, Hurricane fighters and Lancaster Bombers [14].

Figure 2.3: Rolls-Royce merlin engine [15].

By 1950 aircraft piston engines had become light, powerful, and reliable. Despite that, around 5 years earlier, engineers at major engine plants began to deviate from piston engines to engines with much greater potential and more extensively used in the modern aviation industry, the jet engines [16].

With the recognition of the importance of environmental issues in 1970, new factors became important such as emissions level and fuel consumption which now have a major influence in engine design and operation [7]. Until today, emissions level and fuel consumption have been decreasing meanwhile, ICEs efficiency continues to increase driven both by legislation and the need to reduce operating costs.

After many years of development, it is expected that ICEs have reached a point where no more improvements can be made. Nowadays, there have been significant improvements in efficiency

and emissions control since the concern about climate change increases by each day, forcing engine builders and designers to develop new strategies to obtain power from an engine without polluting that much. With the discovery of new materials and the development of brand-new technologies and fuels, new possibilities to reduce weight, heat losses and emissions will be unlocked, foreseeing further optimization and hope for ICEs in the future.

2.0.2 Classifications

Since this dissertation focuses essentially the intake process of reciprocating ICEs, only the main engine characteristics and the ones related to the induction procedure will be taken into account.Thus, ICEs can be classified by [6, 8]:

1. **Type of ignition**
    (a) SI engine - the combustion process in each cycle begins with a spark plug, which gives an electrical discharge igniting the air-fuel mixture in the combustion chamber.
    (b) CI engine - the combustion starts when the air-fuel mixture auto ignites due to the high compression and temperature experienced in the combustion chamber.
2. **Working cycle**
    (a) four-stroke cycle - requires the piston to move four times over two engine revolutions for each cycle.
    (b) two-stroke cycle - the piston has to shift two times over one crankshaft revolution for each cycle.
3. **Basic engine design**
    (a) Reciprocating - the engine has one or more cylinders in which pistons oscillate back and forth in a cyclic pattern inside the cylinders, transmitting power to a drive shaft by means of a connecting rod and crankshaft mechanism.
    (b) Rotary - the engine is made of a block built around the crankshaft and a triangular-shaped rotor which rotates eccentrically in the housing.
4. **Valve location**
    (a) Overhead Valves (OHV).
    (b) Valves in the block.
    (c) One valve in the head and one in the block.
5. **Air intake process**
    (a) Naturally aspirated - atmospheric air is admitted into the engine.
    (b) Supercharged - a pre-compressed fresh mixture enters in the engine.
    (c) Turbocharged - the engine admits fresh mixture compressed in a compressor driven by an exhaust turbine.
6. **Application**
    (a) Light aircraft
    (b) Automobile
    (c) Locomotive

2.0.3 Operating Cycles

As previously mentioned, reciprocating engines operate on a four-stroke or two-stroke cycle. These operating cycles are standard for all engines, with only slight variations depending on individual designs [6]. The majority of ICEs operate on a four-stroke sequence, where each cylinder requires four piston movements or two revolutions of the crankshaft in order to complete the operating cycle. Both types of engines (SI and CI) can be designed to operate on either four-stroke or two-stroke configuration. The operating sequence of a four-stroke SI engine is presented in Figure 2.4 followed by the description of each cycle stage [6, 8, 10].

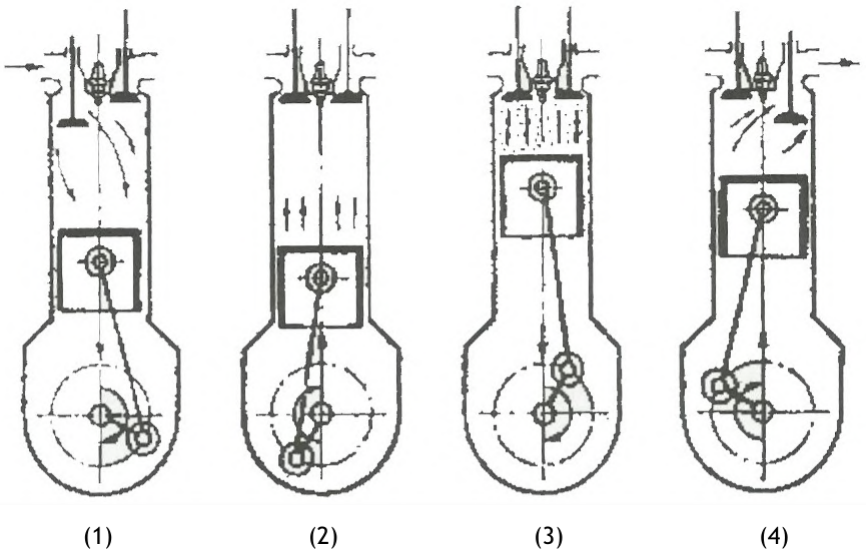

Figure 2.4: Four-stroke cycle [17].

1. **Intake stroke** - starts with the piston moving from top dead center (TDC) to the bottom dead center (BDC) and with the intake valve open and the exhaust valve closed. This creates a vacuum inside the cylinder which causes a pressure differential between the intake system and the interior of the cylinder, drawing air into the cylinder. As the air moves through the intake system, fuel is mixed with the inlet air by means of a fuel injector or carburettor.
2. **Compression stroke** - Both valves are closed and the piston travels up to TDC. This piston motion compresses the air-fuel mixture to a small fraction of its initial volume, raising both the pressure and temperature in the cylinder. The compression starts shortly after BDC because the intake valve takes some time to close. As the piston approaches TDC, the spark plug is fired and combustion is initiated.
3. **Power stroke or expansion stroke** - Combustion raises the temperature and pressure inside the cylinder forcing the piston away from TDC. As the piston travels to BDC, cylinder volume is increased whereas the pressure and temperature decrease. Near the end of the power stroke, the exhaust valve opens, initiating the exhaust blowdown. This is the stroke which produces the work output of the engine cycle.
4. **Exhaust stroke** - By the time the piston reaches BDC, exhaust blowdown is complete, the exhaust valve is open and the cylinder is full of exhaust gases at approximately atmospheric pressure. The piston shifts to TDC, pushing most of the remaining exhaust gases

out of the cylinder into the exhaust system. As the piston approaches TDC the inlet valve starts to open, being fully open by TDC when the new cycle begins. Once the exhaust valve is fully closed, shortly after TDC, some residual gases are left to dilute the next charge. This period when both intake and exhaust valves are open is known as valve overlap.

Relatively to the four-stroke CI engines, the operating sequence is the same as the four-stroke SI engines but there are two major differences. The first one, during the intake stroke, only air enters the cylinder instead of an air-fuel mixture. The other one happens in the compression stroke, where the compression is performed at higher pressures and temperatures than in SI engines and near TDC fuel is injected into the combustion chamber, forming the air-fuel mixture which evaporates and auto ignites.

On the other hand, the two-stroke cycle allows a higher power output from a given size engine and a simpler valve design [8]. This cycle generates a power stroke at every revolution of the crankshaft instead of every two revolutions as four-stroke engines and eliminates the separate induction and exhaust strokes. Thus, two-stroke engines are mechanically simpler and have higher specific power than four-stroke engines. Despite that, the efficiency of these engines is probably lower than four-stroke engines, since it is difficult to ensure that the induction and exhaust processes occur efficiently [10]. The level of the scavenging process is the performance limiter since it includes simultaneously the exhaust of the burnt mixture and the introduction of the fresh air-fuel mixture into the cylinder.

2.0.4 Theoretical Cycles

The operating cycle of an ICE is quite complex and difficult to analyse. Therefore, with the purpose to make the study of the engine cycle easier, the real cycle is approximated with an ideal air standard cycle which assumes that [6, 18]:

- The mixture inside the cylinder is solely air for the entire cycle.
- The engine cycle is closed because the exhaust gases are fed back into the intake system.
- The combustion process is replaced by a heat addition with the same amount of energy.
- The open exhaust process is substituted with a closed system heat rejection process of equal energy.
- Intake and exhaust strokes are performed at constant pressure.
- Compression and expansion strokes are approximately isentropic.
- The combustion process is idealized by a constant volume process in the case of a SI cycle or a constant pressure process in a CI cycle.
- Exhaust blowdown is estimated by a constant volume process.
- Valves close and open instantly.
- All processes are reversible.

For SI engines the idealization is referred to as Otto cycle which consists of six processes presented in Figure 2.5 and described below [6, 18]:

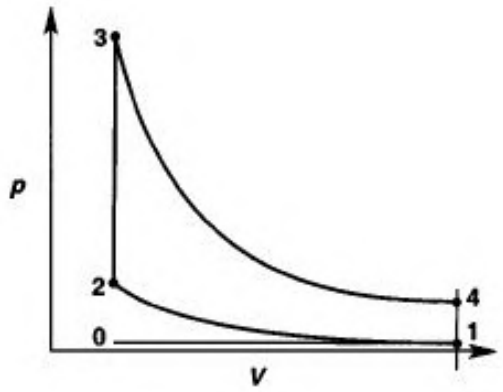

Figure 2.5: Ideal Otto cycle [18].

0 to 1 constant pressure process at atmospheric pressure that corresponds to the intake stroke where the piston is at TDC, the inlet valve is open and the exhaust valve is closed.

1 to 2 isentropic compression of air from BDC to TDC which increases the pressure inside the cylinder and consequently reduces cylinder volume.

2 to 3 constant volume heat addition process at TDC which corresponds to the combustion process in a real engine cycle, where a large amount of energy is added to the air, raising the temperature and also the pressure to very high values resulting in point 3.

3 to 4 isentropic expansion of air which decreases both values of pressure and temperature in the cylinder as the cylinder volume increases. It is equivalent to the power stroke where the piston is forced back towards BDC, producing the power output of the engine.

4 to 1 constant volume heat rejection process which corresponds to the exhaust blowdown mechanism. At this point the exhaust valve opens instantly, according to the idealized cycle, reducing suddenly the cylinder pressure to atmospheric pressure and the temperature due to the expansion cooling.

1 to 0 constant pressure process at atmospheric pressure which represents the exhaust stroke, where the remaining exhaust gases are expelled through the exhaust valve.

The reality differs undoubtedly from the ideal cycle since several processes that occur in the engine operating cycle are approximated and some aspects are not taken into account. In Figure 2.6 is shown the real cycle of a four-stroke engine at Wide Open Throttle (WOT) superimposed on the Otto cycle with the differences between them being described below [6, 18].

This Figure doesn't consider the real intake and exhaust strokes, being only represented the ideal intake and exhaust strokes. The curve **y-z**, presented in the Figure 2.6, is an isentropic curve that intersects with point **b**. Points **a, b** and **c** correspond to the beginning of ignition, the end of combustion and the opening of the exhaust valve, respectively. The hatched area to the left of point **a** and above point **b** until the curve **y-b** represents the time loss, the heat losses are indicated by the hatched zone above curve **b-c** and the stippled area near curve **c-1** shows the exhaust blowdown loss.

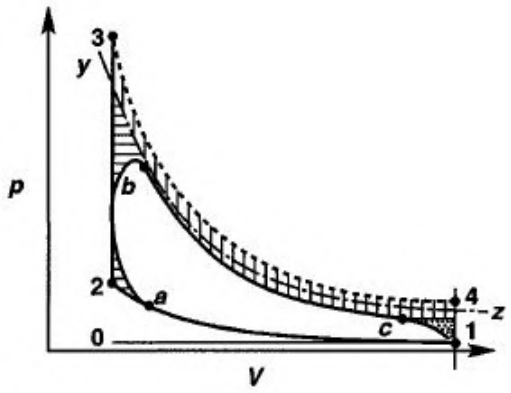

Figure 2.6: Real Otto Cycle versus Ideal Otto Cycle [18].

From the analysis of Figure 2.6 it is possible to see some differences between both cycles. The first is that the combustion process doesn't occur instantly. The spark ignites the surround mixture (point **(a)**), and a flame front progresses outward from there. As the flame travels it is converting chemical energy into heat, raising the pressure and temperature continuously. It takes some time to the flame to travel from the spark plug to the farthest side of the combustion chamber, this is known as time loss. The difference in the area from curve **a-b** to the respective ideal process represents the work that is lost due to time loss. For this reason, it is necessary to start the combustion substantially before TDC in order to gain some of the lost work. During the combustion process, the mixture is losing heat, therefore, the point **(b)** is below the curve **3-4**.

Going back to the compression stroke, when the charge is compressed, it is losing heat to the cylinder walls. This heat loss is usually neglected because the temperature is not very high. However, after combustion, the temperature inside the cylinder is significant and as the piston executes the power stroke, there is a considerable amount of heat lost to the combustion chamber and the cylinder walls, leading to a notable reduction in cylinder temperature and pressure at the end of the stroke. The difference between curve **b-c** and curve **3-4** represents the work lost for heat losses.

Lastly, during the exhaust stroke, the exhaust valve is opened when the piston comes close to BDC, resulting in a gradual pressure drop as the exhaust gases leave the cylinder. This pressure difference between both cycles is the exhaust blowdown loss and represents the inaccessible work. The exhaust blowdown process requires a finite time to happen and doesn't occur at constant volume as the ideal Otto cycle defends. This way, the exhaust valve opens before BDC (BBDC) and as a result, the work produced later in the power stroke is lost.

In the case of the CI engine cycle, the idealized process is the Diesel cycle which differs from the Otto cycle by the fact that the energy is added at constant pressure [10].

Chapter 3

Engine breathing

Deep knowledge of the induction process is critical to attain the best engine performance characteristics together with the lowest emissions level. This chapter will present the main factors and phenomena which affect the inlet flow, the key aspects to have in mind in order to optimize the inlet system, the set of concepts and definitions involved in a valve system, the behaviour of the discharge and flow coefficients according to the literature and, at last, a discussion of the valve and port designing aspects and configurations.

3.1 Intake system

The induction system is critical to engine operation since it collects and delivers the air to the engine, allowing the combustion process to happen, and therefore, the production of power. Through this system, air at atmospheric pressure is drawn into the engine, mixed with fuel and evenly distributed among the cylinders. The air-fuel mixture quality provided to the cylinders will establish how much power it can be created by the engine. Every reciprocating ICE, whether small or large, share the same problem which is effective breathing [19]. In order to optimize engine breathing, it is required to follow the airflow through the induction system and understand the interaction between the air and the intake components and also the flow phenomena which occur during the induction stroke.

The intake system must meet some requirements [10, 19]:

- Be able to eliminate dust and other unwanted debris from the inlet air.
- It has to produce the best pressure pulse motion in order to optimize cylinder filling.
- For engines with carburettors, the induction system has to adapt the pressure pulse at the carburettor to attain the appropriate air-fuel ratio in every engine operating condition.
- Assign the air-fuel mixture evenly through the cylinders.
- Fit in the available place.
- Be easy to manufacture and accessible to perform modifications and maintenance.
- Be durable and mechanically robust.

The intake manifold is a key element in the intake system since engine breathing and performance are highly affected by the unsteady flow which flows inside the intake manifold [20]. This part of the intake system has the following functions [21]

- Guide the air or inlet charge into the cylinders;
- Distribute equally the air-fuel mixture through the cylinders;
- Keep pressure losses to a minimum throughout the manifold;

- Improve engine breathability;

As shown in Figure 3.1, a typical intake manifold consists of an air duct, throttle plate, inlet plenum and runners. The intake plenum is a high-pressure air chamber that delivers air to the several cylinders and equalizes the pressure in the manifold to provide more equal distribution, whilst runners link the plenum to each cylinder [19].

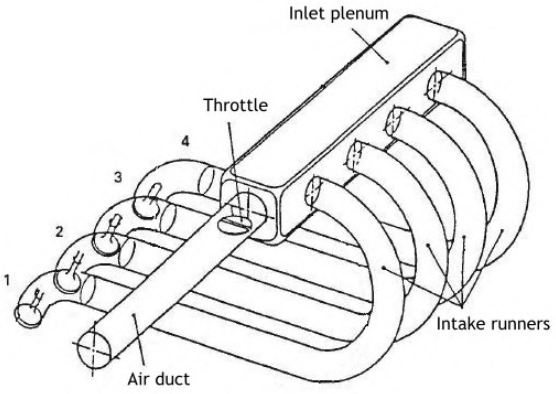

Figure 3.1: Typical SI engine intake manifold adapted from [10].

3.2 Volumetric efficiency

The volumetric efficiency, η_v, is one of the most important performance parameters in four-stroke engines since it is a measure of engine breathing. It is well known that the inlet system is constituted by several components. Every single component in the intake system represents a barrier to the airflow and consequently to the volumetric efficiency, which is defined as the mass flow rate of air that enters into the cylinder divided by the rate at which mass is displaced by the piston [7]. Therefore, the volumetric efficiency is obtained by [8]

$$\eta_v = \frac{2\dot{m}_a}{\rho_{int} V_d N} \quad (3.1)$$

wherein

$\dot{m}_a$ is the air mass flow rate which enters into the cylinder in $\mathrm{kg/s}$.
ρ_{int} is the air density inside the inlet manifold that is expressed in $\mathrm{kg/m^3}$.
V_d is the displaced volume which comes in $\mathrm{m^3}$.
N is the engine rotational speed in rps.

The volumetric efficiency measures the pumping performance of the whole inlet system whenever it is based on atmospheric conditions, otherwise, it quantifies the breathing performance of the intake port and valve [8]. The air density in the intake manifold is affected by the pressure and temperature experienced in the intake duct and can be obtained by [22]

$$\rho_{int} = \frac{p_{int}}{R_{air} T_{int}} \quad (3.2)$$

where

p_{int} is the air intake pressure in Pa.
R_{air} is the gas constant for dry air which is equal to 286.9 $\mathrm{J/kgK}$.
T_{int} is the air intake temperature indicated in K.

As the charge flows through the induction system there are pressure losses when it passes through each intake element. These losses depend on the cross-sectional area through which the mixture flows, engine speed, air-fuel mixture density and the flow resistance made by the intake components [8]. On one hand, intake components should present minimum flow resistance since a high flow resistance can harm overall parameters like the volumetric efficiency. On the other hand, if the inlet elements are made excessively free-flowing, turbulence creation can be reduced too much, making the combustion process to happen too slowly, and consequently, the power to drop in SI engines [19]. Therefore, a balance is required in order to get the best of both outcomes.

SI engines have volumetric efficiencies between 75 to 90% at full throttle, whereas CI engines reach even higher volumetric efficiencies [6]. The volumetric efficiency is affected by a big number of variables being one of the most difficult parameters to improve. As the volumetric efficiency increases, there is more air inside the cylinder, and thus, can be introduced and burned a greater amount of fuel, resulting in higher engine torque and power. So, it is desirable to maximize the volumetric efficiency of an engine, not only because engine power and torque are maximized, but also the fuel consumption, as well as emissions, are minimized. However, there are some factors that have a great impact on volumetric efficiency like the valve size, valve lift, valve timing and the design of intake and exhaust manifolds [7, 17].

3.3 Factors that affect engine breathing

Intake system design

The design and optimization of such important system usually involve a tricky process of synthesis based on physical tests, where several geometries are tested under conditions experienced in real engines [23, 24]. From these tests, designers can evaluate if a certain intake geometry benefits or harms engine performance characteristics. Even though this method might be effective, it is quite expensive, time-consuming and the flow complexity existent in the intake is harder to replicate [25, 26]. Therefore, today's engineers rely on sophisticated software programs, which obtain accurate results in a short period of time, to simulate the actual engine conditions in order to properly design and optimize intake systems.

At the designing stage of the intake system, a clear understanding of several factors and phenomena such as the pulsed flow and the variation of the throttle plate position which considerably change the processes that conduct the flow to the cylinder is required. These features bring additional problems to what it was already complicated and have a major influence on the effectiveness of the intake system, combustion and consequently in engine performance. Knowing how to take advantage from these aspects is crucial to design a proper intake system and to allow an easy engine breathing, which according to Annand and Roe [19], "is the key to

high sustained power” .

The growing seek for increased engine breathing has promoted the improvement in design and layout of some critical engine components for engine performance such as the inlet manifold [25]. Although the amount of charge which enters into the cylinder depends on the pressure drop through the inlet valve and its effective area, enhanced volumetric efficiency can be achieved by optimizing the inlet manifold for the pulsating flow [27]. This optimizing process is generally called intake tuning and consists in making modifications into the plenum and the inlet runners in order to take advantage of the pressures waves inside the inlet track, and thus, improve engine breathing.

As indicated above, the flow in the intake and exhaust manifolds is pulsatory and unsteady due to the piston motion and valve system action. Knowing that pressure waves carry energy, it is quite clear the importance of taking advantage of this energy to reduce the work required to maintain the charge flow or to force more mixture into the cylinders [19]. However, if the intake or exhaust systems are poorly designed this energy can act against the charge, resulting in a decrease in engine power and efficiency.

The Chrysler Ram Theory is a concept that explains the airflow dynamics inside the inlet manifold, being a reference for tuning strategies [28]. According to this theory, as the engine operates, the opening and closing of the intake and exhaust valves create a compressible flow process where pressure waves travel back and forth throughout the inlet and exhaust systems. Pressure waves are generated due to the air column movement set by the piston motion and the standing wave produced in the previous cycle [27]. A compression wave is obtained when pressure is increased, while a rarefaction wave is achieved if the pressure is reduced [10, 18]. When considering a compression wave travelling towards an open end, for instance, the manifold plenum area, the pressure within the wave is greater than the pressure in the plenum. Because of this pressure difference, once the compression wave reaches the open end, a rarefaction wave is created in the opposite direction at the end of the pipe, so that, the pressure difference at the end of the pipe is zero [19]. Therefore, at an open end, a rarefaction wave is reflected as a compression wave and vice versa.

In the case of a closed pipe end, the flow velocity at the pipe end must be always zero [19]. Thus, when a compression wave finds a closed end, it is reflected as another compression wave, so that, the velocities of both waves cancel each other out, resulting in a total gas velocity of zero [19]. With that in mind, at a closed pipe end, a compression wave is reflected as a compression wave, while a rarefaction wave is reflected as another rarefaction wave. The wave propagation and reflection mechanism in the induction system are represented in Figure 3.2. During the induction stroke, when the intake valve opens and the piston reaches its maximum speed towards BDC, the pressure upstream the valve is minimum, resulting in a creation of a rarefaction wave that moves from the piston to the open end or plenum area through the runners [23]. As soon as it reaches the plenum, the rarefaction wave is reflected back into the runner towards the cylinder as a compression wave that, if reaches the valve right before Intake Valve Closing (IVC) will push more air into the cylinder. This effect normally increases with engine speed, since the inertia of the intake flow rises [29].

During the exhaust stroke, more precisely in the valve overlap period, a rarefaction wave is

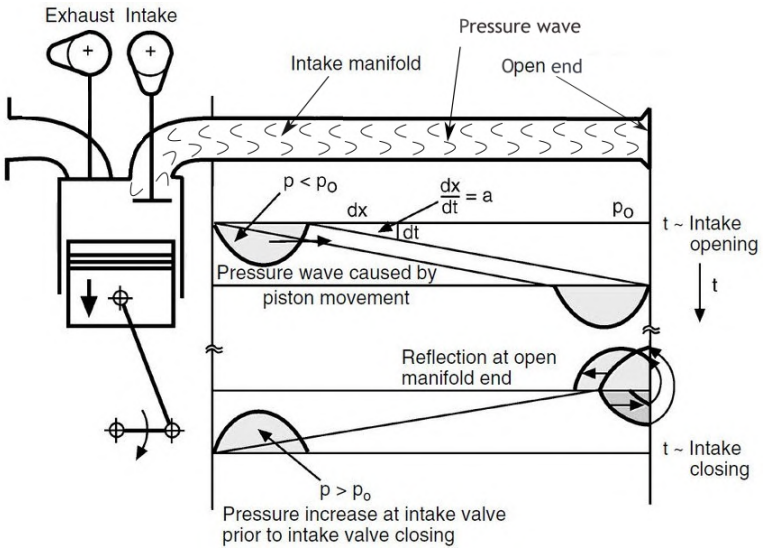

Figure 3.2: Development and propagation of pressure waves along the intake system adapted from [30].

generated as the expelling of the combustion gases and the introduction of a fresh charge is being made [31]. The wave proceeds through the intake and is reflected as a compression wave when reaches the plenum area. If the length of the intake runner is accurate for the rpm range and the flow rate is such, that pressure waves shortly before the intake valve will be reinforced, some more air will be admitted into the cylinder as a result. This phenomenon is more evident in single-cylinder engines since in multi-cylinder engines the almost continuous flow considerably reduces the effect of pressure waves [27].

Intake tuning is influenced by the piston movement and the resonance features of the induction system, not being affected by the valve action [26]. Despite that, valve duration has an important effect on the intensity of the benefits obtained through intake tuning [26]. This tuning strategy will be truly effective only at a specific rpm since the engine speed doesn't influence the propagation speed of pressure waves [31]. Outside that engine speed, the system will be out of tune, reducing the volumetric efficiency and engine power relatively to a tuned system. In order to overcome the shortcomings of conventional manifolds, variable intake manifolds were developed. This system uses dual intake runners for each cylinder, one short in length to assist in high engine speed operation and a longer one for low engine revolutions, as shown in Figure 3.3.

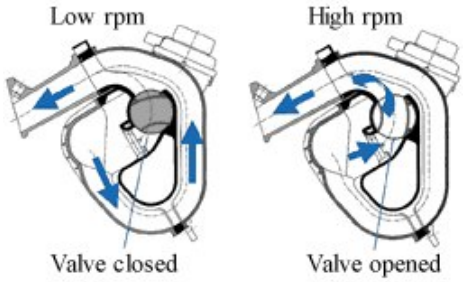

Figure 3.3: Variable intake manifold system [32].

The sensitivity of the volumetric efficiency is a factor that has been haunting engine designers. Its dependency on runner length and engine speed creates challenges to engine designers and engineers [7]. When designing an intake manifold, the length and the diameter of a runner should be sized simultaneously to balance the amount of charge transported to each cylinder [6]. This way, the power delivered by each cylinder is more equal and engine running gets smoother. Figure 3.4 represents the variation of the volumetric efficiency with engine speed and runner length. It is possible to conclude that an increase of the runner length results in higher volumetric efficiency, but the engine speed, in which, the volumetric efficiency is maximum decreases as runner length gets bigger. Moreover, it is visible the gain in volumetric efficiency when comparing a runner pipe of a particular length to a no pipe configuration.

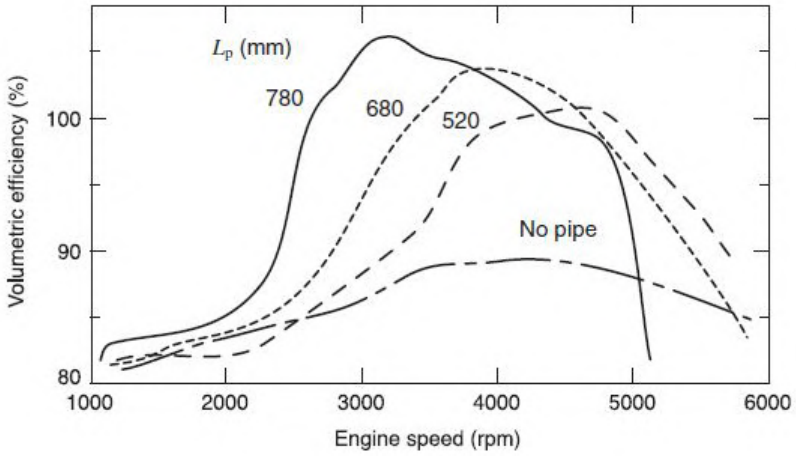

Figure 3.4: Effect of intake runner length on the volumetric efficiency as a function of engine speed [7].

The best outcome in terms of runner configuration can be achieved with an active intake manifold [6]. This system is very similar to the variable intake manifold one since it allows the ability to change runner length and diameter accordingly with engine speed. Thus, the ram effect is intensified for a wider range of engine speeds, resulting in an overall power and torque increase along with a decrease in fuel consumption. However, the designs of variable induction manifolds can be fairly complex and expensive to manufacture.

Another aspect of interest is the valve-port geometry which is where the major pressure losses happen in the entire intake system. The respective losses are related to the effective cross-section of the inlet port-valve [24]. The effective cross-section of the intake valve is selected according to the engine operating speed range and size. For high-speed engines, a larger effective cross-section valve, in other words, a multi-valve configuration will result in a higher volumetric efficiency if a properly designed manifold is utilized [24]. However, at low or medium speeds, this greater effective cross-section will contribute to a higher backflow.

The main overall conclusion is that the ramming effect strongly depends on the inlet valve timing, intake runner length and diameter and also the engine speed. In addition, intake tuning is only achieved when the inlet manifold geometry, valve timing, and engine speed are correctly chosen. However, the inlet system design is normally established by the cost, ease of construction and the space that it will occupy instead of flow optimization [10]. Thus, it is quite difficult or perhaps impossible to design an induction manifold that provides both improved volumetric

efficiency and uniform mixture distribution.

Mixture preparation

The induction and fuel systems have the common goal of preparing the air-fuel mixture so that the requirements which the engine must deliver over its operating range can be accomplished. The air-fuel mixture may be adjusted by a carburettor or a fuel injection system. If direct injection is not employed, fuel in the form of liquid film, vapour and droplets will be encountered in the intake system [10].

In a typical fixed choke carburettor air flows across a converging-diverging nozzle (venturi), in which, it is mixed with the proper amount of fuel and then the resultant mixture goes through the throttle plate into the intake manifold. As the engine speed rises, higher flow rates will cross through the venturi, producing a greater pressure drop. This means a higher differential pressure that leads to a richer air-fuel mixture. However, bigger pressure drops imply a lower volumetric efficiency [6]. In simpler carburettors what is possible to attain is not the same as what is ideally desirable at each engine condition. So, there has to be a certain compromise which can be influenced by the existence of airflow pulsations in the carburettor [19].

Fuel can be added into the airstream before the intake manifold, inside the manifold or into each cylinder. The sooner the fuel is added, more time it has to evaporate and to achieve the appropriate air-fuel mixture [6]. Considering an engine with a carburettor, when fuel leaves the fuel pipe, it breaks in small droplets (fuel atomization) which are transported with the high-speed airstream. As the flow travels to the intake manifold these droplets evaporate, mix with the air and deposit along the manifold walls [6, 8]. The gaseous fuel will take the place of some air which leads to a certain decrease in volumetric efficiency.

The flow normally enters the intake manifold through a tee junction. The carburettor-manifold connecting pipe is the riser and the manifold branches are the runners [19]. The design of this tee junction is fundamental for a good mixture distribution across the cylinders. In Figure 3.5 is shown the junction between the riser and the runners of an intake manifold where the best performance results, in a WOT position, are achieved when the riser is short and the section which the riser and the runner joins is sharp instead of rounded as aerodynamic perspective alone would defend.

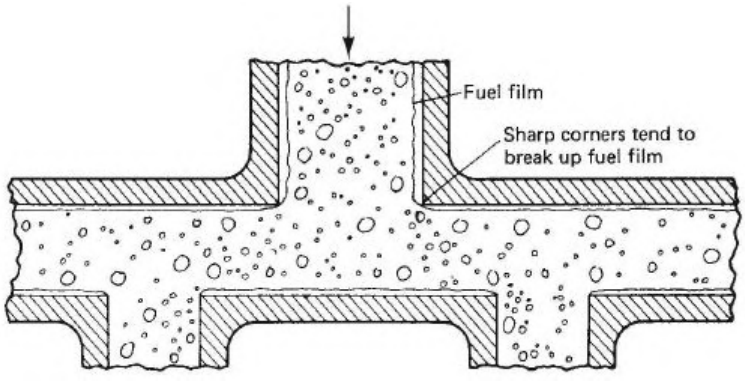

Figure 3.5: Air-fuel mixture flow in the intake manifold [10].

The reason is that a shorter riser diminish the area for liquid fuel deposition and the sharp edges cause the liquid fuel to break up, while rounded edges allow the liquid fuel to keep moving along the manifold walls [19]. The liquid fuel film arises due to gravity which detaches some droplets from the airstream and when the runner makes a corner [6]. Thus, the length and bends in a runner affect the quantity of fuel that is transported by a certain airstream into the cylinder. However, some fuel droplets can have greater inertia than the air, which results in a fuel concentration on the wall perpendicular with the riser [19]. In this area, heating the manifold is effective to accelerate fuel vaporization. The rate at which the fuel vaporizes depends on the temperature and pressure experienced in the intake manifold and on the amount of liquid fuel presented there. A conventional manifold system which links to several cylinders must have some heating to boost fuel evaporation, so that, cylinder mixture delivery is not overly influenced by liquid fuel moving on the walls [19]. However, the temperature rising decreases the mixture density and, in its turn, reduces the volumetric efficiency and engine power [10]. In addition to that, this fact increases the engine tendency to knock, therefore, the compression ratio must be reduced.

In order to reduce atmospheric pollution and to overcome the shortcomings of carburettors, fuel injection systems have been developed and implemented in ICEs. There are two kinds of fuel injection systems, single-point and multi-point fuel injection. In the former which is also known as throttle body fuel injection, the fuel is sprayed at the manifold, allowing more precise control of the fuel quantity injected, better fuel atomization and droplets downsizing, however, it can't solve the distribution problems of carburettors [10, 18].

The latter has the possibility to deliver a higher power because the manifold can be designed and tuned for optimum airflow alone, since fuel transportation across the manifold is no longer a design restriction [8, 10]. Thus, multi-point systems are more efficient than single-point ones, opening more possibilities for volumetric efficiency improvement since the pressure drop through the inlet system is reduced and there is no need for heating the inlet manifold [17, 27].

Boundary layer

The presence of boundary layers in the intake track, flow separation and the Mach number significantly affects engine volumetric efficiency, being three more factors to take in consideration at the designing stage [18]. In Figure 3.6 is presented the evolution of the boundary layer along an intake pipe without any curvature. The pressure difference between the atmospheric air and the air inside the cylinder causes the air to flow into the cylinder. As the pressure difference gets bigger, the rate of air rushing into the cylinder increases until the laminar flow becomes turbulent [19]. This flow transition only occurs when an oscillating frequency is created and keeps being amplified by the flow field and when the Reynolds number, which is the quotient of the inertia forces to viscous forces, as shown below, reaches a typical value.

$$Re = \frac{\rho_{int} U D_p}{\mu} \quad (3.3)$$

wherein

U is the airflow velocity expressed in $\mathrm{m/s}$.

D_p the inlet pipe diameter in m.
μ is the dynamic viscosity of the fluid in $\mathrm{N\,s/m^2}$.

When the engine is performing the induction stroke, a boundary layer is created in the pipe walls as the air flows in the intake duct due to the viscous effects of the fluid. At the beginning of the duct, the flow velocity profile is uniform, but as the pipe length increases, the effects of the wall become bigger, in other words, the boundary layer gradually grows as shown in Figure 3.6. As the flow moves towards the wall, the flow velocity decreases and in the wall the flow velocity is zero due to the no-slip condition. From Figure 3.6 is clear that as the pipe length increases the flow velocity profile gets more parabolic and the inviscid region, which is the middle area of the pipe where the effect of the wall is not felt by the fluid yet, becomes smaller and smaller. Eventually, the boundary layer becomes large until it fills the cross-sectional area of the pipe. From this point, the flow is fully developed and its velocity is no longer dependant from the pipe length.

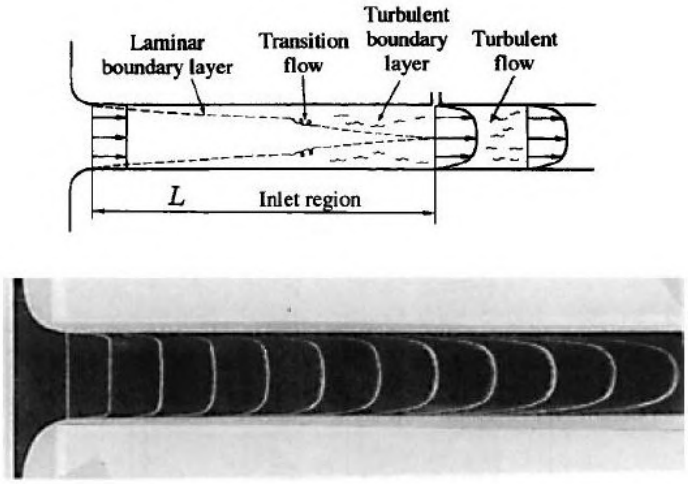

Figure 3.6: Development of the boundary layer in the intake duct [33].

The creation of boundary layer inside the intake pipe gradually decreases the effective area of the pipe and consequently reduces the static pressure throughout the duct. As a result, the airflow velocity increases and a negative pressure gradient is felt inside the intake track, leading to a lower amount of air admitted into the cylinders, hence, the volumetric efficiency drop. For this reason, special attention should be given by engine designers to the effects of the boundary layer in the intake system.

3.4 Inlet valves

Generally in flow systems, it is quite important to focus firstly on those components which provide greater resistance, for instance, the intake and exhaust openings since they will have the greatest effect in the flow [19]. This open areas change continuously during engine operation and they are closed and opened by valves or piston-controlled ports. In this dissertation, it will be focused only the valve system because the engine which will be studied ahead is a four-stroke engine with a multi-valve configuration.

3.4.1 Configurations and types

There are several design options for both engine valves in terms of location and type. In older engines, camshafts were mounted near the crankshaft while the valves were assembled in the engine block [6]. As engine development proceeded, valves were placed into the cylinder head and a mechanical linkage assembly was developed and installed in ICEs to act on valves. Figure 3.7 presents an OHV engine or pushrod engine where the camshaft is assembled next to the cylinder block.

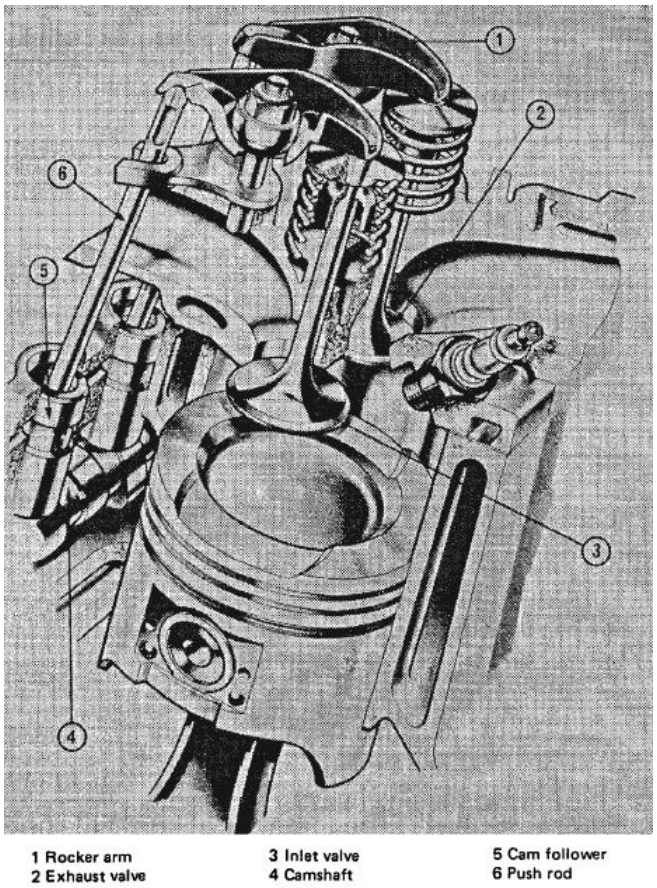

Figure 3.7: Pushrod engine configuration [10].

An engine with this configuration controls the valve motion with the help of rocket arms and pushrods that transmit the rotational force of the camshaft to the engine valves. This design results in a simple camshaft installation and a cheap solution in terms of manufacturing [10].

As years went by, the camshaft started to be mounted in the engine head because the closer the camshaft is from the valves, less mechanical losses occur, which leads to greater mechanical efficiency of the system [6]. An Overhead Camshaft (OHC) engine operates the valves by means of a rocket arm or directly through the camshaft follower or cam. In Figure 3.8 is shown an OHC engine where the camshafts are mounted directly over the valves. When the camshafts rotate, the cam pushes downwards the cam follower, which is connected to the valve, opening it and, at the closing time, the camshaft lobe gradually stops pushing the follower down, closing the

valve due to the spring force. The drive to the camshaft is generally made by a chain or toothed belt system which has the advantage of damping out the torsional vibrations experienced in the assembly [10].

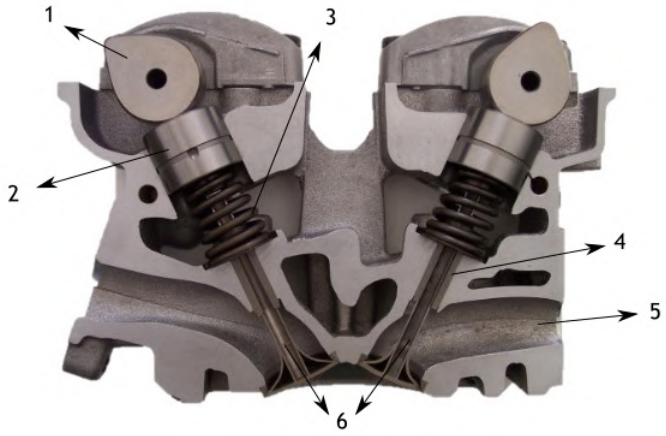

Figure 3.8: OHC engine adapted from [34]. (1) cam; (2) cam follower; (3) valve spring; (4) valve guide; (5) port and (6) poppet valves.

Nowadays, ICEs adopt an OHV and OHC configuration having one or two camshafts placed in the engine head since this arrangement produces better flow characteristics in the intake and exhaust along with lower mechanical losses [6, 7].

During the development of ICEs, several different types of valves and valve actuation systems have been used. The vast majority of these vanished as the years went by. Nevertheless, during the twenties, the poppet valves domain was contested by the sleeve valves. This system achieved high popularity and consisted in an inner sleeve which ran the piston inside and shifts within an outer sleeve that moves inside the cylinder [18]. The sleeves had ports and moved up and down by the action of pushrods that were regulated by a cam. Eventually, the sleeve valve system disappeared, probably due to the high cost and difficulty of fabrication and the fact that the sleeve required to be flooded in oil which could enter in the cylinder during engine operation. [18].

Another valve mechanism which is used sometimes, even nowadays, is the desmodromic valve. This system can adopt several mechanical forms, one of which is illustrated in Figure 3.9. In this mechanism, there are two separated complementary cams, one opens the valve by pressing the opening rocket arm and the other closes the valve by means of a closing rocket arm [18]. In contrast with the poppet valve system, no spring is needed to secure the valve on the cam.

In a poppet valve system, the cam must accelerate the valve upward and also be able to do it in opposition to the spring force, whereas in a desmodromic valve assembly, the cam only needs to provide the force to speed up the valve train [18]. Therefore, the desmodromic setup reduces fatigue and lubrication problems as well as engine friction at low speeds, and, at the same time, allows higher engine speeds.

It is important to note that when the engine speed overcomes the speed at which the force

Figure 3.9: Desmodromic valve system [35].

made by the spring is equal to the inertial force, the cam follower stops being in contact with the camshaft lobe, resulting in a reduction in engine efficiency and performance and most likely can lead to failure [10, 18, 36]. This is known as valve float or valve bounce and is the main reason why the desmodromic valve train is still being used today. Desmodromic valve systems significantly reduce the possibility of valve float and improve the engine overall efficiency and performance, however, this comes at the cost of a greater fabrication cost and complexity [18, 36].

3.4.2 Theoretical and actual valve motion

Poppet valves which are pushed open and spring closed at the proper time in the engine cycle through the camshaft are the most commonly used type of valves in ICEs due to their matchless sealing features [6, 7]. Ideally, valves should open and close instantly in the engine cycle, but as we know, this is impossible to accomplish due to mechanical limitations such as valve seat wear and noise, which force the valve opening and closing to be slower. In order to avoid valve seat wear, the cams are intended to provide quick and smooth opening and closing for valves.

The dynamic behaviour of a valve gear is set by the theoretical and the actual valve motion. Starting with the theoretical valve movement, this is established according to the cam and its follower geometry [10]. In Figure 3.10 is represented the usual curves of lift, velocity and acceleration from a poppet valve secured on its cam through a spring. Firstly, the valve clearance needs to be closed before the valve begins its motion [10, 18]. Valve clearance is the space between the cam and the top of the valve stem and has a significant impact on valve loads and sealing [10]. This clearance must be highly controlled since if it is excessively small, the valves won't seat correctly, otherwise, greater loads on the valve gear will occur.

Initially, the cam is designed to supply a constant low valve velocity as the clearance is being closed in order to control impact stresses [10, 18]. Then, the cam accelerates the valve according to a function which accelerates the valve from rest to a maximum, returning to zero again, as shown in Figure 3.10. Once the valve reaches the maximum lift, the deceleration is managed by the valve spring. At the time that the valve begins to close, the last deceleration is controlled through the cam. Identically to the initial cam movement, the cam profile has to provide a constant closing velocity to keep within limits the impact stresses.

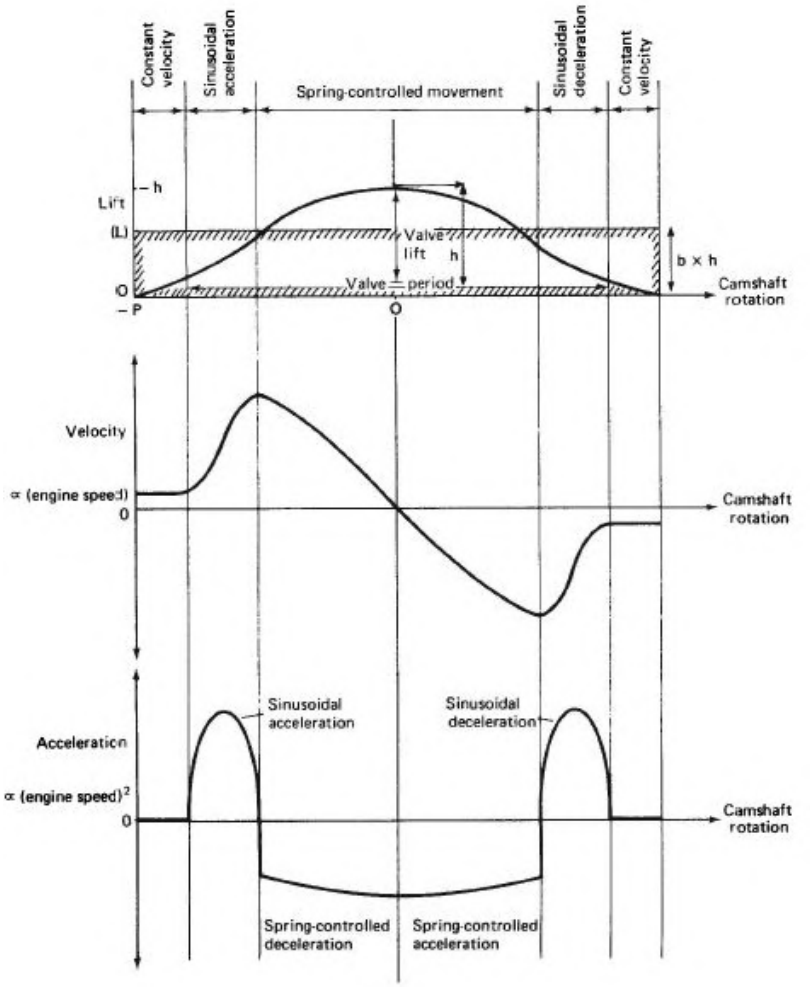

Figure 3.10: Theoretical valve lift, velocity and acceleration in function of the camshaft angle [10].

On the other hand, the actual valve motion is different from the theoretical due to the finite mass and stiffness of the components that belong to the valve train [10]. This disparity is highlighted in Figure 3.11 where both valve motions are superimposed.

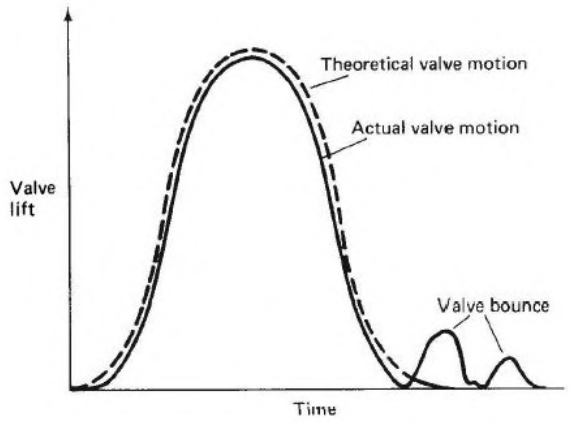

Figure 3.11: Differences between the actual and theoretical valve motion [10].

According to Figure 3.11, in the actual valve motion is possible to occur valve bounce which happens when the seating velocity is too high or whenever the pre-load from the spring is excessively low.

3.4.3 Valve timing

Relative to the valve timing, there is no universal criterion when it comes to set valve timing points. The valve timing is controlled by the engine camshaft and has an effect on engine performance and efficiency. Figure 3.12 depicts the typical valve timing diagram of a conventional and high-performance SI engine. It is noticeable that high-performance engines operate at higher speeds promoting the improvement of power and volumetric efficiency, while conventional engines run at lower speeds having the partial load performance and idle condition as a priority.

Moving clockwise around the diagrams, the intake valve opening (IVO) usually happens between 10º and 20º before TDC (BTDC) during the exhaust stroke [17]. From Figure 3.12 is clear that, in high-performance engines, the IVO occurs earlier than in conventional engines because it allows more mixture to enter inside the cylinder in the intake stroke since the valve is completely open at TDC, and also enables a gradual valve lift, avoiding valve bouncing which generally occurs at high speeds [37]. However, an early IVO also means a greater overlap period which can produce backflow of exhaust gases towards the intake manifold because of the high pressure within the cylinder when the piston is close to TDC. For conventional engines, minimization of valve overlap is a must to achieve an improved idle quality along with minimum idle fuel consumption [38]. This timing point by itself is not very important to performance, but can set constraints on the maximum valve lift and duration which, in some extent, can influence performance characteristics.

The IVC typically occurs in the range of 50º to 70º after BDC (ABDC) during the beginning of the compression stroke, as shown in Figure 3.12 [17]. This timing point is crucial to balance low and high-speed volumetric efficiency since it sets the maximum amount of mixture that enters in the cylinder, therefore, it has to be decided according to the desired engine performance features. So, the IVC of high-performance engines happens later than conventional engines to take greater advantage of the incoming charge inertia. In the case of conventional engines, where the operating speed is low, delaying the IVC will create backflow of the charge due to the pressure increase in the compression stroke [17]. On the other hand, if the IVC occurs too early a lower amount of mixture will enter into the cylinder.

The exhaust valve opening (EVO) normally takes place between 40º to 60º BBDC, this way, the pressure inside the cylinder drops near the exhaust pressure, reducing the required pumping work in detriment of the expansion ratio [7, 17]. In high-performance engines, the exhaust valve opens earlier than in conventional engines because an early EVO promotes a faster blowdown process which leads to a reduced pumping work during the exhaust stroke in comparison to conventional engines. The energy lost through the blowdown pays off the decreased pumping work in the exhaust procedure [37]. Opposingly, a late EVO will create additional work which can't compensate the increase in pumping work.

Lastly, the exhaust valve closing (EVC) typically occurs in the range of 15º to 30º after TDC (ATDC)

during the induction stroke [17]. The EVC is performed ATDC to avoid an increase in the cylinder pressure, which results in backflow of exhaust gases into the intake manifold [37]. Early EVC prevents the incoming charge to enter inside the cylinder due to the high pressure near TDC. This tendency is intensified at high speeds since there is no time to reduce the cylinder pressure. In contrast, a late EVC, in conventional engines, increases the backflow during the time that both valves are open due to the low operating speed. In the case of higher speeds, backflow during valve overlap reduces, owing to the fact that there is less time for backflow to occur [37].

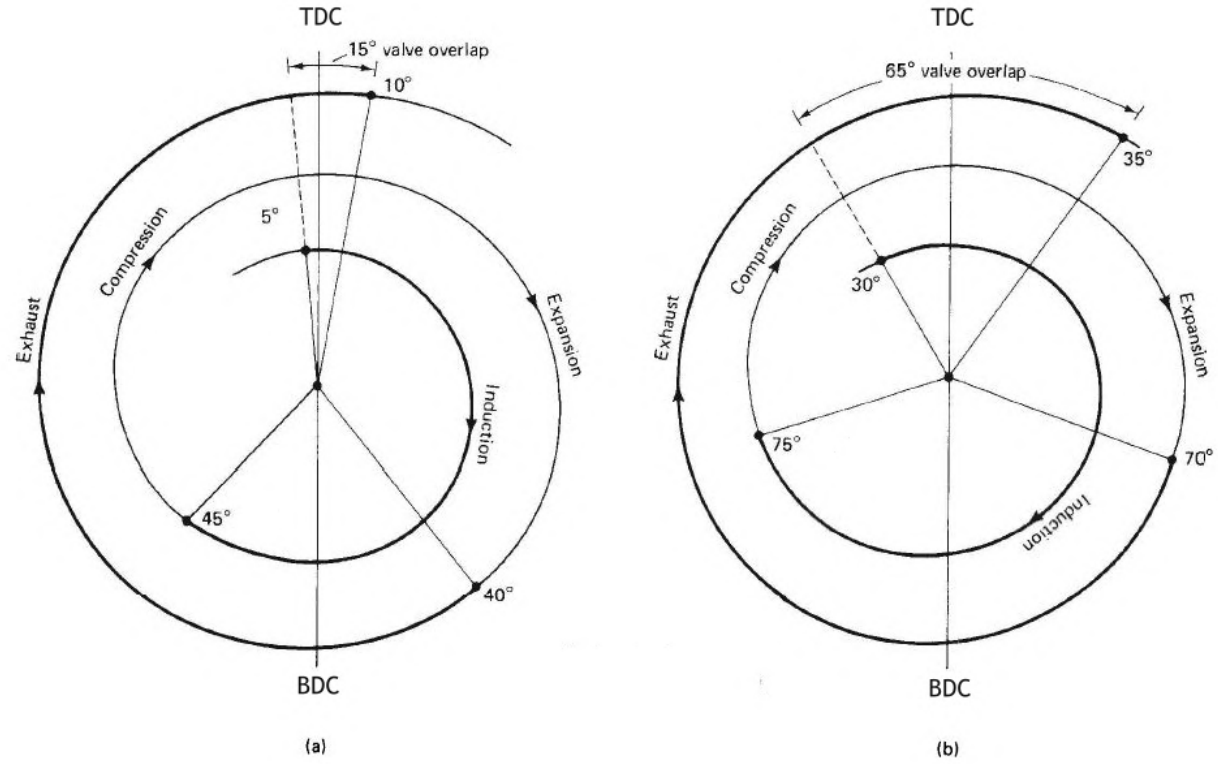

Figure 3.12: Valve timing diagrams. (a) conventional engine; (b) high performance engine. [10].

Generally, both inlet and exhaust valves remain open beyond the induction and exhaust time, so that, a better cylinder filling and scavenge can be achieved with the help of the gas inertia [17]. However, at WOT and with both valves being open, some short-circuiting of the intake charge to the exhaust will happen because the pressure in the inlet track is higher than the exhaust pressure in this condition [7]. As a result, engine performance at full load is reduced since some charge doesn't burn inside the cylinder.

Valve timing is usually set for one engine speed, below or above that speed, engine losses will happen [6]. The fact that valve timing is defined for one given speed imposes a barrier to ICEs since most engines operate at various different speeds. To counteract this drawback, engine engineers started to develop numerous procedures to obtain variable valve timing (VVT). The cheapest and easiest way to achieve VVT is known as cam phasing [18]. Cam phasing is normally used in double OHC engines since higher benefits are obtained due to the separated control of the intake and exhaust valves. This system modifies the valve timing by changing the phase angle of the camshaft, in other words, enables the engine valves to open and close at different

angles according to the engine load and speed [7, 10]. As a result, the duration of the valve action can be changed.

In Figure 3.13 is shown the variation of the valve lift in a camshaft set with cam phasing. During idle conditions, the intake camshaft is retarded to minimize the valve overlap period in order to decrease the backflow from the exhaust gases, achieving enhanced idle characteristics. At low engine speeds, IVC occurs earlier to promote greater volumetric efficiency and low-end torque, whereas at high speeds IVC is delayed, so that, the volumetric efficiency and engine power are increased [7, 18]. This way, improved flow efficiency and performance throughout the engine operating range is attained.

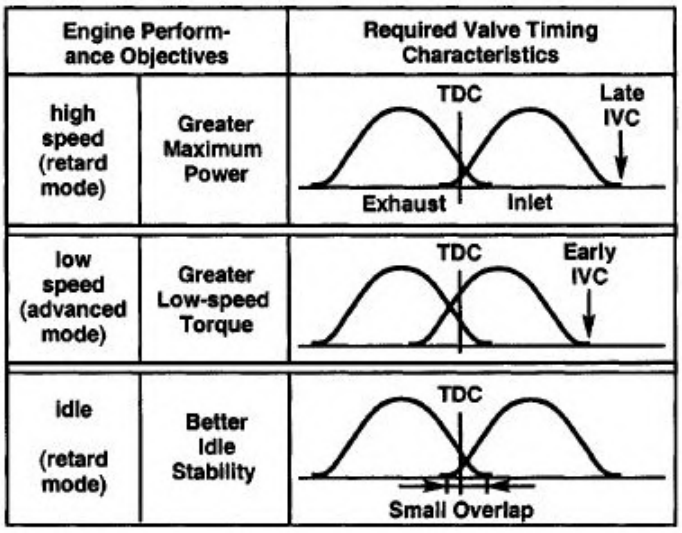

Figure 3.13: Valve lift due to cam phasing at different engine conditions [18].

3.5 Flow Parameters

When analysing a given intake or port-valve assembly geometry in terms of flow parameters, it is required to take into consideration some important ideas and definitions. Usually, it is recommended to use dimensionless ratios and coefficients when testing the geometry of the port-valve assembly or intake, since the size effects are removed from the results obtained experimentally, which results in a basis to other investigators compare their results [19]. This way, different valve, port and intake geometries can be easily analysed and compared. The basic geometry parameters of a poppet valve are represented in Figure 3.14.

As it is well known, during the engine cycle, there are some moments when fluid flows over an orifice. Generally, real flows are associated with an equivalent ideal flow in order to evaluate how close to the maximum efficiency a given flow is. In this equivalent ideal flow concept, a steady adiabatic reversible and frictionless flow flows inside a duct with the same geometry and dimensions of the real duct [8]. When considering the real flow, the deviation from the ideal assumptions is taken into consideration through a dimensionless discharge coefficient C_d [8].

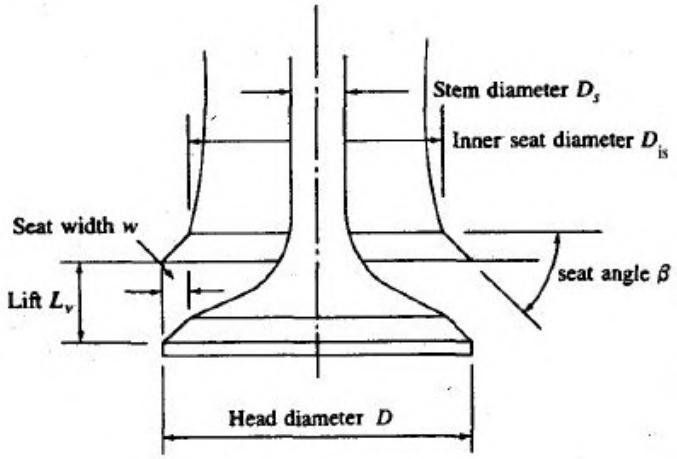

Figure 3.14: Geometry parameters of a poppet valve [8].

This way, the discharge coefficient can be determined by [8]

$$C_d = \frac{\dot{m_{act}}}{\dot{m}_i} \quad (3.4)$$

where

m_{act} is the actual mass flow rate in $\mathrm{kg/s}$.
m_i is the ideal mass flow rate expressed in $\mathrm{kg/s}$.

There are several ways to calculate the discharge coefficient, one of which, is through the one-dimensional isentropic flow analysis. From this analysis, it is possible to obtain the equation for compressible flow over a restriction [8]. In order to consider the real gas flow effects, it must be added to the compressible flow equation an experimentally calculated discharge coefficient $C_{d_{exp}}$. The experimental discharge coefficient is given by [8]

$$C_{d_{exp}} = \frac{\dot{m}_a}{\frac{p_0}{(RT_{int})^{1/2}} A_R \left(\frac{p_c}{p_0}\right)^{\frac{1}{\gamma}} \left(\frac{2\gamma}{\gamma-1}\left[1-\left(\frac{p_c}{p_0}\right)^{\frac{(\gamma-1)}{\gamma}}\right]\right)^{1/2}} \quad (3.5)$$

wherein

A_R is the reference area given in m^2.
p_0 is the static pressure upstream the restriction expressed in Pa.
p_c is the cylinder pressure in Pa.
γ is the specific heat ratio.

However, at high speeds choking will most likely occur, and when this happens, the flow rate stops increasing with engine speed, resulting in a severe reduction of the volumetric efficiency. In this condition, the experimental discharge coefficient is determined through the Equation

below [8]

$$C_{d_{chok}} = \frac{\dot{m}_a}{A_R \frac{p_0}{(RT_0)^{1/2}} \gamma^{1/2} \left(\frac{2}{\gamma+1}\right)^{\frac{(\gamma+1)}{2(\gamma-1)}}} \quad (3.6)$$

The choice of the reference area establishes the difference between the discharge and flow coefficient [1, 7, 39]. If the valve curtain area is considered, the discharge coefficient is obtained from Equation 3.5, whereas if the valve outer seat area is chosen, the flow coefficient $C_{f_{exp}}$ is determined by replacing the valve curtain area for the valve seat area in Equation 3.5. The valve curtain area corresponds to the region where the airflow is free to proceed and increases with the valve lift, being given by [8]

$$A_c = \pi D L_v \quad (3.7)$$

On the other hand, the valve seat area is obtained by [39]

$$A_s = \frac{\pi}{4} D^2 \quad (3.8)$$

The effective flow area of the valve A_e relates the discharge or the flow coefficient to the reference area and is determined by [8]

$$A_e = C_{d_{exp}} A_c \quad (3.9)$$

or

$$A_e = C_{f_{exp}} A_s \quad (3.10)$$

During engine operation, the flow rate that crosses each open area is intermittent due to the piston motion and is established by the pressure difference existent between the valve-port area and the cylinder [27]. As anyone would think, it is difficult to study and calculate the flow properties in the opening areas. However, it was verified through Bicen et al. [40] and Kastner [41] experimental works, that the actual flows obtained when the engine is running can be determined with good accuracy assuming that, at every instant, the flow rate will be equal to that calculated in steady conditions at the same opening and pressure difference. Thus, the inlet system performance is generally evaluated under steady flow conditions since steady discharge coefficients results are a good way of predicting the dynamic performance of the valve-port assembly. However, according to Heywood [8], the transition points between one flow pattern and another don't happen at the same valve lift under dynamic and steady flow operation.

Figure 3.15 presents the results of a flow test on a typical intake valve arrangement with a sharp-edged valve seat. From Figure 3.15 is clear that the discharge coefficient, established by the valve curtain area, is a discontinuous function of the valve lift/diameter ratio. It is possible to visualize three segments that correspond to different flow patterns across the valve shown in Figure 3.16. Still in relation to Figure 3.15, the dashed segments represent unsteady stages among the different flow regimes [18].

According to Figure 3.16, when the valve lift is low, the jet near the port drags fluid from the surroundings due to the fluid viscosity, reducing the local pressure which will displace the jet

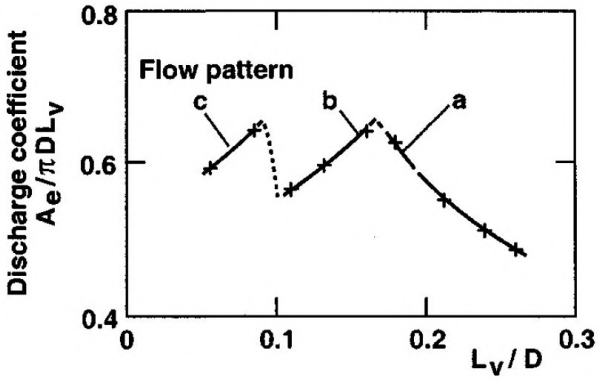

Figure 3.15: Variation of the discharge coefficient as a function of dimensionless valve lift for a sharp-edged intake valve [19].

towards the valve head and seat, reattaching the flow if it is close enough [19]. This effect is shown in Figure 3.16 (c), where the fluid separates at both valve seat and head after crossing the sharp inner corners and then reattaches filling the seat gap. During this lift stage, high values of discharge coefficient are obtained [8]. At intermediate lifts, the flow breaks away from the valve head surface but reattaches to the seat. At this point, the discharge coefficient drops sharply, as revealed in Figure 3.15, and then increases as the valve lift gets higher because the area of the separated region stays approximately the same whereas the minimum flow area gets greater [8]. At high valve lifts, the fluid flowing along the inner edges of the seating can't follow around the sharp edges due to its inertia, so the flow separates from the surface to create a free jet, as shown in Figure 3.16 (a). In this valve lift condition, the discharge coefficient decreases, as indicated in Figure 3.15, due to the flow separation at both surfaces. It is noteworthy that increasing the valve lift beyond a certain point (L_v/D = 0.25) doesn't increase the flow across the valve since the flow area over that threshold is limited by the port size [7].

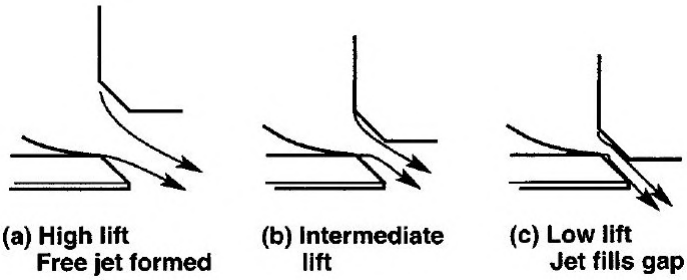

Figure 3.16: Flow patterns through a sharp-edged intake valve [19].

Figure 3.17 shows the effect of Reynolds number variation on the discharge coefficient to the three previous valve lift conditions. During high and intermediate lift stages, viscosity contributes little or nothing to the flow pattern, therefore, the discharge coefficient is almost independent of Reynolds number. In contrast, at low lifts, viscosity does play an important role in establishing the flow patterns, this way, the discharge coefficient is somewhat affected by the Reynolds number, as exposed in Figure 3.17. The variation of Reynolds number also changes the lift at which the transition among flow patterns occur [19].

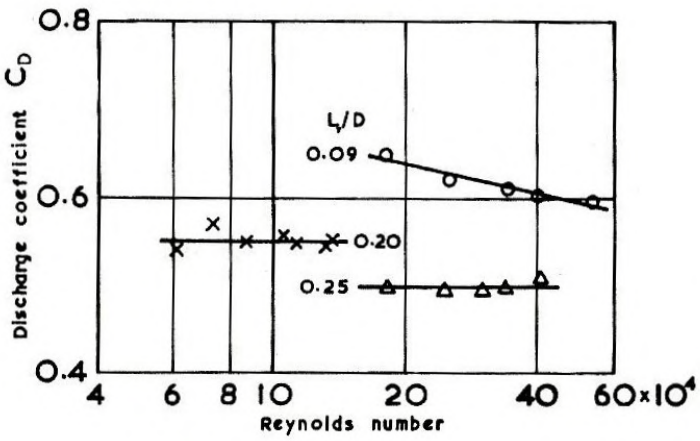

Figure 3.17: The effect of Reynolds number on the discharge coefficient of a sharp-edged intake valve [19].

3.6 Related works

Throughout the years, several experimental and numerical tests have been performed with the aim to determine the discharge and flow coefficients of a given valve-port assembly in order to measure engine breathability. The majority of those studies were carried out in steady flow rigs, where the pressure drop through the intake valve is kept constant and the valve lift is fixed. The unsteady flow case, in its turn, is less investigated in experimental tests due to the higher degree of complexity in simulating the piston and valve motion of an engine. Nevertheless, some numerical and experimental studies under dynamic conditions were performed and some important discoveries were made. The following studies presented will corroborate prior statements and expose new findings about this subject. Both experimental and numerical studies will be shown to verify the agreement between the results obtained by each method.

Recently, Oh and Lee [42] measured the flow coefficient in the intake port of a cylinder head under unsteady operation conditions. Their measurement system had some differences in relation to the traditional one, since the camshaft is driven by a step motor instead of a micro-meter controlling the valve lift and the surge tank pressure instead of being kept constant is changed continuously with the valve lift. Their experimental setup, presented in Figure 3.18, consisted of a blower that sucks air into the intake port and valve, where the lift is adjusted by the camshaft, and then it proceeds to the cylinder and surge tank. The pressure drop was measured with a differential pressure transducer, an encoder was used to obtain the camshaft angle and the valve lift was measured using a linear variable differential transformer sensor. All data were collected using a data acquisition board and a computer. In all tests performed, the blower operated at its maximum speed and the step motor rotated at a constant speed. The camshaft speed was set to 10, 20, 30, 60,120 and 180 rpm and the valve lift varied from 0.15 mm to 8.5 mm according to the camshaft angle. Results show that, at the lowest camshaft speed, the flow coefficient achieves its maximum value and as the rotation speed increases, the maximum value of the flow coefficient decreases. In addition, the intake flow inertia effect on the flow coefficient is presented, increasing as the rotation speed of the camshaft gets bigger. The authors conclude that when the camshaft speed is constant the flow coefficient increases with the valve lift.

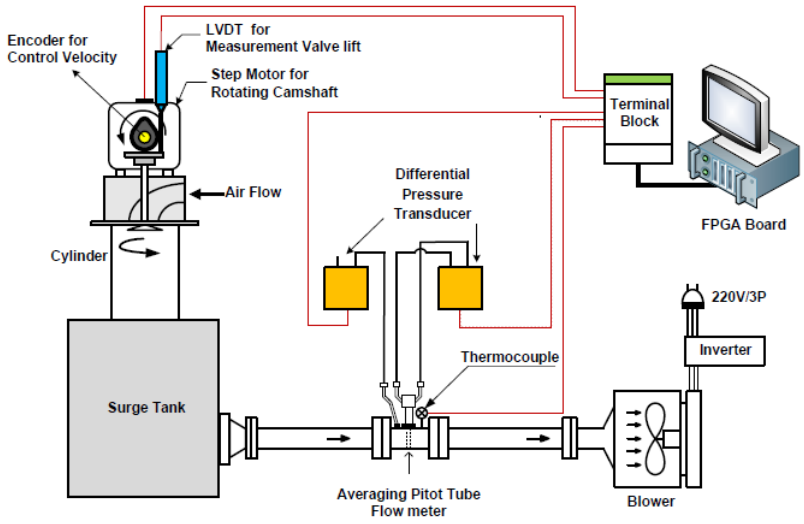

Figure 3.18: Experimental apparatus for flow coefficient measurement [42].

The effect of valve lift and throttling on engine breathability was investigated in experimental studies performed by Algieri [1, 43]. In the first study, the author analyses both inlet valves open and also investigates alternative intake strategies such as valve deactivation and asymmetric valve lift arrangements. The experimental study was carried out at a steady flow rig and dimensionless flow and discharge coefficients were adopted to define engine breathing. At the steady rig, a blower creates the air motion throughout the intake system and the valve is fixed to a given value. The pressure drop between the cylinder and outside was kept at 8.3 kPa and the dimensionless valve lifts varied from 0.059 to 0.294. Results show that, at WOT with both valves equally open, a gradual increase in the flow coefficient is verified as the valve lift grows, whereas the discharge coefficient decreases from a certain dimensionless valve lift value. This result was also obtained experimentally and confirmed numerically by Soriano et al. [44] and Costa et al. [39] investigations. Furthermore, it is clear the presence of different flow regions in the discharge coefficient results.

Regarding the throttling processes, several throttle positions were studied and again the fluid dynamic parameters were calculated. Figure 3.19 shows the values of flow (a) and discharge (b) coefficients for several throttle positions with both inlet valves open. Experimental results show identical variations from both coefficients for the different throttle angles analysed. From the results obtained in this condition, the author confirms that the transition from a flow condition to another is achieved at lower valve lifts if the flow is throttled and, as it is expected, a gradual reduction of the engine breathing occurs when the throttle plate angle decreases. These results were also obtained in Algieri's second work [43], even though, the inlet conditions and the range of valve lift were different. In relation to the valve deactivation strategy, the results obtained by the author demonstrate the presence of the different flow regimes and highlights the absence of flow interference between the two intake valves. This leads to a better cylinder filling, at low and intermediate loads, whenever only one inlet valve is opened. Finally, the asymmetric lift case is investigated in a WOT condition, where it was found that high fluid dynamic efficiency is maintained, even when the mass flow rate significantly reduces. From all results, the author suggests that when lower mass flow rate is required, the asymmetric lift strategy should be

implemented and whenever the engine load is very low the valve deactivation configuration should be adopted.

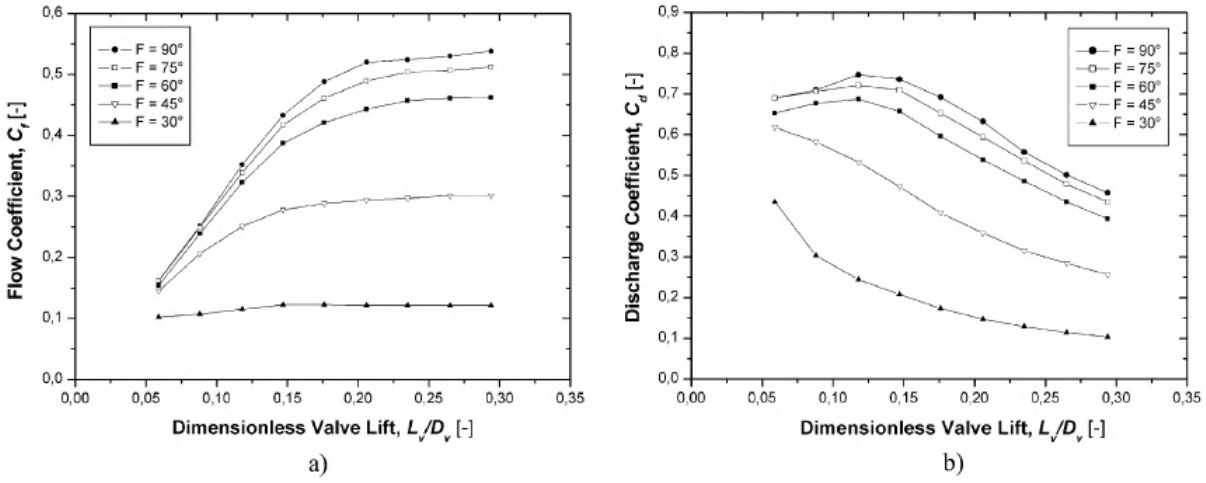

Figure 3.19: Throttle effect on the flow (a) and discharge (b) coefficient with both valves open [1].

Another review regarding the effect of valve deactivation on the head permeability and the interference phenomena between inlet valves was conducted by Algieri [45]. In this study, the global fluid dynamic efficiency of the intake system was established by means of dimensionless discharge coefficients, while the analysis of the mean flow velocity within the valve curtain area and the interference between valves was performed using the Laser Doppler Anemometry (LDA) technique. The induction system of a high-performance multi-valve ICE was analysed at a steady flow rig, where air is forced to move throughout the intake track by a blower and the valve lift is fixed. The measurements of the dimensionless discharge coefficients were obtained in a WOT condition for a fixed pressure drop of 7.3 kPa and for a range of dimensionless valve lifts between 0.050 and 0.400. Results show that, when one intake valve is open, the interference between valves is eliminated, leading to an improved filling of the cylinder whenever the dimensionless valve lift is smaller than 0.275. For greater lifts, the both inlet valve open configuration obtains the best results. When the flow distribution in the valve curtain area was investigated, the pressure drop was set to 7.3 kPa, the dimensionless valve lift was fixed at 0.375, the measuring plane was placed at 3/4 of the valve lift and the WOT condition was considered. Results show a considerable distortion of the flow field and a notable decrease in the flow velocity intensity when both valves are open, in contrast with the one intake valve arrangement.

Soriano et al. [44] performed an experimental and numerical investigation of a cylinder head under steady flow conditions in order to find out if the discharge coefficient depends on the suction pressure. In this study, the experimental rig consisted of a fan which created a suction pressure, a hot film anemometer to measure the airflow, a rotary encoder to provide the angular position of the camshaft, a length gauge to measure the valve opening and a data acquisition board. For all study cases, three different suction pressures: 6000, 8000 and 10000 Pa were investigated and for each suction pressure, three different valve lifts were studied: 1, 2 and 2.5 mm. Regarding the numerical investigation, the numerical solution was achieved with FLUENT 14, using the k-epsilon standard turbulence model together with a high Reynolds approach. The boundary condition defined at the outlet was the experimental suction pressure and at the

intake was the atmospheric pressure. The experimental results show some small dependence of the discharge coefficient on the suction pressure in the lower valve lift studied. However, for the other two greater valve lifts, the discharge coefficient became independent of the suction pressure. These results were also proved in Tanaka's experimental work [46], Bicen et al. study [40] and in Pajkovic and Petrovic review [47]. The numerical results show a good agreement with the experimental ones and reveal the existence of a large recirculation area, as seen in Figure 3.20, induced by the valve downstream low pressure in all valve lift and suction pressure tested. This recirculation causes an irregular distribution of the flow across the valve gap, leading to a reduction of the discharge coefficient.

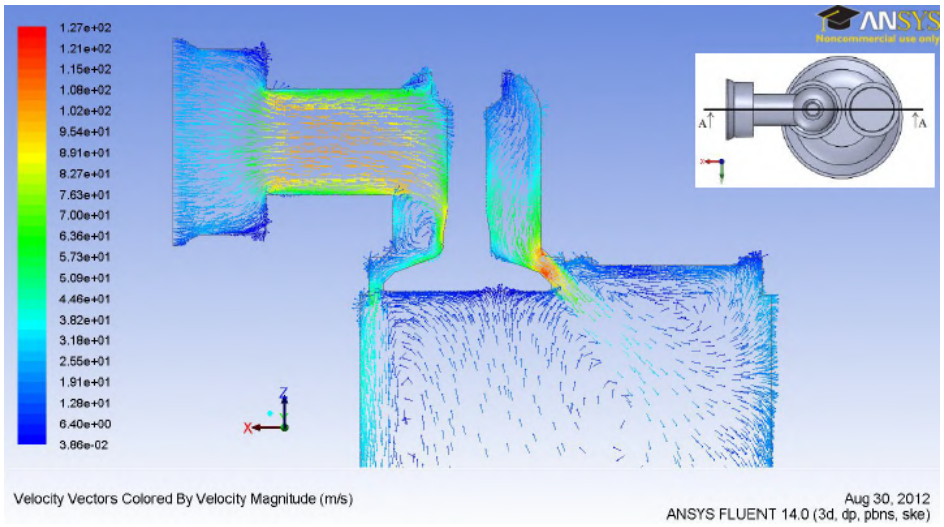

Figure 3.20: Velocity vectors through the port-valve assembly at 2.5mm valve lift [44].

An experimental study to calculate the discharge coefficient through one steady and three unsteady configurations along with three different valve geometries was carried out by Bicen et al. [40]. In this investigation, a detailed measurement of the velocity field was achieved by means of LDA for the steady and unsteady configurations considered. The static setup consisted of a steady flow section supported on a plenum chamber that was linked to a compressed air supply. The first unsteady configuration adopted the same previous test section of the steady setup which was attached on an engine with the piston moving at 200 rpm within the cylinder upstream of a static valve. The two other unsteady arrangements consisted in simulating a real engine with the piston moving inside a cylinder downstream of the valve. In one of these last configurations, the valve was fixed open, whereas in the other arrangement the valve was operated by a camshaft. Regarding the three valves considered, the first one had a 45º seat angle and sharp corners, the second also had sharp corners but the seat angle was 60º, and lastly, the third had a 45º seat angle with rounded corners. For the steady case, a constant mass flow rate of 12 kg/s was defined and the pressure upstream the valve was the stagnation pressure inside the plenum, while the pressure downstream the valve was assumed to be atmospheric. The steady results for the first valve type indicate the existence of four different flow regimes. The extra flow regime happened at a valve lift of 6.5 mm, where the flow reattached only on the valve head after separating from it during the previous flow regime. This result is in line with Tanaka's results [46] since four flow regimes were also identified in his experiment when a sharp corner inlet valve with 45º seat angle was tested. Pajkovic and Petrovic results [47], shown in Figure 3.21, also support the existence of four flow regimes, even though, a 35º seat

angle was adopted in the used intake valve. In contrast with the first valve analysed, the results of the second valve type in the steady configuration demonstrate the presence of the three conventional flow regimes. Rounding the corners of the valve and seat decreased the number of flow regimes to only two and also improved the discharge coefficient up to 15%. In relation to the three unsteady configurations, the results were compared to the data obtained under steady condition, where it was discovered that the discharge coefficients obtained in both flow conditions were similar to each other. The results obtained by Kastner et al. [41] also verifies this previous statement. The authors conclude that the overall results of the 45º seat valve were better than the 60º seat angle during the low to medium valve lift range and the flow across an intake valve under engine operating conditions can be predicted reasonably well through steady flow measurements.

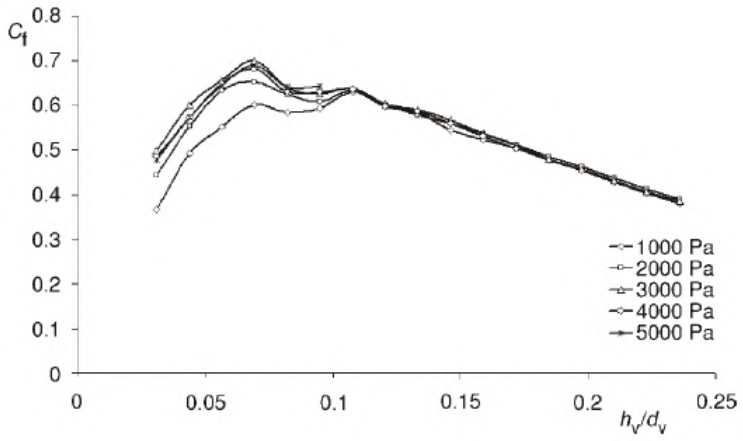

Figure 3.21: Discharge coefficient evolution for different pressure drops in function of dimensionless valve lift [47].

Fukutani and Watanabe [48] studied the discharge coefficients and mean effective areas of poppet valves during steady and dynamic flow conditions in two engines with different displacement volume by varying, over wider limits, the angle-areas and opening periods of the valves. In their experiment, several inlet cams were used, some were changed to maintain the same inlet valve angle-area by changing the valve lift and opening period, and others were modified to reduce the angle-area through the decrease of valve lift. The test rig consisted of two reservoirs one connected to the cylinder head and the other to the cylinder. The former is kept at atmospheric pressure during the experiment by varying the speed of the centrifugal blower, whereas the latter changes the pressure using a roots blower and a bypass valve, resulting in several flow rates across the inlet valve. During the static condition, the pressure ratio was fixed at 0.97 and, for the unsteady case, the intake valve was operated by a camshaft which was controlled by a variable speed motor and the pressure ratio across the valve was fixed.

The static results show that when the angle-area is kept constant in each engine, the intake valve which has the shortest maximum valve lift has a tendency to obtain a greater static mean discharge coefficient. Regarding the dynamic data, it was discovered that the dynamic mean discharge coefficient reduces with an increase in the engine speed and a decrease in the pressure ratio. It was also noticed from the results that the engine which had the smaller displacement volume will most likely achieve the larger dynamic mean discharge coefficient throughout all engine operating speed range, whenever the pressure difference through the valve is constant.

The authors noticed the presence of valve bounce in the dynamic results due to the sudden increase in the dynamic mean effective area and the sudden upsurge of the volumetric efficiency when the engine speed was high. Furthermore, the authors suggest reducing the maximum inlet valve lift through the enlargement of the valve diameter or by adopting several inlet valves in order to enhance airflow characteristics under both flow conditions.

An experimental investigation to evaluate the flow characteristics of several different inlet valves tested under three distinct conditions was carried out by Kastner et al. [41]. In the first condition, the valve was fixed for each valve lift and pressure drop was kept constant to each lift. For the second case, the pressure drop was also kept the same for each test, but the valve was operated through a camshaft at several rates. In the final condition, the airflow was created by the descending piston motion instead of setting a fixed pressure drop throughout the intake system. In their experimental rig, air provided by an air compressor flows into reservoir tanks and then into a damping reservoir, where a flow meter and a bypass valve is placed upstream of the second reservoir. After the damping reservoir, the air flows through a curved port to the test valve and, after the valve opens, to the atmosphere. For the steady test, each valve was studied up to an 8.89 mm valve lift and a pressure drop of 5000 Pa. Regarding the dynamic conditions, the camshaft speed varied from 400 to 3500 rpm by means of an electric motor. In relation to the third condition, the valves were tested under similar engine conditions, in which, the valve lift and pressure drop varied continuously according to each valve used and the overall speed range of the camshaft was established between 1000 and 4000 rpm.

The static results show that the mass flow rate across a poppet valve can be increased until 20% if the edges of the seating faces are rounded off. The dynamic results, in its turn, demonstrate that when the camshaft speed is low, a greater rate of flow than that foreseen in the static tests occur. The authors indicate that this fact happens because of changes in the flow pattern, which result in transition points between different flow regimes at valve lifts that are different from those where the transition points were found during the static tests. For high camshaft speeds, the unsteady results prove that the rate of flow reduces due to the loss of energy which is used to accelerate the air in the port of the valve. The authors recommend the use of a large port area, around 3 or 4 times the valve area, and a tapering of the port in order to minimize the loss of energy.

3.7 Design of ports and valves

At the designing stage of valves and ports, some important aspects to improve engine breathability and efficiency are required. Generally, the intake valve has a larger diameter than the exhaust valve in order to allow sufficient air-fuel mixture into the cylinder. Since the pressure differential caused by the piston downwards motion is not that high, a larger inlet valve diameter is required to facilitate the entry of a greater amount of airflow into the engine. The exhaust valve, in its turn, is kept smaller to avoid pre-ignition and knocking. The performance of the inlet valve gear is affected by the valve seat width, valve seat angle, valve lift, port design, rounding the seat edges and the cylinder head shape [8]. These factors will be discussed and analysed ahead in order to properly design an intake port and valve.

Figure 3.22 demonstrates several seat angles and seat width configurations and also their influ-

ence on the discharge coefficient of a sharp-edged intake valve. Focusing firstly in Figures 3.22 (a) and (b), is clear that the discharge coefficient gets bigger with the reduction of the seat width. In addition, as the seat width varies, the valve lift at which there is transition between flow regimes changes [8]. Regarding the seat angle, for the minimum seat width, the 30º seat angle configuration obtains the best overall results against a 45º seat angle setup, as shown in Figure 3.22 (d). When comparing both seat angles for different seat widths the same prior conclusion is valid only for low valve lifts. The discharge coefficient is also slightly affected by the shape of the upstream surface of the valve head. Several experimental tests proved that an increase of this angle, enhanced the discharge coefficient at low lifts, but worsened it at high valve lifts [19]. Therefore, an angle of 10º is defined as being the best compromise [19].

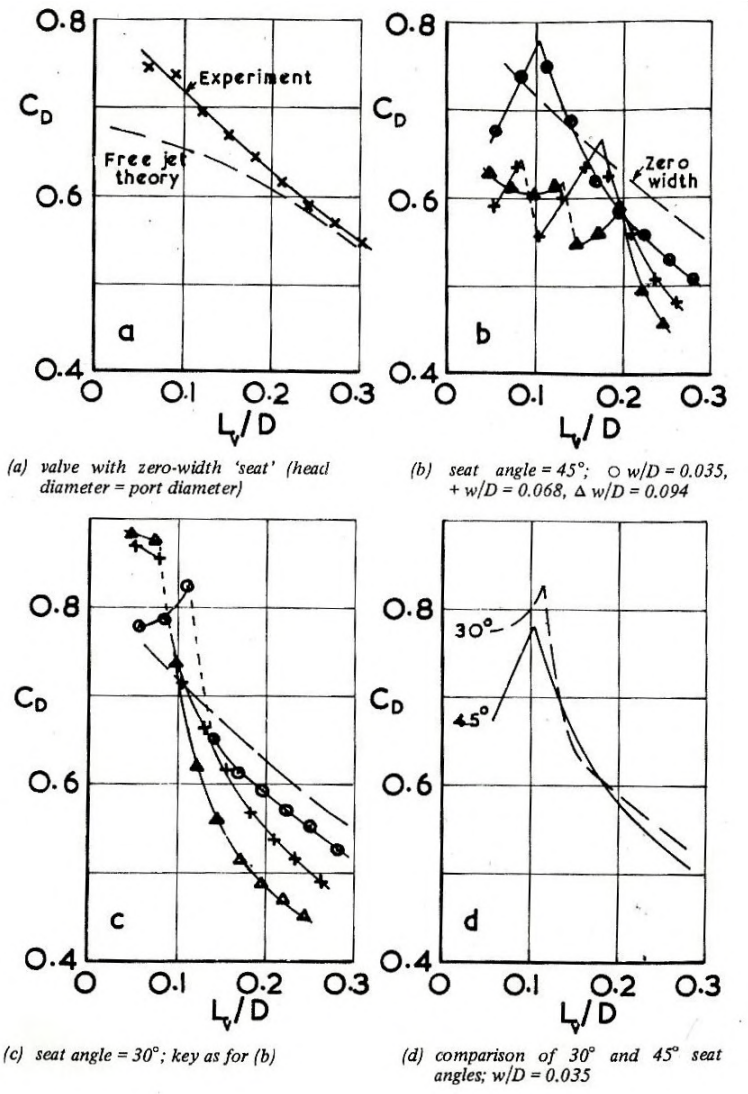

Figure 3.22: The effect of the seat width and angle variation on the discharge coefficient of a sharp-edged inlet valve [19].

In Figure 3.23 is shown the effect of rounding the corners of an intake valve with a 45º seat angle. It is known that the flow will have a tendency to break away on corners 1 and 3 of Figure 3.23 (a) due to its inability to get around sharp edges. So, rounding the edges of the

valve seat and head appears as a way of reducing the flow separation tendency and increasing the discharge coefficient at high lifts. Taking into account Figure 3.23 (b), it is proved that rounding the corner 1 is advantageous and the best result is achieved with a radius of roughly 0.25D. Rounding corner 3, in its turn, is not clearly stated due to some apparent disagreement among experimental tests , as shown in Figures 3.23 (c) and (d). Nevertheless, it was found that a radius configuration of 0.05D produces some improvement on the discharge coefficient at low valve lift. When corner 2 is rounded the discharge coefficient is enhanced only throughout a limited range of valve lifts, as exposed in Figure 3.23 (e). In relation to corner 4, it is rounded occasionally but no major impact on valve performance has been proven.

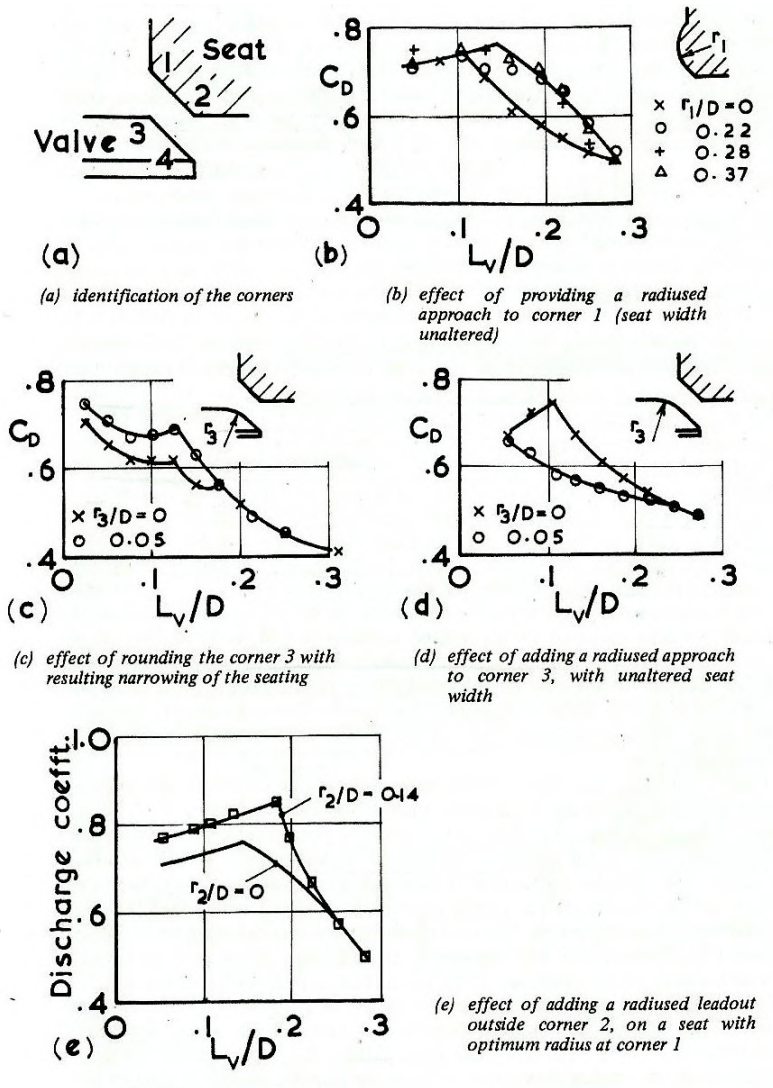

(a) identification of the corners

(b) effect of providing a radiused approach to corner 1 (seat width unaltered)

(c) effect of rounding the corner 3 with resulting narrowing of the seating

(d) effect of adding a radiused approach to corner 3, with unaltered seat width

(e) effect of adding a radiused leadout outside corner 2, on a seat with optimum radius at corner 1

Figure 3.23: The impact of rounding edges on the intake valve seat and head with a 45° seat angle and w/D=0.035 [19].

The inlet port also influences the discharge coefficient, thus, it must be designed according to some principles. Firstly, the surface radius within the bend has to be sufficiently large and shouldn't have any sort of interruption [19]. Secondly, the area of flow passage should be much greater in the valve guide section than at the end from the bend [19]. There are several advantages of doing this: it decreases the flow velocity through obstructions, enhances the

flow pattern inside the bend and accelerates the flow in the direction of the valve, resulting in a reduction of the wake created by the valve stem and guide. Figure 3.24 shows three different design configurations of intake ports and their effect on the discharge coefficient. According to Figure 3.24, the best configuration is the one which meets the principles outlined. Any deviation from these principles will result in a reduction of the discharge coefficient.

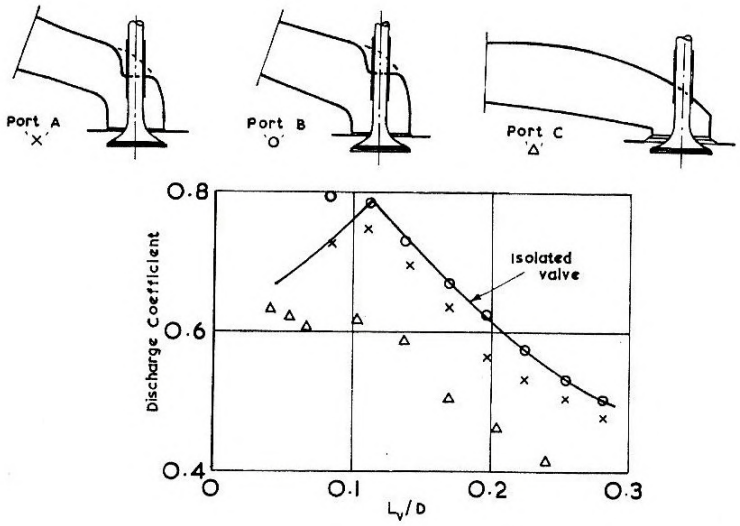

Figure 3.24: Intake port designs [19].

The previous design principles and statements discussed until now are applied to configurations, where the discharge coming out of the valve is entirely unobstructed [19]. From experimental tests, it was concluded that the restriction created by discharge into a cylinder with conventional valve and cylinder dimensions together with the normal offset of the valve axis from the cylinder axis, has a negligible impact [19]. Therefore, the principles defined may be adopted in real configurations.

The combustion chamber design and considerations of the dynamics of the valve train have an impact in the maximum opening area of a poppet valve [19]. In both cases, the goal of reducing resistance to a minimum entails the utilization of the maximum accessible area during all opening stages. In an ideal case, the gas flows at the same velocity across each part of the open area [19]. As ideal conditions are impossible to achieve, the best we can do is get as close to these conditions as possible in order to attain the maximum discharge coefficient at each engine condition. When doing this, we can't forget the other functions of the arrangement, for instance, the flow pattern resulted from the intake valve will influence the combustion procedure, thus, a compromise has to be made between the valve requirements and the reduction of flow resistance.

In some engines, the port-valve assembly is designed to create a rotational movement (swirl) within the cylinder in the intake stroke to improve combustion. A way of creating swirl is to add a mask or shroud to the valve, so that, a portion of the peripheral opening is blanked off [19]. Figure 3.25 demonstrates the effect of adding shrouds of different angles on the discharge coefficient. According to Figure 3.25 is evident that the discharge coefficient decreases when some shrouding is done to the inlet valve. A possible explanation to this can be the production of vortices in the open area of the valve by the shroud which, on one hand, improves the

air and fuel mixing and the intensity of the turbulence inside the cylinder, leading to better combustion and emissions, but on the other hand, it offers a greater restriction to the flow which strongly contributes for the reduction of the discharge coefficient. In order to counteract this drawback, distinct ports designs have been developed and analysed to provide different air distribution over the valve periphery. It turns out that a helical port shape offers the best discharge coefficient results together with a good swirl when compared with shrouded valves and other ports configurations [19].

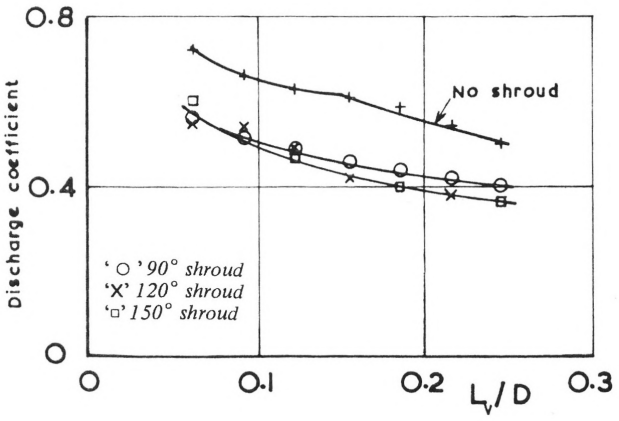

Figure 3.25: Discharge coefficient variation when shrouds of various degrees are added to the inlet valve [19].

The design of the valve gear is largely dictated by the need to avoid choked flow throughout the desired performance range. Chocking is a major performance limiting factor of engines which generally happens at high engine speeds. Thus, current engines have mounted multiple inlet and exhaust valves to counteract choked flow since chocking arises from restrictions in the valve flow area. A multiple valve configuration produces more flow area and less flow resistance in comparison to a large intake valve. This way, higher volumetric efficiencies are attained with this setup at the expense of a bigger complexity in terms of design since more camshafts and mechanical connections are needed.

Chapter 4

Experimental work

This chapter describes the required components for the experimental tests, the designing of the test bench and auxiliary elements, the entire set of steps to build and assembled the different components, as well as the different obstacles encountered which lead to several modifications.

4.1 Components

In order to successfully perform the proposed laboratory tests, some elements and equipment were required.

4.1.1 Engine

The most obvious is an engine since without it the measurement of the discharge and flow coefficients are impossible to obtain. The engine chosen for the tests is a multi-valve four-stroke SI engine with the specifications presented in Table 4.1. This engine was selected because it makes it possible to carry out different valve lifting strategies and the original intake manifold was available, unlike the two other accessible engines.

Table 4.1: Engine technical specifications [49].

Engine type	Naturally aspirated SI
Cylinders	Straight 4
Stroke / Bore	0.909
Bore x Stroke [mm]	79 x 71.3
Number of inlet valves per cylinder	2
Head diameter of the intake valve [mm]	31.5
Inlet valve seat angle [°]	45
Valve gear	DOHC
Number of valves per cylinder	4
Capacity [cm^3]	1400
Compression ratio	10.5:1
Maximum power output [hp]	97 at 6000 rpm
Maximum torque [Nm]	130 at 4400 rpm

4.1.2 Sensors

Throughout the experimental tests, several sensors were used to ascertain the intake-cylinder conditions which will allow the measurement of the discharge and flow coefficients in the consid-

ered intake strategies. In total four sensors were used, two pressure sensors, one temperature sensor and a mass air flow (MAF) meter. Described below, in a summarized form, are the specifications and the working principles of each utilized sensor.

Thermocouple - The MAX6675 thermocouple and the associated module were used in the experiment to measure the intake temperature. The thermocouple consists of two wire legs, one positive which is non-magnetic and a negative that is magnetic, which are welded together at one end [50]. The MAX 6675 thermocouple module converts the signal from the thermocouple into a voltage using a diode which senses the temperature. Then, it measures the output voltage from the thermocouple and the diode which are used on a temperature conversion function that calculates the actual temperature at the welded end [51]. The operating range of -270 ºC to 1260 ºC and tolerance class of $\pm$ 1.5 K between -40 and 375 ºC together with its small size, low cost, fast response time and reliability were the reasons to select this type of temperature sensor for the experiment [50].

MAF sensor - A hot-wire MAF sensor type HFM 5 was chosen for the measurement of the air mass that enters into the intake manifold. This sensor has an electrically heated wire which is heated by a constant voltage and is in contact with the inlet air. As the air flows through the wire, it cools and its resistance decreases, resulting in an increase of current to heat the wire until its resistance is balanced again. This current variation is proportional to the airflow moving past the wire. The specifications of the hot-wire MAF sensors type HFM 5 made by Bosch are shown in Appendix A . The MAF sensor utilized didn't have a part number and there were 5 MAF sensors in the technical sheet. In order to choose the right one, the inside diameter of the sensor was measured, leading to a match. The MAF sensor with the following part number 0 280 218 019 revealed to be a match and so, the features and specifications of this MAF sensor were considered to be equal to the MAF used in the experiment.

Manifold Absolute Pressure (MAP) sensor - The intake and cylinder pressure were measured using two PBT-GF30 MAP sensors. This type of sensor is usually utilized in the automotive industry to measure the inlet air pressure, being typically located inside the intake manifold. This sensor has as reference the absolute vacuum, therefore, it allows pressure measurements above or below the atmospheric pressure. This way, it creates a signal proportional to the intake manifold vacuum which is converted to pressure.

4.1.3 Stepper motor

The static tests required that both inlet valves were open at certain valve lifts. Once the desired lift is reached, it needs to be held constant for some time in order to obtain the intake-cylinder conditions at that lift. To successfully perform these steady requirements, a high torque stepper motor was used due to its high precision, low-speed torque and repeatability. The chosen stepper motor was the Nema 23 which, in order to work properly, required a controller that can withstand higher current than the maximum current of the motor. The stepper motor driver utilized was the TB6600 v1.2 since it fulfilled the previously stated condition. The specifications of both devices can be found in Appendix C. The stepper motor was also used during the dynamic tests since it was able to reach the desired speeds for this condition.

4.1.4 Power supply

The MAF sensor, as well as the stepper motor, required more voltage to work properly besides the 5V provided by the Arduino. Only one power supply was available in the department and it couldn't provide the requirements set by the stepper motor. Thus, a custom power supply based on an old pc power supply was developed and built for this purpose. This custom power supply relies on a buck converter, which decreases the voltage and, at the same time, increases the current from its input to a variable output. The specifications of the buck converter and the old pc power supply are presented in Appendix D. Besides the variable output, the power supply also has the following five fixed outputs +3.3V, +5V, -5V, +12V and -12V.

4.1.5 Toothed belt-gear system

Due to the extremely high stiffness of the original engine springs, it was decided to use a belt-gear system in order to obtain higher torque at the expense of velocity. The high torque set by the stepper motor forced the installation of a tensioning system to ensure that the belt is always tensioned. A small pulley was fixed into the stepper motor shaft and a medium pulley, as well as a big gear, were obtained to be fixed in the shaft connected to the camshaft in the case that more torque was needed. Two toothed belts were considered due to the two existing possibilities. Further information about the specifications of the belts, pulleys and gear used can be found in the Assembly section.

4.1.6 Suction machine

In order to characterize the flow that flows through a valve, it is required to force the airflow into the cylinder. This can be achieved by using a blowing or a suction system. Regardless the chosen way, the results are believed to be the same at least for the steady flow tests [52]. For convenience, a suction system was adopted and used during the experimental tests. This system consists of a Karcher A 2054 vacuum cleaner with 1400 W as maximum power provided by the department that is connected to the bottom of the engine cylinder, which is sealed, to create a pressure difference between the cylinder and the intake.

4.1.7 Arduino Uno

The collection of the sensors data and the control of the stepper motor were achieved through the Arduino software which allows the user to write code and upload it to an Arduino board. Two Arduino Uno boards were required for both test conditions since it was not possible to control the stepper motor and, at the same time, collect the sensor data using only one Arduino.

4.2 Parts Design

After identifying the required components for the proposed tests, it is time to proceed for the design of the test bench and some important parts that will allow the experiment to be performed. The design of the intended parts and the test bench was made using the Computer-Aided Design (CAD) software CATIA V5R20 developed by Dassault Systèmes. During this designing stage, some major design adjustments were made in the test bench and in the stepper motor support, due to the heavy load that these components were subjected to. Described below,

there is a brief summary of each designed element, where key information about their design and role in the experiment are presented. Further details such as the 3-view drawings as well as dimensions of each designed element can be found in Appendix E.

4.2.1 Shaft support

A proper shaft holder was needed since a toothed belt-gear system will be used to transfer the rotating motion of the stepper motor to the camshaft through a shaft connected to the camshaft. In order to balance the shaft, two shaft supports were required and, in each shaft holder, a hole for a 30mm diameter bearing was added to reduce shaft friction. Furthermore, these shaft supports needed to be fixed to a platform with the proper height for the shaft to be aligned with the camshaft connecting point. Thus, two holes for screws were added to the sketch and the final result is shown in Figure 4.1.

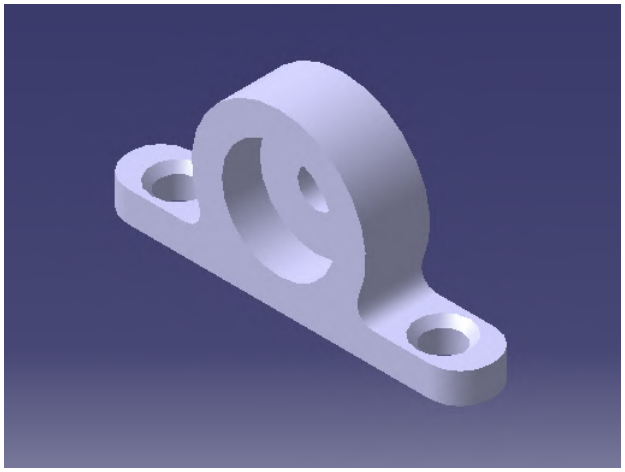

Figure 4.1: Shaft support isometric view.

4.2.2 MAF-throttle holder linkage

A linkage element to be placed between the MAF sensor and the throttle holder was designed due to the impossibility of joining both parts and the big diameter difference between them. As a result of the diameter difference, a progressive increasing convergent section throughout the entire length of the developed part had to be made. This element was made with a considerable length, so that, the airflow wouldn't be affected by a quick and large section variation. Both ends of the developed part have slightly larger diameters than the respective part to be joined since the ends are designed to fit on the outside surface of the MAF sensor and the throttle holder. The final result is shown in Figure 4.2.

4.2.3 Throttle plate set

In order to evaluate the effect of a carburettor on the head permeability, it was designed a holder and a throttle plate that fits inside the holder. The holder, in its turn, is connected to the inlet manifold at one end and to the MAF-throttle holder linkage on the other end, in order to limit the amount of air that goes into the cylinder. The throttle holder was designed to have

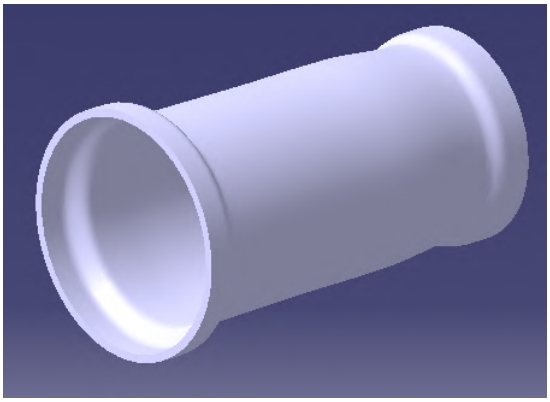

Figure 4.2: MAF-throttle holder connecting element isometric view.

the same shape of the intake manifold connection zone at one end to allow their coupling, and, on the other end, a tube shape compatible with the linkage element previously described. Two holes for screws were added to the throttle plate and holder to secure the throttle plate within the holder. Figure 4.3 presents the final result of the throttle plate set.

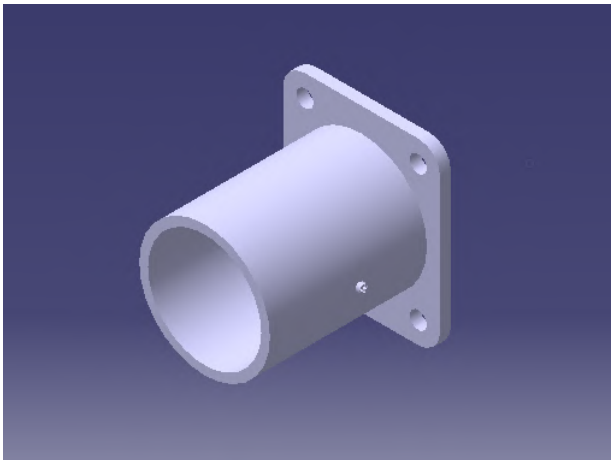

Figure 4.3: Throttle plate set isometric view.

4.2.4 Stepper motor support

Regarding the stepper motor, it had to be fixed to the test bench in order to transmit the required torque to the shaft connected to the camshaft. The easiest way found to fulfil the previous requirement was by designing a motor support. The support features an L shape with the required holes for the stepper motor to be fixed to the structure on the shortest side, and, on the other side, holes that allow the whole assembly to be fixed to the bench. This support configuration was adopted since it avoids any sideway or upward movement of the motor. Later on, after some preliminary tests, the lowest side began to bend inwards due to the high torque made by the stepper motor, reducing the initial 90º angle between both support surfaces. To counteract this tendency, two backings connecting both surfaces were added to the structure. The final configuration of the stepper motor support is shown in Figure 4.4.

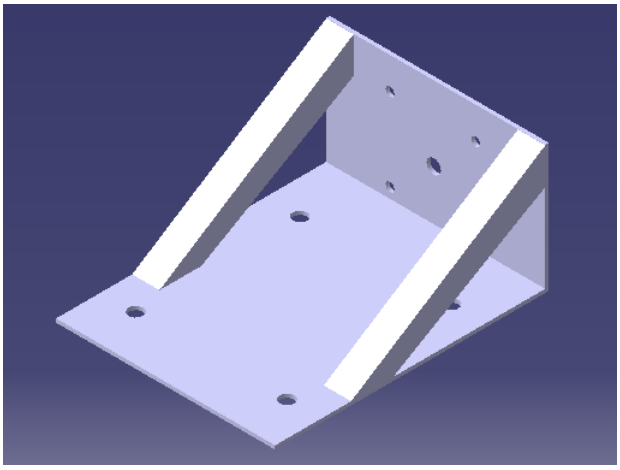

Figure 4.4: Stepper motor support isometric view.

4.2.5 Test bench

The design of the test bench involved constant changes and adjustments of several sections due to the available materials and the problems encountered throughout the assembly phase. The overall idea for the flow bench was to allow the engine head to be placed above the engine block so that the airflow can move from the inlet manifold into the cylinder in a downwards motion as in conventional engines. Therefore, the test bench was designed with two platforms spaced at a height equal to the height of the engine block. The lowest one, which is shorter, holds the engine block, whereas the highest secures the engine head and other components. Due to the need of allowing the airflow to be drawn into the engine cylinder and the suction machine to be connected to the bottom of the engine cylinder, two holes slightly bigger than the engine bore diameter were added to the sketch in both platforms. Both holes were aligned according to the first set of valves since it was decided to use only the first valve set of the engine head for the experiment.

The toothed belt-gear system required two small platforms fixed on the bench with specific heights and spacing in order to work properly. The stepper motor and the associated support are meant to be fixed on the lowest platform, while on the other platform, the shaft holders are screwed so that the shaft is properly aligned with the camshaft connecting zone. A system of tensioners was designed and added to the bench in order to keep the belt taut and reduce the possibility of belt slip. This system consists of a wall fixed on the edge of the top platform and a threaded rod which makes the connection between the wall and the stepper motor platform. One side of the threaded rod exceeds the wall and a nut placed on this side of the threaded rod sets the desired belt tension by pulling the stepper motor platform towards the wall.

At last, due to the heavyweight of the components and the vibrations produced by the stepper motor during the experimental tests, it was decided to join both smallest sides of the test bench and add two X's on the greatest sides in order to increase stability and rigidity of the whole set. The final result is shown in Figure 4.5.

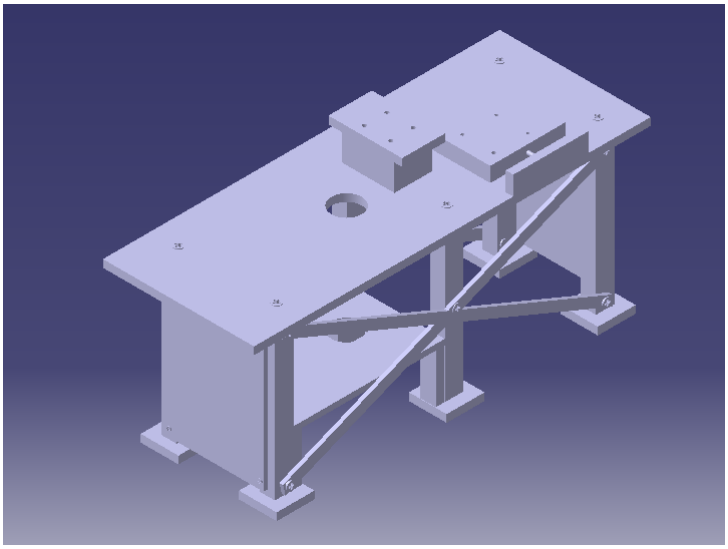

Figure 4.5: Test bench isometric view.

4.3 Manufacture

This stage starts when the designing phase of the required components is over. Here are presented the different manufacturing processes and materials adopted for the construction of the designed components, as well as the entire set of steps made to obtain the desired parts.

4.3.1 3D elements

The MAF-throttle holder linkage, shaft supports and the entire throttle plate set were manufactured on a 3D printing machine and are presented in Figure 4.6. Since these components, except the shaft supports, would only be used to control and direct the airflow throughout the induction system, it was decided to print them on Polylactic acid (PLA). At the time when it was to print the MAF-throttle holder linkage, PLA was not available, so, this element was made of Polyethylene terephthalate (PET) which is a thermoplastic polymer resin.

Figure 4.6: Manufactured 3D parts.

Even though the shaft supports had to endure some mechanical efforts, they were also made in PLA due to the good physical and mechanical properties of this material. Nevertheless, the areas subjected to greater stresses were reinforced by adding more thickness as a safeguard. The reason to use this manufacturing technique for the previous parts was due to its reasonably good precision and fast manufacturing.

In order to obtain the finished parts, the CAD file of each previous component is converted into STL format and the resultant file is then opened in Autodesk Fusion 360 software for the final adjustments such as setting tolerances. Afterwards, the modified STL file is loaded into Cura 3D printing software which will create the G-code that is sent to the 3D machine via Universal Serial Bus (USB).

4.3.2 Power supply

To build a power supply several components were required in order to run as expected. The components used in this one were the following:

- 350W pc power supply;
- Buck converter;
- two 100k Ohm potentiometers;
- digital Voltmeter ammeter;
- twelve female banana plug connectors;
- two switches;
- two knobs.

These previous elements were placed inside a built box with the respective cover. Both the box and the cover were made of wood with the dimensions shown in Figure 4.7.

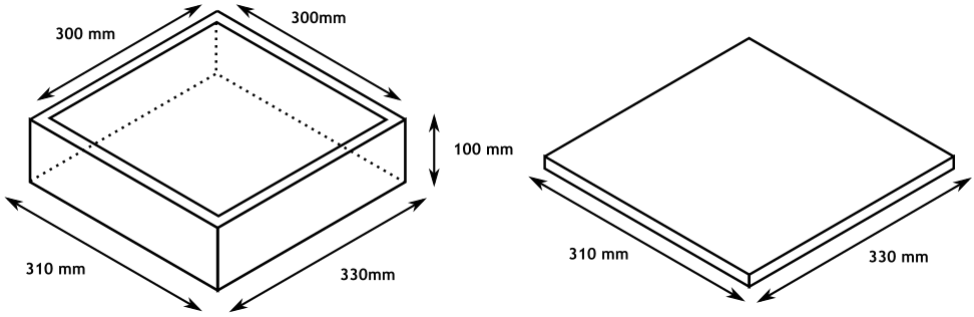

Figure 4.7: Power supply box and cover dimensions.

The wood boards utilized to build the box were remains from other projects, thus, the thickness and even the kind of wood were not the same. Since it was required to drill some holes for the outputs, display and switches, it was decided that the boards with lower thickness would be the front and the back of the power supply, whereas the thicker ones would be placed sideways. Thus, two thicker wood boards and two thin boards were linked together and to the bottom

wood board using wood glue and some small nails. The linkage between the box and the cover was done by means of a hinge which was screwed to one of the thickest wood pieces. In order to keep the lid closed, one magnet was installed on the cover and another magnet was placed on the top of the thicker wood board, in a way that the two magnets have opposite poles, creating an attraction force to keep the lid closed.

Regarding the required holes, a sketch highlighting the zones to be cut was drawn on the wood using a pencil and a ruler to ensure that the components to be inserted into the front of the power supply were properly spaced and could fit in the cut area. Using the sketch as a guide, the holes for the fixed and variable outputs were made with a 5 mm drill bit, the area for the display and the ON and OFF switch were cut using an electric saw and the hole for the enable switch was made using a 20 mm drill bit. Besides that, 10 mm holes for the potentiometers were added and, to allow a more efficient cooling, 20 mm holes on the sides were made and a rectangular section was cut away on the back.

Afterwards, the pc power supply was positioned in a way that the fan inside the pc power supply fitted the cut rectangular section and, once it was in place, the pc power supply was screwed to the bottom of the box. Subsequently, all components for the power supply were fitted into the respective holes in the wooden box and then, the internal connections were done. Figure D.1 in Appendix D presents the wiring scheme made for the variable output of the power supply. This wiring scheme was based on an existing scheme with some modifications implemented by the author that made the variable output section of the power supply to work properly. Regarding the fixed outputs, these were performed by connecting the remaining wires with the same colour to a red fixed output and an equivalent number of ground wires to the black fixed output associated with the previous one, taking into account the colour code shown in Table D.1 from Appendix D. All internal connections of the power supply are shown in Figure 4.8 (a) and were accomplished using a soldering iron, solder and soldering flux.

At last, a label which is presented in Figure 4.8 (b) was added to the front panel in order to notify the user about the voltage and current limit of each fixed output.

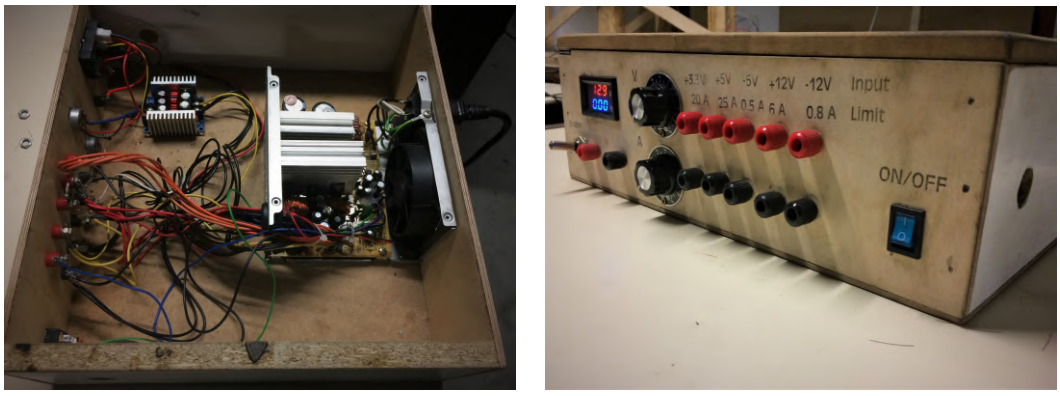

(a) Inside view (b) Outside view

Figure 4.8: Custom power supply.

The output limits were stamped on the box through a label printed on an A4 sheet with the letters rotated 180º with respect to X and acetone. Firstly, the sheet was positioned so that the

limits could be written above the respective output. Afterwards, the sheet was wetted with a reasonable amount of acetone and pressed against the wood panel with considerable force for 30 s using a rectangular piece of wood. Then, the sheet was removed and the engraving was printed on the wood. In order to make the letters more visible, this process had to be done several times as it didn't always work as expected.

4.3.3 Shaft

One steel shaft with 10 mm diameter was required to transmit the rotation from the stepper motor to the camshaft assembly. Thus, a 1 m shaft was acquired externally which was cut with 300 mm long. On one end of the shaft, a 1.25 pitch thread was made using a lathe to allow the shaft to be coupled with the camshaft set. Near to the other end of the shaft, a 4 mm hole was made perpendicular to the shaft in order to couple the gear from the toothed belt system to the shaft through a hexagon head M4 screw.

4.3.4 MAP calibration chamber

A calibration duct was created due to the need to calibrate the MAP sensors. The duct was made of steel, had 50 mm in length, and it was closed in both ends by tungsten inert gas (TIG) welding two cut steel circles with 35 mm diameter. On one end of the duct, a hole was opened in the center of the circular section using a 20 mm metal drill and a tire valve stem was installed in that hole to add or remove pressure to the chamber, as shown in Figure 4.9 (a). On the other end, a 12 mm hole, which corresponds to the diameter of the sensor, was made in the center of the other steel circle using a metal drill bit. This hole was to insert the MAP sensor but due to the shape and the gradual increased diameter of the sensor, it couldn't fit properly in the hole, so, a nut with a slightly larger inner diameter than the hole was welded over the hole in order to allow the sensor to fully enter into the pressure chamber (Figure 4.9 (b)).

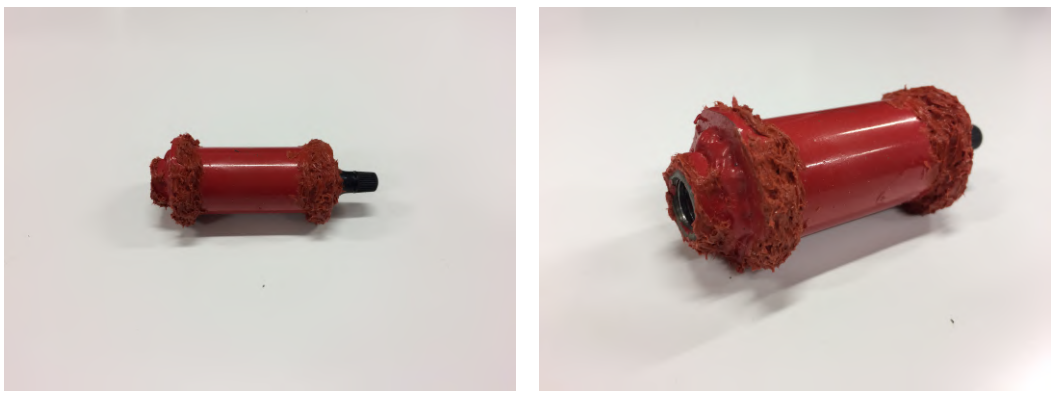

(a) Side view (b) Perspective view

Figure 4.9: Calibration chamber.

To confirm if there were any leaks, the chamber was dipped into a container having water. Before the chamber was dipped into the water, a small length bolt was tight to the nut to prevent the pressure inside the chamber from escaping. Several leaks were identified and closed with an adhesive sealant. Lastly, the chamber was red painted and the sharp edges of the welded circular sections were smoothed using an angle grinder.

4.3.5 Engine springs

The springs that came with the engine were stiff to avoid valve float which can cause a critical failure during engine operation. However, for the proposed tests, valve floating is not a major concern since it generally happens at high engine speeds which cannot be obtained during the experiment. This way, the original valve springs were replaced for a set of weaker springs which had to be modified in order to fit in the available space and attach to the valve. The weaker springs had approximately the same inner diameter as the original springs, roughly 27 mm, but were larger in length, therefore, the weaker springs were cut using a metal saw so that they had around the same length as the originals approximately 42 mm. Afterwards, the springs were secured in a bench vise and a hammer was used to make the cut end of the springs flatter as the original springs. After hammering several times, the springs were compressed in the bench vise and left in compression for a while in order to produce the same flatness at both ends. This procedure was repeated until both springs fitted into place. Figure 4.10 presents the original spring together with the used spring.

Figure 4.10: Original engine spring on the left along with the used spring.

4.3.6 Throttle plate angle cards

Instead of building and creating an angle scale, where the desired throttle angle could be set by moving the throttle plate until it matched with the angle in the scale, the author decided to go for an easier strategy. To make sure the throttle angle is the desired one, three small triangles of cardboard with the following angles 50, 60 and 70 were made and, in order to fit inside the throttle plate holder, one end of each triangle was cut with scissors. Knowing that the internal sum of the angles of a triangle is 180º, the triangle of 60º can also be used to mark 30º and so on. Therefore, it only takes three triangles to obtain the required throttle plate angles. Regarding the 90º throttle plate position, a ruler placed over the flat surface of the throttle plate was used to ensure the WOT position.

4.3.7 Stepper motor support

The stepper motor support was made using a 2 mm thick sheet metal, in which, a rectangle with 220 X 120 mm was cut using a grinding wheel. Afterwards, the cut rectangle was secured in a bench vise and was bent so that both surfaces were roughly perpendicular to each other. After achieving the L shape, four 4 mm holes and one 8 mm hole were opened on the vertical

surface of the support using a metal drill in order to allow the stepper motor to be fixed to the structure. On the horizontal surface of the support, four 8 mm holes were made to provide a stable and reliable attachment to the platform. Then, two metal profiles were cut with a 45º angle using a metallic saw and a paper triangle with 45º as a guide. The resultant profiles measured 45 mm long and were welded to the support using arc welding.

4.3.8 Tensioning system

A tensioning system, presented in Figure 4.11, was built to ensure that the belt was always taut, preventing belt slip during the stepper motor operation. For the construction of this system, it was used a 12 mm diameter threaded rod, an L shaped steel bar, a 12 mm inner diameter nut, a 2 mm thick sheet metal with 150 X 120 mm and a rectangular wooden bar. Firstly, the L shaped steel bar had to be cut to measure 120 mm, and then, two 4 mm holes were opened near each end of the L shaped bar using a metal drill in order to allow it to be fixed to the wood platform, in which, the stepper motor is fixed.

Figure 4.11: Tensioning system.

Afterwards, the threaded rod was welded to the backing of the stepper motor support using arc welding. Subsequently, the rectangular wooden bar was cut into the desired measures, 200 X 170 mm, and a 12.5 mm hole was made on the center and at the same height as the threaded rod. After the hole was made, two 4 mm holes were opened in the test bench top platform and in the wooden bar so that the wooden bar is fixed to the edge of the test bench top platform with two M4 screws. Afterwards, the threaded rod was inserted into the center hole of the wooden bar, a 12.5 mm hole was created on the center of the 2 mm thick sheet metal and the sheet metal was then placed between the nut and the wood surface in order to spread the force that the nut makes over a larger area. Lastly, the nut was inserted into the threaded rod and the belt tension was adjusted by tightening the nut.

4.3.9 Test bench

It was decided to build a wooden test bench since it only needs to provide a stable base for the components and if some major adjustments were required, it would be easier to implement them on a wooden bench. Thus, six wood squares with 100 X 100 mm and six wood bars measuring 410 mm long were cut using an electric saw and a wood saw in order to make the supports

of the test bench. This length was chosen based on the height of the engine block, which was 240 mm, and the height required to install a plastic hose under the lower platform which will be used to connect the suction machine to the cylinder.

Afterwards, two wood boards with 1050 X 400 mm and 390 X 320 mm were cut using the electric saw to make the top and bottom platforms, respectively. On both platforms, an 80 mm circle was cut to connect the engine head with the engine cylinder and to allow the plastic hose to be connected to the bottom of the engine cylinder. Besides that 80 mm circle, four 10 mm holes were opened on the top platform of the bench around the 80 mm circle in order to allow the attachment of the engine head with the block. To make sure these four holes were aligned to the engine block, before drilling the four holes, a sheet of paper was placed over the surface of the block and the various holes of interest in the block were marked. Furthermore, a reference was established and also marked. The engine block was then positioned on the lower platform so that the cylinder hole was aligned with the upper platform hole. After that, the guide sheet was placed over the upper platform cylinder hole, the reference was checked and the holes to be drilled were marked.

Subsequently, it was required to fix the engine block into the lower platform to ensure that the reference never changes. To perform this, two 8 mm holes were drilled into the lower platform after the correct engine block position which allows the holes to be aligned was found. Still on the top platform, six 5 mm holes were drilled, one in each corner and the other two 100 mm away from the board center in order to allow more space on one side for the engine block to be placed and fix the wooden legs to the top platform. Subsequently, four 130 mm long and 30 mm wide wooden bars were cut from a larger bar with the electric saw and a 4 mm hole was made perpendicular to each bar in order to support the lower platform. After that, four 4 mm holes were made on the corners of the lower platform to attach it to the four 130 mm long bars.

Afterwards, it was necessary to know the required height that the platform having the shaft supports would need to have so that the shaft was aligned with the camshaft connecting point. Thus, a test platform was made with higher height than the required and, each time it was tried, its height was lowered until the shaft was lined to the camshaft. It was determined that the required height would be 97 mm, therefore, five wood boards with 150 X 100 mm were cut and glued on top of each other, reaching the desired height. On the bottom board of the stack were drilled three 5 mm holes to link the platform to the top board of the bench. To finish this part, a bigger wood board with 195 X 115 mm was glued on top of the five stack and four 10 mm holes were opened on this last board to allow the shaft holders to be fixed to the platform.

Regarding the stepper motor platform, this was made of two wood boards glued together having 200 X 150 mm as dimensions. Four 8 mm holes were opened over the entire thickness of the platform matching the holes of the stepper motor support to allow the stepper motor and respective structure to be fixed to the platform. A rail system was made on the upper platform of the test bench in order to allow the stepper motor platform to move towards the tensioning system wooden bar so that belt tension is improved. At last, in order to add more stability and rigidity to the test bench, two wood boards with 380 X 260 mm were drilled into the four corners to be fixed to the smaller sides of the test bench and two wood X's were drilled and fixed into the greater sides of the test bench. Besides that, another board with 420 X 260 mm was fixed into the test bench square bases through six 5 mm holes.

The manufacturing processes used to obtain the final components were the following ones:

- Arc welding;
- TIG welding;
- Sawing;
- 3D printing;
- Drilling;
- Grinding;

4.4 Assembly

This subchapter describes how the different components are assembled and also points out the problems encountered in this phase and the adopted solutions to overcome these obstacles.

4.4.1 Components assembly

Engine - For the experimental tests it was only required the engine head, one cylinder from the engine block and the intake system. The available engine was found to be fully assembled. Thus, the engine had to be disassembled so that the engine head and block were freed from other parts. This disassembly process took a long time because the tools available in the department were not suitable for the bolts and nuts that fix the whole engine. Since the type of bolts and nuts were very specific, it was required a proper socket and ratchet set which was luckily found in another department.

Firstly, the engine head was removed by freeing the only M10 bolt that was fixing the head to the engine block using a ratchet and the compatible socket. Subsequently, the oil filter was removed by loosening three M14 bolts and the carter was carefully extracted from the engine since it still had some oil. Afterwards, in order to free the pistons, all bearings securing the pistons to the crankshaft were removed by releasing the eight bolts using the ratchet and an 11 mm socket. After that was done, the pistons were extracted by tapping them towards the engine head side with a hammer and a steel pipe. To remove the crankshaft it was required to firstly, take the flywheel off, which was fixed with four M14 bolts, and then remove the main bearings using a ratchet and a 13 mm socket.

The engine block was cut with a mechanical saw in a way that one cylinder and the associated holes, which fix the engine head to the block, could be used in the experiment. The reason to cut the block was due to its high weight which would force some modifications in terms of robustness to the already designed test bench.

Test bench - The six square bases were linked together with the six wooden bars through six M5 screws using an electric screwdriver. Afterwards, the top platform was fixed to each wooden bar by screwing six M5 screws into the drilled holes on the wood board and placing the bar underneath the board. After that, the four small wood bars were attached to the middle vertical

bars and to the vertical bars farthest from the middle bars so that the lower platform can be placed above the small bars and screwed using four M4 screws, as shown in Figure 4.12.

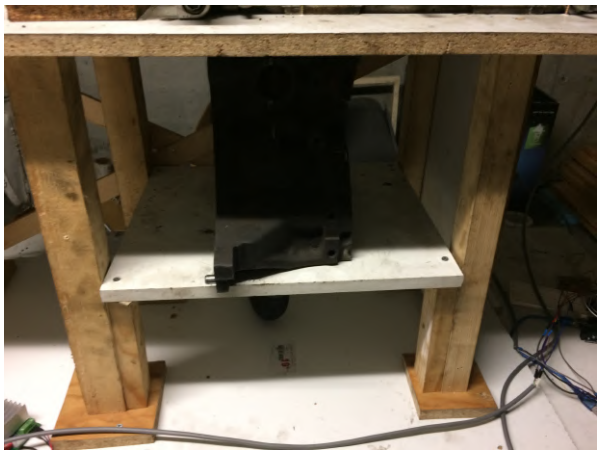

Figure 4.12: Test bench bottom platform.

The shaft platform was attached to the top board of the bench by means of three M5 screws and a screwdriver at a specific distance (35 mm) from the engine head in order to make possible the shaft-camshaft connection and allow the gear placement on the other end of the shaft. The stepper motor platform, in its turn, was linked to the top board of the bench through four M8 bolts and the respective nuts and washers. This linkage was done by placing the platform over the rail system and inserting firstly the washers and then the four bolts from bottom to top. After that, the desired position was set by moving the platform inside the rail system and, once it was defined, the nuts were added and tighten using a 13 mm wrench, locking the platform in place. Regarding the structures added to the sides and to the bottom of the bench, these were screwed using 4 mm and 5 mm screws and an electric screwdriver.

Engine parts and bench - The engine block was the first engine part to be placed on the test bench. Its attachment was made through two M8 bolts placed on each side of the block and, to minimize the space between the engine block and the upper platform, wooden shims were placed on each small bar that holds the lower platform. The engine head, in its turn, was placed over the upper platform and the cylinder hole alignment was made by aligning the four holes around the cylinder hole. After the holes were aligned, the two camshafts had to be removed using a 10 mm wrench, to insert and tight the only M10 bolt that was securing the engine head and block together when the engine was disassembled. For the remaining holes were inserted three steel shafts in order to ensure the alignment of both engine parts. Afterwards, several M4 screws were screwed around the engine head to prevent engine head movement when the engine block had to be removed.

Tensioning system and bench - The wooden bar that belongs to this system was attached to the top board of the bench by means of two M4 screws and the L shaped steel bar was fixed to the stepper motor platform using two M4 screws and the respective screwdriver.

Engine head and intake manifold - Before connecting the inlet manifold to the head, it was required to clean the inside of the manifold due to the large accumulated dirt which could influ-

ence the results. For the cleaning process, a brake cleaner and some paper towels were used. After that, two metal sheets with 0.5 mm thickness were cut in order to block three intake runners since for the experiment only one inlet runner was necessary. Both sheets were placed and fixed over the unwanted intake runners using an adhesive sealant. The intake manifold had some holes for sensors which were close, except one, using again an adhesive sealant. This open hole will be used to place the thermocouple inside the manifold later on.

Afterwards, the cover was fitted over the open section of the inlet manifold and both parts were tight using two M6 nuts and three M6 hexagon bolts. Once the inlet manifold was fully mounted, it was fixed to the engine head side where the intake valves were through two M8 nuts and three M8 bolts tighten using a 13 mm wrench.

Intake manifold and MAF sensor - Firstly, the throttle plate was fitted inside the holder by means of two M3 screws which were slightly tight so that the throttle angle could be set. Subsequently, the throttle plate holder was attached with the entrance of the intake manifold through the alignment of the two manifold bolt stems and by means of two M8 bolts. The linkage between the MAF sensor and the throttle holder was made through the 3D connecting element, which was fitted in both MAF and throttle holder, as shown in Figure 4.13.

Figure 4.13: Inlet manifold-MAF sensor assembly.

Shafts and respective holders - Before fixing the shaft holders to the corresponding platform, a 30 mm bearing was inserted into each holder to minimize friction between the two parts. Afterwards, both shaft holders were attached to the matching platform through four M8 screws and the respective screwdriver. Subsequently, the shaft was introduced between the holders so that the threaded end of the shaft faces the engine head.

Stepper motor - The stepper motor was inserted and attached to the respective support by means of four M4 screws and four M4 nuts. Afterwards, the support was placed over the moving platform so that the holes on the support match the holes on the platform. After the alignment was made, the four M8 bolts, that connect the platform to the upper board of the bench, were tight until the bolt stem passed through the stepper motor support. At last, when the desired position of the platform was set, the four M8 nuts were tight using a 13 mm wrench in order to prevent the whole assembly to move when the stepper motor was operating. Due to the back-

ings on the support, the front bolts had to be cut in order that the front nuts could be inserted from above.

Toothed belt-pulley-gear system - To successfully transmit the stepper motor torque into the camshaft set, a 20 mm diameter pulley was fixed to the stepper motor shaft and a 48 teeth gear was connected to the available shaft. Firstly, an 8 mm hole was opened in the center of the small pulley using the lathe and an 8 mm metal drill bit, in order to allow the small pulley to be placed into stepper motor shaft. Afterwards, a 4 mm hole was made perpendicular to the previous hole and a 4 mm thread tap was used to create a thread inside the hole.

Subsequently, a mark was made on the stepper motor shaft to serve as a guide for the 4 mm shallow hole which had to be drilled into the stepper motor shaft in order to prevent the pulley from slipping on the shaft. This hole on the motor shaft was made using a 4 mm drill bit which was secured in a column drilling machine, and, after it was done, the pulley was inserted into the motor shaft. An M4 screw was screwed into the 4 mm hole on the small pulley which required to be aligned to properly secure the pulley to the motor shaft. The head of the M4 screw had to be trimmed using a grinding wheel since it wouldn't let the screw enter into the hole. After the screw head was reduced, the M4 screw was tight until the screw stem enters inside the shallow hole of the motor shaft.

Regarding the gear, a 10 mm hole was opened in the center of the gear using the same tools as in the small pulley, except the 8 mm drill bit which was changed to a 10 mm one. After the hole was done, the gear was fixed into the shaft through brazing.However, after some preliminary tests gear slip started to occur whenever the cams pressed the intake valves.As a solution, it was adopted the same technique used to fix the small pulley into the motor shaft. This way, a 4 mm hole was opened into the gear perpendicular to the shaft and a thread was made in the hole using a 4 mm thread tap. Afterwards, a 4 mm shallow hole was done into the shaft and then the gear was fixed to the shaft by tightening the M4 screw until it reaches the shallow hole. Lastly, a 180 mm length belt was placed between the pulley and the gear, see Figure 4.14, allowing torque transmission to the inlet valves.

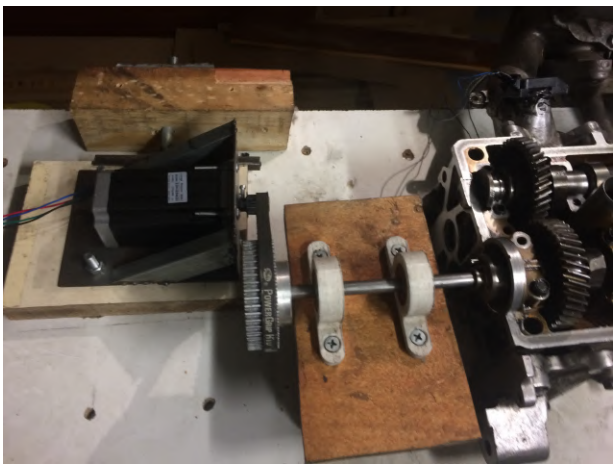

Figure 4.14: Toothed belt-pulley-gear system.

Engine valves - For the experimental tests only the first set of valves was required, thus, all the

valves, springs and tappets from the unwanted cylinders were removed, reducing the required torque to rotate the camshafts. The valve assembly is constituted by several parts, as shown in Figure 4.15. In order to extract the valves, the tappets were firstly removed by hand followed by the retainers and locks that keep the spring compressed and the valve in place. The retainers and locks were removed by placing a steel bar over the retainer and hammering it with enough strength for the locks to pop up. After that, the spring, oil seals and the valve were extracted and saved in a cardboard box. This procedure was repeated for the remaining valves of the unneeded cylinders.

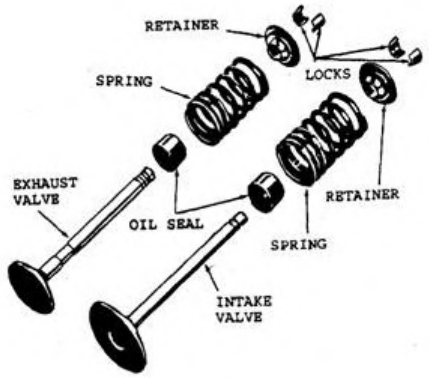

Figure 4.15: Valve components assembly [53].

It was decided to not extract the exhaust valves of the cylinder that will be used for the experiment because the cylinder needs to be sealed during the tests. However, it was also required that the exhaust valves do not open since only the intake stroke is studied in this work. To achieve this requirement, the exhaust cams matching with the first set of exhaust valves were cut using a grinding machine to ensure that, when the camshaft rotates the exhaust valves remain closed. Afterwards, the original springs of both inlet valves of the cylinder used during the tests were removed to be replaced by the modified weaker springs. The inlet valves were really dark and dirty due to the combustion process, so, both inlets were cleaned using two scouring pads and a drilling machine. The stem of the valve was grabbed using the drilling machine chuck, the drilling machine was turned on and the valve was rub with the scouring pad until it was clean.

Subsequently, the intake valve was placed in the respective hole followed by the oil seal, the modified spring and the retainer. In order to lock the valve and spring in place, it was required a specific tool which was not available. Thus, a simple tool, presented in Figure 4.16, was created for this purpose. This tool was a tube made of Polyvinyl chloride (PVC) with a hole opened on one end which allows the placement of the locks while applying pressure on the retainer.

Before placing the locks, a wood piece was placed on the valve head to prevent the valve stem from going down while force was being made. Afterwards, the created tool was placed over the retainer with the hole in contact with the retainer and faced towards the author. To assist in applying force against the spring a clamp was used. The clamp presses the tool which presses the spring until the lock grooves are seen from the hole in the created tool. In the meantime, the two locks were placed into the grooves, one at a time, using a magnetized screwdriver to hold the locks.

Figure 4.16: Custom made tool.

The same procedure was done for the other inlet valve, the two tappets were placed and both camshafts were mounted into the engine head.

Suction machine and cylinder - The cylinder was closed at the bottom with a 78.5 mm diameter wood circle which was cut using an electric saw and a 20 mm drill bit. Before inserting the wood circle inside the cylinder, it was required to open a 40 mm hole at the center of the circle in order to connect a plastic hose to provide the linkage between the suction machine and the cylinder. Afterwards, the circle was pushed from the top of the cylinder to the bottom and adhesive sealant was placed over the junctions to ensure no air leaks. Subsequently, a plastic hose was inserted into the center hole of the wood circle and the other side of the hose was connected to another plastic hose which was linked to the suction machine.

Figure 4.17 shows the final placement of every component after the assembly process is finished.

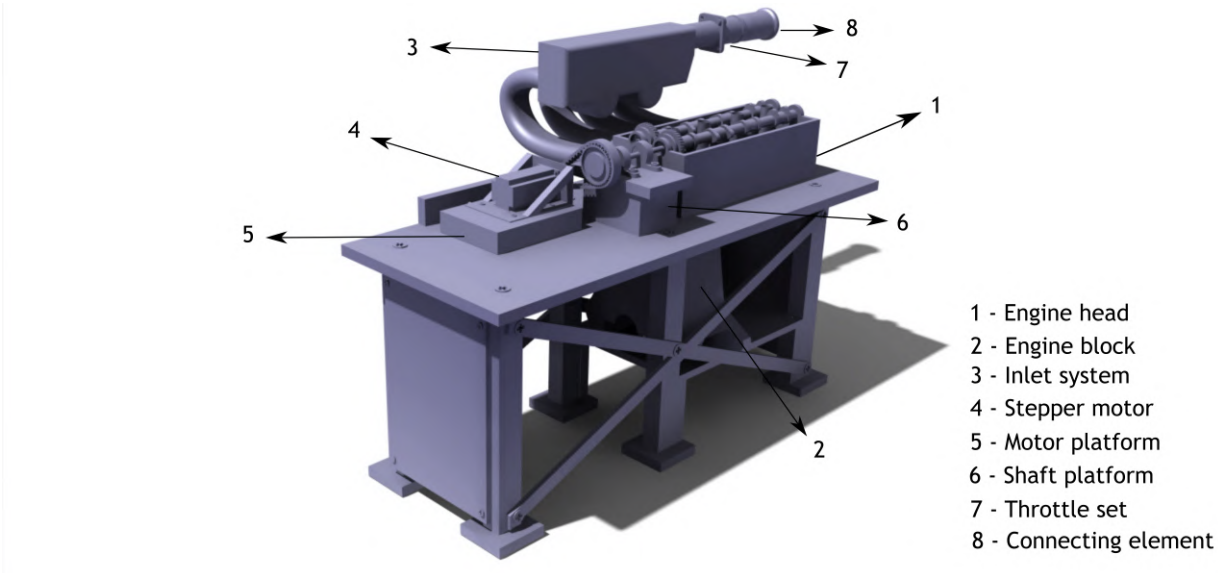

Figure 4.17: Finished assembly.

Chapter 5

Experimental tests and Results

The present chapter makes a summarized description of the experiment by specifying the measuring conditions for each variable parameter, intake strategy and flow condition. Moreover, it reveals the electrical connections made for the sensors and the stepper motor to work, the major problems found during the final steps and the experimental procedures for both tests conditions. At last, the results obtained are shown and the uncertainties associated with the experimental values are determined.

5.1 Characterization of the experiment

This experimental work consists in the analysis of the fluid dynamic efficiency of a multi-valve spark-ignition engine throughout the induction phase and in the evaluation of the effect of adding a throttle plate on the head permeability. For this purpose, two intake valve strategies are considered, tested and analysed in both steady and unsteady conditions in order to study, in detail, the overall efficiency of the port-valve assembly for the defined configurations.

The first valve lift setup is typical of conventional multi-valve engines, where the intake valves open and close at the same time, whereas the second one is an alternative valve strategy which has been less studied and may play an important role on the engine permeability and consequently on engine performance [1]. The valve deactivation option simply consists in disabling one of the inlet valves. As a result, the available flow area of the valve system will be reduced, in comparison to the standard setup, but the valve interference phenomena, which strongly affects engine breathability, will be eliminated [45].

To measure the fluid dynamic efficiency of the engine head at steady conditions, the experiment is carried out at a steady/unsteady flow rig, where air is sucked into the cylinder by means of a suction device to simulate the piston action and dimensionless discharge and flow coefficients are determined for a set of fixed valve lifts. Moreover, in order to assess the effect of a throttle plate on the engine permeability, the parameters of interest are calculated at several throttle plate positions. During each measurement, the valve lift, throttle angle and suction pressure are fixed and values of air mass flow, intake temperature, intake pressure and cylinder pressure are registered.

It was decided to use dimensionless valve lifts (L_v/D) in order to remove the size effects and limitations imposed by units of measurement. The range of values tested for the dimensionless valve lift, throttle plate angle and pressure drop in each intake strategy considered are presented in Table 5.1. A configuration without a throttle plate was also evaluated at steady conditions to compare with a throttle plate setup.

For the measurement of unsteady discharge and flow coefficients, the same flow rig is used since

Table 5.1: Measuring conditions for the investigated intake strategies during static conditions.

Configuration	Standard	Valve deactivation
Dimensionless valve 1 lift	0.016 to 0.27	
Dimensionless valve 2 lift	0.016 to 0.27	-
Throttle plate angle [º]	30, 50 , 70, 90	
Pressure drop [kPa]	13	

it allows steady and unsteady measurements. This time the camshaft is driven to a certain speed and the inlet valve lift changes continuously, carrying out the profile presented in Figure 5.1. According to the defined reference, the IVO and IVC times were at 135º and 255º, respectively. The effect of the throttle plate position and the camshaft speed on the dynamic discharge and flow coefficients are analysed in order to compare with the steady coefficients.

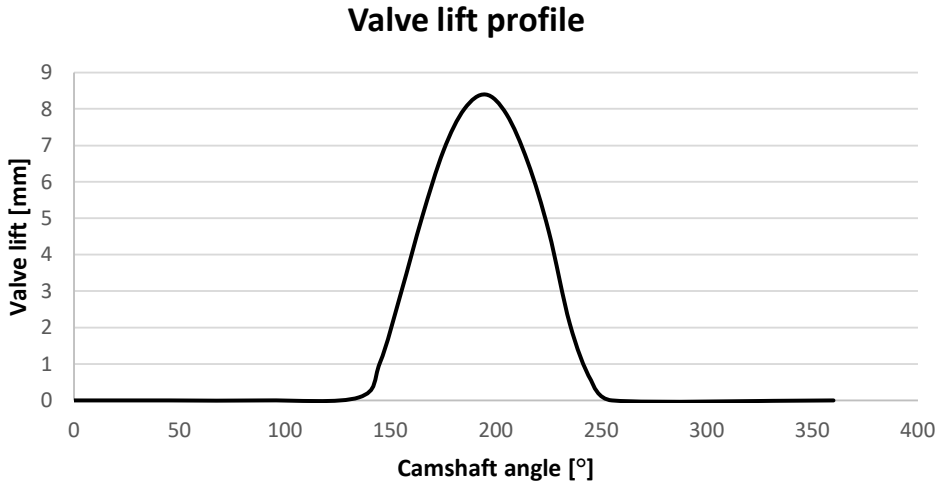

Figure 5.1: Intake valve lift profile.

Likewise under static conditions, the temperature, pressure and air mass flow rate are registered during each test and the configuration without throttle is tested. Each measurement is made when the camshaft speed, suction pressure and throttle plate angle are constant. The range of values chosen for the three previous parameters is indicated in Table 5.2 for the two different intake valve strategies.

Table 5.2: Measuring conditions for the analysed inlet setups in dynamic tests.

Configuration	Standard	Valve deactivation
Camshaft rotation [rpm]	5, 10, 15, 20	
Throttle plate angle [º]	30, 50, 70, 90	
Pressure drop [kPa]	13	

5.2 Sensors and stepper motor final steps

5.2.1 MAF sensor

After knowing the MAF sensor features, the corresponding characteristic curve was selected through the sensor's datasheet and, in order to discover the equation of the characteristic curve, the associated voltage and air mass flow values were sent to Microsoft Excel where a tendency curve was implemented, resulting in an equation for that curve (see Figure A.1 in Appendix A). The MAF sensor used measures airflow mass rates until 480 kg/h and has five connecting pins. Only four of the five connecting pins were used since the pin 1 measures the temperature. The connections among the sensor, power supply and the Arduino Uno board are shown in Figure 5.2 and were established using a solder iron and solder.

Firstly, two male banana connectors are fixed to one end of the wires that will be connected to the ground and supply voltage pins of the sensor. Afterwards, the following connections were made accordingly with the sensor's pinout: Pin 2 - red variable output; Pin 3 - black variable output and GND on Arduino; Pin 4 - +5V Arduino; Pin 5 - A3 Arduino pin. It was used heat shrink tube to isolate the connections made in the sensor and prevent short circuits, and an extension was made since the sensor was placed far from the Arduino board and the power supply.

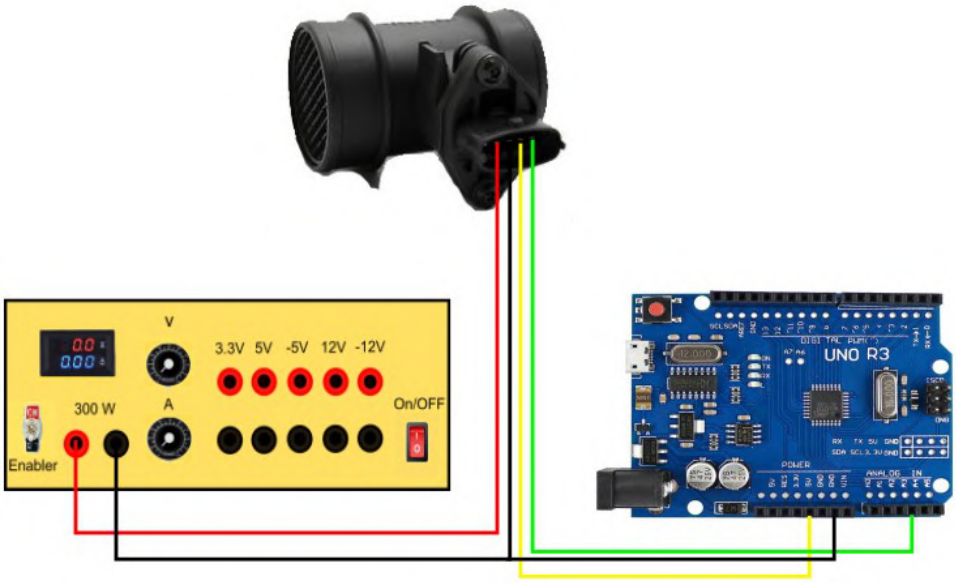

Figure 5.2: MAF sensor connections created using Inkscape.

After that, an Arduino code ("Sensor readings"), presented in Appendix F.1 and created by the author using C programming language, is compiled and uploaded to the Arduino board. This code reads the sensor value, converts that value into voltage through the calibration equation of the sensor to determine the actual air mass flowing through the sensor and shows the measured air mass flow in the serial monitor. Regarding the MAF sensor positioning in the experiment, the sensor had to be placed before the inlet system and the throttle body due to reasons that will be indicated in the Problems found section.

5.2.2 MAP sensors

Each MAP sensor has four outputs but only three were used since one of the pins was for temperature measurement. The established connections are presented in Table 5.3. Similarly to the MAF sensor connections, heat shrinking tube was used and an extension was made for each MAP sensor.

Table 5.3: Arduino Uno and MAP sensors connections.

Intake MAP sensor	Arduino Uno	Cylinder MAP sensor
Pin 1	A1	-
-	A2	Pin 1
Pin 2	+5V	Pin 2
Pin 4	Ground	Pin 4

Afterwards, both sensors were calibrated using the MAP calibration chamber and a vacuum pump. Firstly, the MAP sensor was inserted into the calibration chamber and the vacuum pump was connected to the tire valve stem.Then, the Arduino board was connected to the computer via USB, the “Sensor readings” code was uploaded to the Arduino board and the voltage values were displayed in the serial monitor. The MAP code during the calibration test only provided the voltage correspondent to the sensor value since the true pressure values were not known. The vacuum pump had a pressure scale in inches of Hg and, with that scale pressure, values were collected as well as the associated voltages using Arduino.

During the calibration, three sets of voltage measurements were made and, in each measurement, the chamber pressure was reduced 5 inches of Hg until 20 inches of Hg, resulting in 5 measuring points per set. An average of the voltage measured in each pressure was made which was then sent, together with the pressure values, to Excel where the calibration line and equation of each MAP sensor, presented in Figures B.1 and B.2 of Appendix B, were obtained. Afterwards, these calibration equations were implemented in the “Sensor readings” code to convert the sensor’s voltage to pressure and thus allow pressure measurements.

The pressure drop across the inlet valves is crucial to determinate the coefficients of interest, thus, one MAP sensor was placed into the injector’s hole, which was right before the intake valve, and the other one was positioned inside the cylinder, as shown in Figures 5.3 (a) and (b). In order to fix the inlet MAP sensor to the injector’s hole, it was required to enlarge the existing hole by using a drilling machine with a 12.5 mm drill bit and apply some adhesive sealant to prevent air leaks and assist in sensor’s fixing.

On the other hand, for the placement of the cylinder MAP sensor, an outside cylinder section had to be removed using a grinding machine to allow the sensor to be placed at the desired location. Afterwards, the 12.5 mm hole required for the sensor was made perpendicular to the cylinder and as close as possible to the valves, taking into account the size of the sensor and the valve action. After the hole was done, the MAP sensor was fitted into the tight hole.

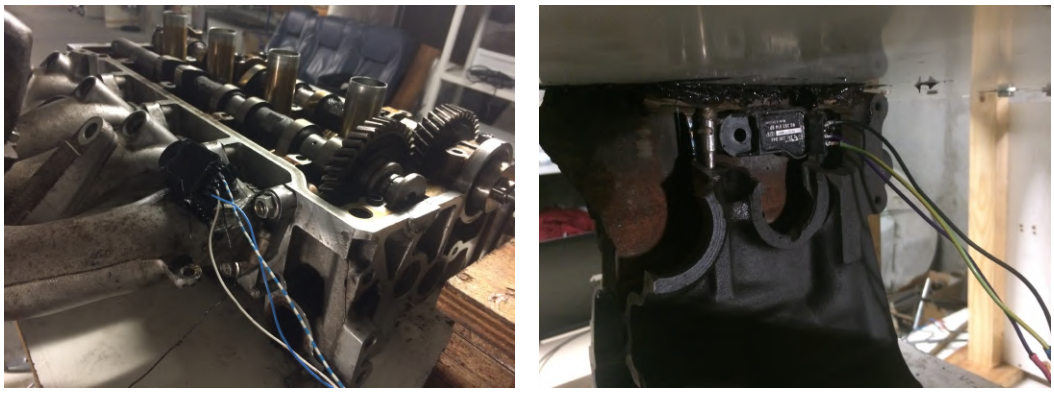

(a) Inlet MAP sensor (b) Cylinder MAP sensor

Figure 5.3: MAP sensors position.

5.2.3 Thermocouple

The MAX6675 thermocouple was linked to the associated module by connecting the red connector to the positive input of the module and the blue connector to the negative one. Afterwards, the thermocouple module was connected to the Arduino Uno board, resulting in the connections: SO pin - D11; CS pin - D10; SCK pin - D6. To perform these connections it was used a soldering iron, heat shrinking tube and an extension was made. Subsequently, the thermocouple code was created and added to the ”Sensors readings” code. Then, the Arduino board was connected to the computer where the ”Sensors readings” code was compiled into the Arduino software and the temperature readings were displayed. Lastly, the thermocouple was placed inside the intake manifold through the single hole which was not covered and adhesive sealant was used to prevent air leaks and secure the thermocouple, as shown in Figure 5.4.

Figure 5.4: Thermocouple location.

5.2.4 Stepper motor

The Nema 23 stepper motor was used together with the TB6600 v1.2 stepper motor driver which controls the stepper motor. The four coloured wires coming from the Nema 23 (red, blue, green and black) represent each set of coils and were linked to four of the six driver inputs.

The two other inputs of the Tb6600 v1.2 driver were connected to the 12V fixed output of the custom power supply using two wires each one with a male banana plug connector at one end. Afterwards, three of the four outputs of the driver were connected to the second Arduino Uno board since the enable pin was not necessary for the stepper motor to operate. The established connections between the outputs of the driver and the Arduino board were the following as presented in Figure 5.5: 5V - 5V; CLK - D5 pin; CW - D9.

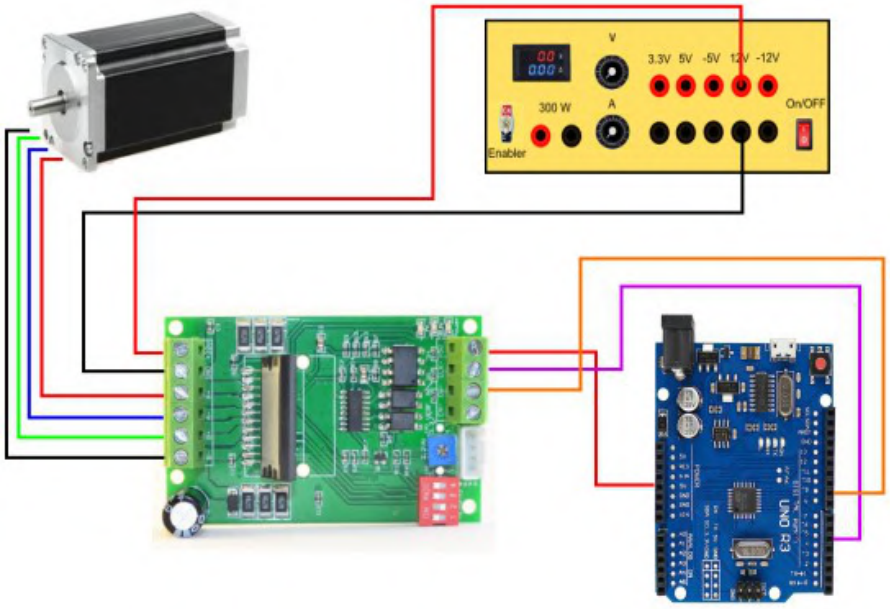

Figure 5.5: Stepper motor connections created in Inkscape.

Subsequently, two more Arduino codes were created, one to control the stepper motor during the static tests and the other to control the motor in dynamic tests. These codes were based on several parts of existing ones which were modified to the experiment requirements. The ”Nema 23 static conditions” code uses the Accel stepper library to set the speed and acceleration of the motor. The acceleration, speed, number of steps and direction are defined in a function which is used throughout the code, resulting in the desired motion by the stepper motor for this condition. On the other hand, the ”Nema 23 dynamic condition” code uses the Stepper library which allows the user to define the motor speed and insert a number of steps, leading to a constant speed motion by the motor which is important for the unsteady tests. Both Arduino codes can be found in Appendix F section F.2 and F.3, respectively.

5.3 Low-pass filter

During the experiment, it was required to implement and design a filter for the airflow data since the MAF sensor had a considerable amount of sensor noise. It was decided to use a low-pass filter due to its ability to smooth sets of data and its adjustable features which allow the filter to adapt to a specific signal. A filter of this nature allows low-frequency signals below the cutoff frequency to pass and attenuates signals with a higher frequency than the cutoff frequency. Thus, high-frequency noise is largely eliminated, enabling more accurate analysis of

the data. The low-pass filter was added to the "Sensor readings" code through Equation 5.1.

$$y_f(t_k) = \frac{1}{2\alpha + \beta_f T}\left[(2\alpha - \beta_f T)\, y_f\,(t_{k-1}) + KTy_s\,(t_k) + KTy_s\,(t_{k-1})\right] \quad (5.1)$$

where

$y_f(t_k)$ and $y_s(t_k)$ are the actual filter and signal values, respectively.
α is the damping coefficient.
β_f is a filter constant.
T is the response time of the filter.
$y_f(t_{k-1})$ and $y_s(t_{k-1})$ are the previous filter and signal values, respectively.
K is the filter gain.

Several performance tests were made to the filter in order to improve the filtering quality of the signal sent by the MAF sensor. During this designing stage, only the response time and the damping coefficient were changed since these two parameters had the greatest impact on the filter action. After the tests were finished, it was concluded that a damping coefficient of 3 and a response time of 1 provided the required filter action for the airflow data during the static tests. Figure 5.6 illustrates the filter behaviour with the previously defined design parameters in the static tests.

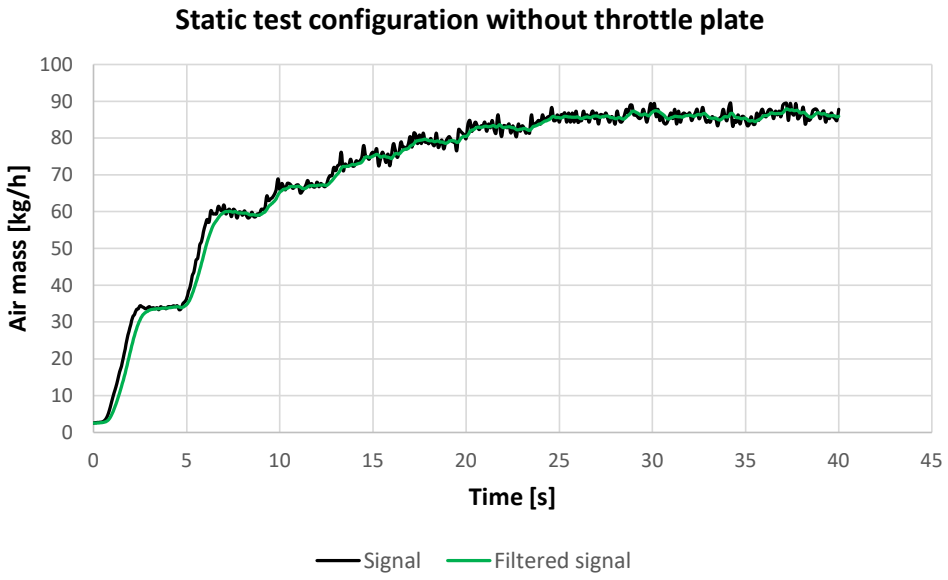

Figure 5.6: Filter acting in a static test.

In order for the dynamic results to be more accurate, the filter would have to be designed for each individual rpm. However, this important aspect was forgotten during unsteady tests. Therefore, it was decided to use the filter only for the static test and rely on the MAF sensor values for the dynamic results.

5.4 Problems found

Here some of the major difficulties encountered during the final steps will be highlighted as well as the solutions adopted to overcome these barriers.

5.4.1 Stepper motor calibration for the experimental tests

The static tests required that the stepper motor opened the valves until several desired valve lifts and maintained the valves at that lift for a short period of time. It is important to highlight that, when this calibration step started, the stepper motor had a different positioning, the tensioning system was different and the medium pulley, as well as the smaller toothed belt were installed instead of the gear and the longer belt (see Figure 5.7). This was the initial experiment setup which had to be changed due to the lack of torque and precision demonstrated by the stepper motor. The medium pulley, which was fixed to the shaft, doubled the torque imposed by the stepper motor which, in its turn, allowed the inlet valves to open and close. The motor had enough torque to open the valves with that configuration, but it didn't have the required torque to allow the same repeatability throughout the tests. As it will be explained ahead, this downside of not achieving the same repeatability, lead to several changes in the experimental configuration.

Figure 5.7: Initial experimental apparatus configuration.

To perform the calibration of the stepper motor, the engine block and the lower platform, that held the block, had to be removed from the test bench. Afterwards, a dial indicator with support was positioned below the inlet valves and the measuring tip of this device was placed in contact with one of the inlet valves head. Subsequently, the dial indicator was set to zero and the first set of cams were moved to a reference point in order to set the same basis for all studied valve lifts. The reference was defined as being the 90º position of the first set of cams in relation to the engine head. It was required to define an uncertainty interval of $\pm$ 5º for the reference since it was really difficult to ensure the 90º angle of the cams. A protractor was used during the calibration and the static tests to ensure that the reference was within the defined angle range.

Then, an early version of the "Nema 23 static conditions" code was upload to the Arduino board

and several Arduino libraries to control stepper motors were tried. Major difficulties were encountered during the Arduino code development since different Arduino libraries produced different movements by the motor. The motor running with the stepper library uploaded would lose some steps when opening the inlet valves, but as the valves were closing, the lost steps were gained and the motor would return to the reference position as if it never had lost any steps. This motor behaviour was due to its lack of torque and the stepper library, which maintains the motor speed constant during its movement.

The solution found for these two barriers was to use the available gear, which would quadruple the motor torque, and to find out a library that allowed to define the motor acceleration and speed during its movement. Due to the need of more torque, the initial experiment setup had to be modified since the gear was too big to fit in the available space with the motor below and the longer belt was required which couldn't fit in that setup. This way, the final experiment configuration appears, ensuring the increased torque. Regarding the Arduino code, the Accelstepper library, which fulfilled the previous library requirements, was implemented in the Arduino code. The acceleration and speed values of the motor had to be optimized for the requirements of the static tests in order to ensure the motor repeatability during these tests and improve its precision.

Before calibrating, a microstepping of 8 was set in the stepper motor driver so that the motor movement was smoother and the available current was set to maximum in the same driver. These adjustments were also tried with the initial configuration without success. Hereupon, it was possible to proceed for the calibration of the stepper motor. So, in order to know how many steps were required for the motor to turn a certain cam angle, it was necessary to know the steps required for a full rotation. After knowing that, the required steps for any camshaft angle were discovered, some of which are found in Table 5.4.

Table 5.4: Motor steps and camshaft angle relations.

Camshaft degrees [º]	Motor steps
360	6400
180	3200
90	1600
45	800

As the motor turned, during the calibration procedure, the valve lifts were measured with the dial indicator so that a number of steps correspond to a certain camshaft angle which, in its turn, correspond to a certain valve lift. The steps, acceleration and speed for each studied valve lift were stored as variables in a function inside the code which is called every time the motor turns. Thus, the motor movement was optimized for each required valve lift.

Regarding the unsteady tests the Stepper library was used, since it allowed a constant motor speed during its motion. In order to find the input speed values which correspond to the desired rpm range (5, 10, 15 and 20), a stopwatch was used to time 60 s and during those seconds the number of full camshaft rotations was counted. This trial and error procedure was made until the input speed values matched the desired rpm.

5.4.2 Initial MAF sensor position

Similarly to the initial stepper motor layout at the test bench, the initial position of the MAF sensor was also different from the final one. Instead of being placed before every other component, the MAF sensor was initially placed between the throttle plate set and the intake manifold because it was believed, at that time, that the throttle plate had to be the first element to contact with the airflow, otherwise its effect on the airflow would not be sensed by the MAF sensor. For this arrangement, another connecting element, presented in Figure 5.8 (a), was designed and 3D printed to provide the linkage between the MAF sensor and the inlet manifold. This element had the same connecting section of the inlet manifold and, in the middle, a progressive increasing diameter section to allow this part to fit inside the MAF sensor and remain tight.

In this configuration, the throttle plate set was linked together with the MAF sensor and the sensor was connected to the inlet manifold through the connecting element, as shown in Figure 5.8 (b). However, during the preliminary tests, the flaws of this intake setup started to be noticed, leading to inconclusive and nonsense results. The throttle plate prevented the airflow from going straightly to the MAF sensor, which resulted in abnormal high air mass measurements when the throttle plate angle was at 50º and unnatural low air mass readings whenever the throttle plate angle was greater than 50º.

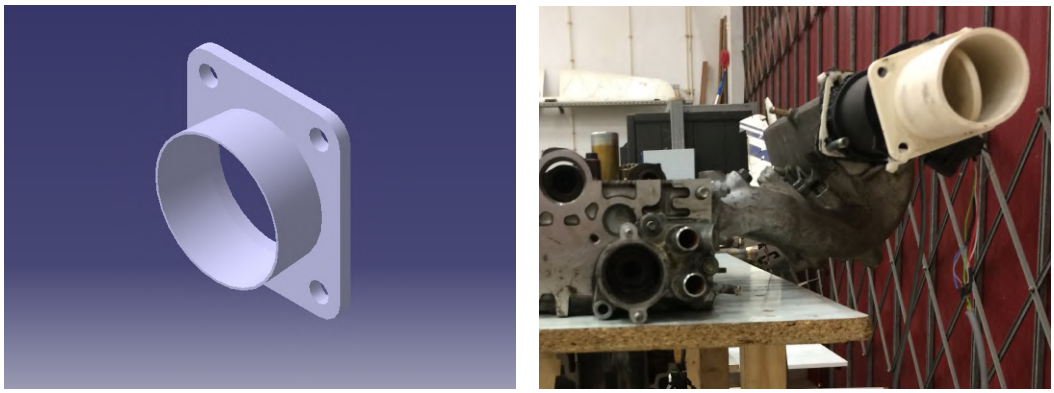

(a) Connecting part isometric view

(b) MAF sensor first layout

Figure 5.8: Initial MAF sensor layout at the test bench.

The solution for these nonsense results arose through the investigation of how the intake system of real carburettor engines is made. It was discovered that, in conventional carburettor engines, the throttle plate is always placed after the MAF sensor so that the airflow is undisturbed when it crosses the MAF sensor. Therefore, this inlet layout was forsaken and the final intake layout was adopted.

5.5 Experimental procedure

The entire set of experimental tests were carried out in the Propulsion laboratory of UBI. For a matter of simplicity, the static tests were conducted before the dynamic tests, being the standard valve strategy the first valve configuration to be analysed. A set of 5 tests were performed at each throttle plate position and without the throttle plate during the static and dynamic tests. The experimental procedure is quite similar for both tests conditions, existing

only minor differences that will be highlighted ahead in this section. Before the tests begin, several early checkings were required such as:

- Tight the tensioning system nut until the belt is properly stretched;
- Add oil to both camshafts fixings to provide a smoother rotation;
- Connect the hose, linked to the suction machine, to the bottom of the engine cylinder;
- Verify if the first set of camshaft lobes is positioned within the established reference;
- Enable a microstepping of 8 on the stepper motor driver.

After the previous tasks are completed, it is initiated the set of experimental steps performed in chronological order for the static condition.

1. Set the throttle plate angle to be analysed;
2. Turn on the custom power supply;
3. Connect the Arduino board linked to the sensors to the computer and upload the “Sensor readings” code;
4. Link the second Arduino Uno to the computer and upload the “Nema 23 static condition” code;
5. Turn on the suction machine;
6. Once the camshaft lobes reach the reference, disconnect the second Arduino and turn off the suction machine;
7. Repeat the procedure for the next throttle plate position.

Regarding the dynamic tests, few changes must be adopted to the static experimental procedure such as :

- The delay in the “Sensor readings” code is updated to 5ms
- The “Nema 23 dynamic condition” code is uploaded to the second Arduino Uno
- Disable the microstepping feature of the stepper motor driver
- After analysing one specific rpm, change the speed values in the code for the next speed to be studied

After the standard configuration being analysed, the valve deactivation strategy was evaluated through static and dynamic tests likewise the standard setup. In order to perform the latest tests, the inlet camshaft, presented in Figure 5.9 (a), had to be modified so that only one inlet valve would open during the tests. The modification made on the intake camshaft was done having in mind the possibility of studying an asymmetric valve lift configuration after the valve deactivation strategy is analysed. Thus, the cams on the fourth cylinder section of the inlet camshaft were trimmed until the shaft in order to allow the spindle chuck of the lathe to grab the camshaft on one side. For the other side, the helical gear was removed and a medium metal

sphere was used to make the contact between the tailstock assembly and the opposite side of the camshaft. Afterwards, the camshaft was cut as close as possible to the cam, which was farthest from the start in the first camshaft section, since if something went wrong the one valve configuration wouldn't be compromised. The final result is presented in Figure 5.9 (b).

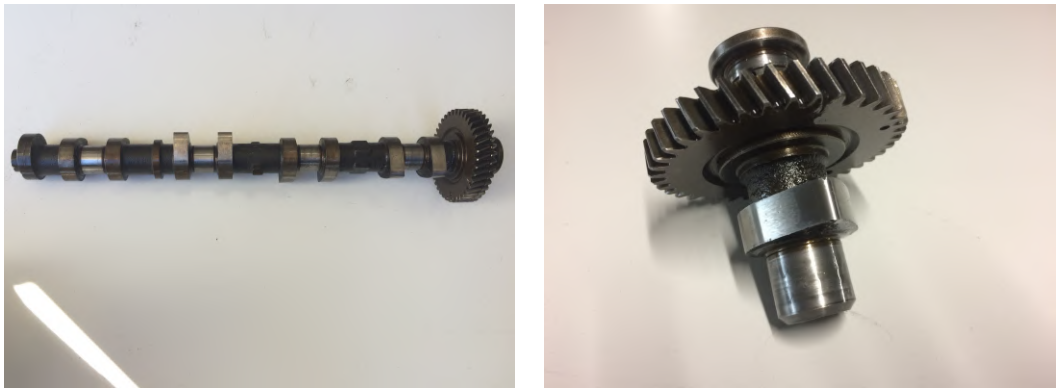

(a) standard configuration (b) One valve setup

Figure 5.9: Camshaft configurations.

Regarding the asymmetric strategy, it was not possible to perform it due to the MAF sensor which stopped sending information to the Arduino after the tests with a single intake valve.

Afterwards, the modified camshaft was mounted to the engine head and the same static and dynamic procedures were implemented. Figure 5.10 presents the experimental setup used to determine the discharge and flow coefficients.

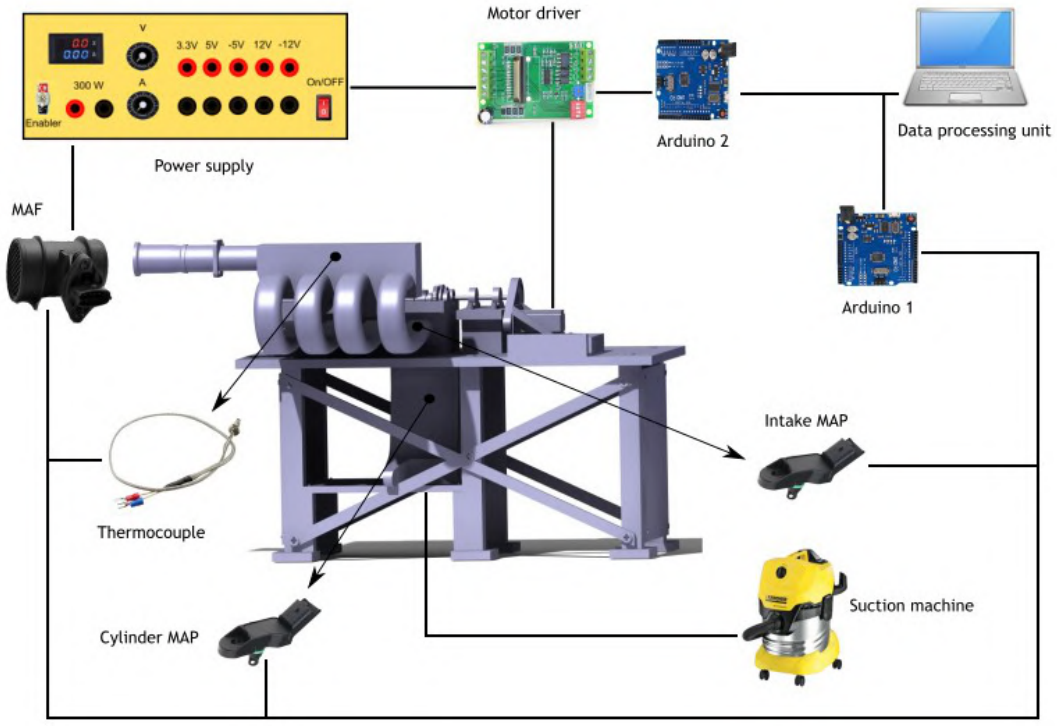

Figure 5.10: Experimental apparatus.

Throughout the experiment, three Arduino codes were used and, depending on the test condition, one of the two Arduino codes designed to control the stepper motor is implemented. The delay in data acquisition was set to 100 ms for static measurements and, during dynamic tests, a 5 ms delay was established in order to better notice the quick pressure and airflow variation. For the purpose to facilitate the data collection, it was installed the Tera Term program which collects the data registered in Arduino's serial monitor and stores it in a text file. This program is opened and synced with the first Arduino board after the fourth step of the experimental procedure during both tests conditions. This way, the collected data was sent to Microsoft Excel 2016 where it was analysed.

5.6 Results

Here are presented the results obtained during the experimental tests for the parameters of interest. Throughout the tests, atmospheric pressure was not always constant, at times it fluctuated, affecting the results. The small atmospheric pressure variation led to the rejection of some results since a small increase of the inlet pressure, higher than 2 kPa, resulted in a greater pressure differential across the intakes valves, and hence, an increased air mass flowing through the valves in comparison to other tests performed at lower inlet pressures. As the atmospheric pressure is impossible to control, an interval of valid values for the atmospheric pressure was set, (95 to 97 kPa), only tests within this range of atmospheric pressures were considered. The static results are shown first followed by the dynamic ones, where a comparison between the results obtained in both conditions is made in order to find out if they are in agreement. Some observations of what could have been done to improve the results are made and the believed reasons for some of the results to don't behave as expected are exposed.

5.6.1 Static condition

The results achieved during the standard and one valve setups are shown and compared in terms of the determined variables.

5.6.1.1 Discharge coefficient

The fluid dynamic efficiency of the studied engine was evaluated in terms of discharge and flow coefficients as a function of the dimensionless valve lift, as shown in Figure 5.11. The results refer to the first valve configuration and the setup without throttle plate. According to Figure 5.11, the flow coefficient progressively increases with valve lift, while the discharge coefficient increases until a certain lift (L_v/D=0.032) and gradually decreases as the valve lift continues to increase. Furthermore, it is visible the presence of three regions which according to literature [1, 19, 43], correspond to different flow patterns across the valves. These distinct flow regimes are characterized by different slopes in the discharge coefficient curve. At low valve lifts, high values of discharge coefficient are observed due to the high viscous phenomena that maintain the flow attached to the valve head and seat. As the valve lift and curtain area further increases, flow separation occurs first at the valve head, roughly between L_v/D=0.05 until 0.10, and then at the valve seat. As a result, the flow becomes less and less able to fill the growing curtain area, resulting in a gradual decrease of the head breathability as well as the discharge coefficient.

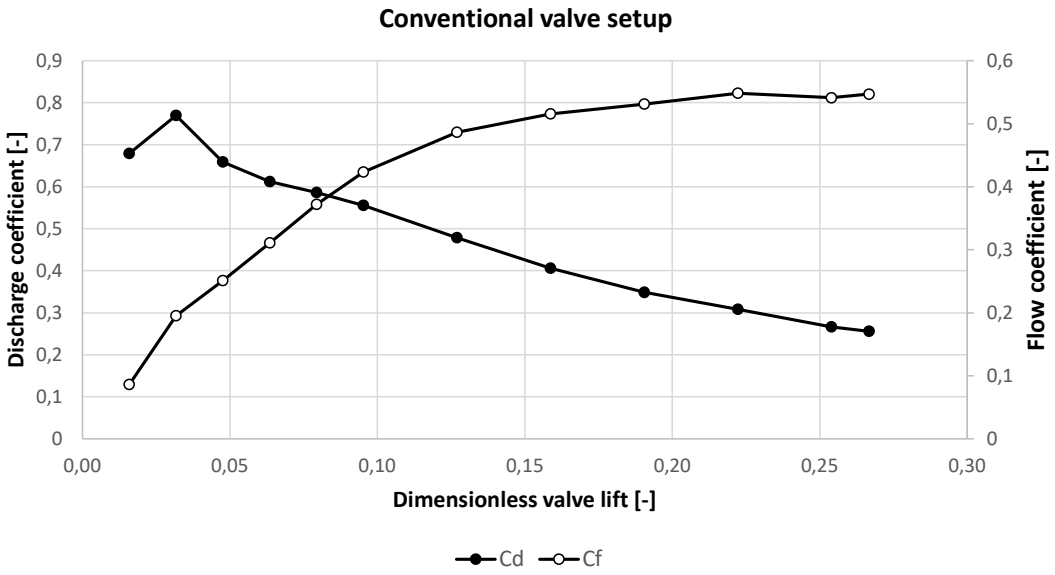

Figure 5.11: Influence of valve lift on the engine breathability. Configuration without throttle.

In order to evaluate the throttling effect on engine breathing, the fluid dynamic efficiency is analysed for both valve setups and different throttle plate angles. Figure 5.12 shows the behaviour of the discharge coefficient at several throttle plate angles and without a throttle plate for a conventional valve lift setup. From Figure 5.12 is clear that adding a throttle plate to the inlet system has a negative impact on the discharge coefficient and consequently to engine breathing. It is quite noticeable that as the throttle plate angle increases, the airflow passing through the valves also increases, leading to a better filling of the curtain area and, thus, to a higher discharge coefficient. Moreover, the presence of the three flow regimes is observed in all throttled configurations as in the no throttle plate setup. These results are in line with the results obtained by investigators in their experimental works [1, 43].

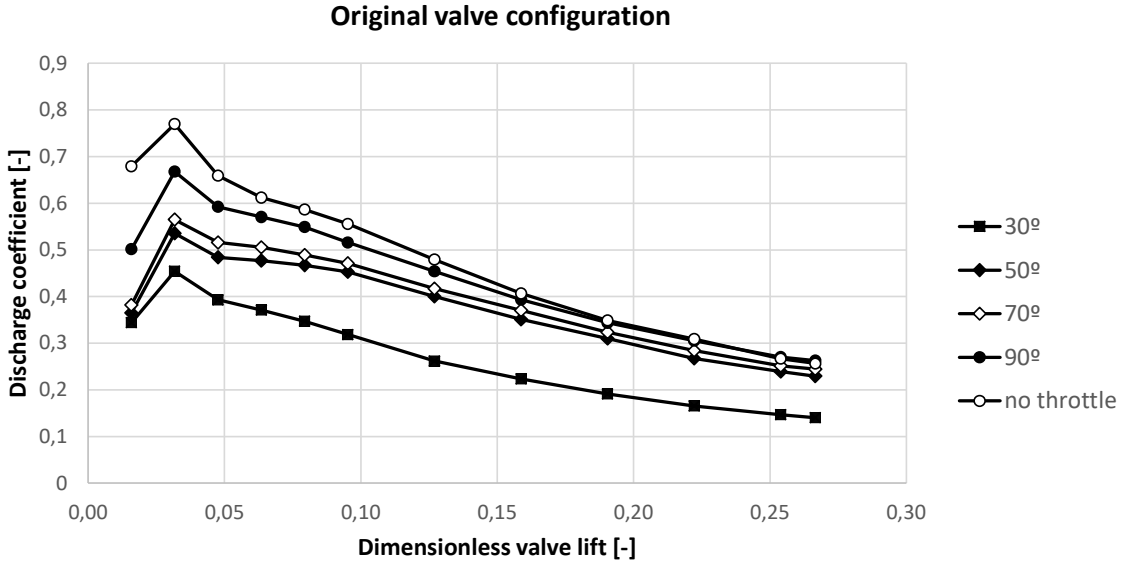

Figure 5.12: The effect of adding a throttle plate on the discharge coefficient.

In Figure 5.13 an individual comparison of both valve configurations in terms of discharge coefficient is shown for each throttle setting and to the no throttle setup. What immediately stands out is the fact that the alternative valve strategy achieves higher values of discharge coefficient than the original valve configuration throughout the entire valve lift range. This tendency was

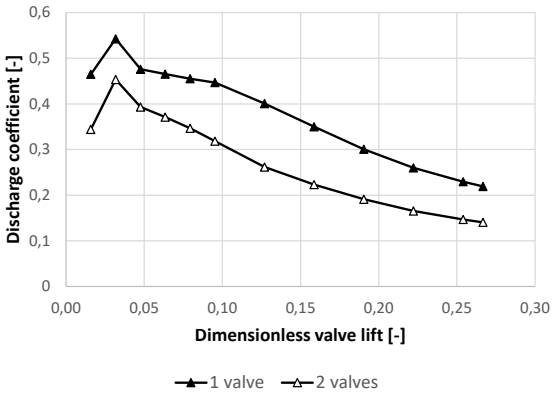

(a) 30°

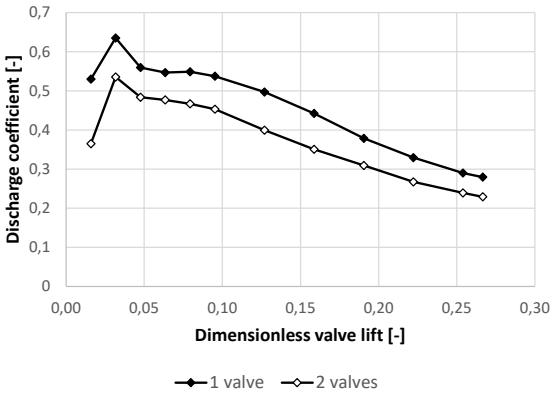

(b) 50°

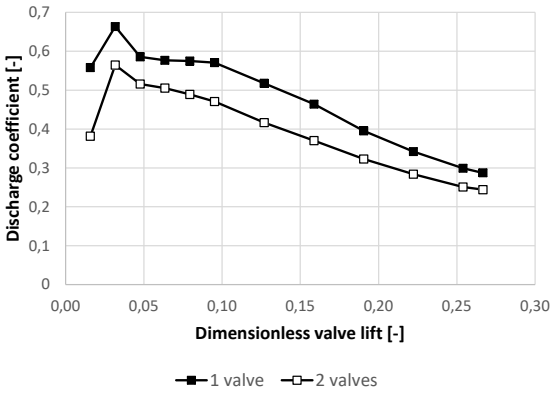

(c) 70°

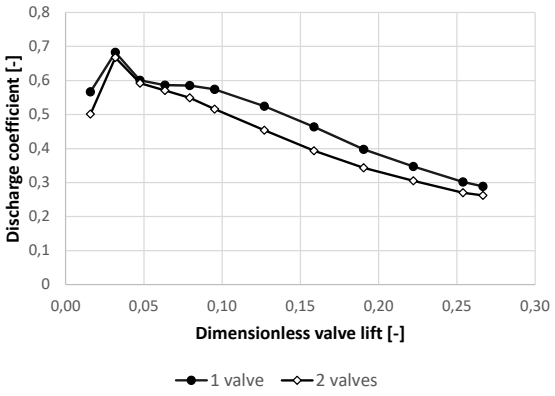

(d) WOT

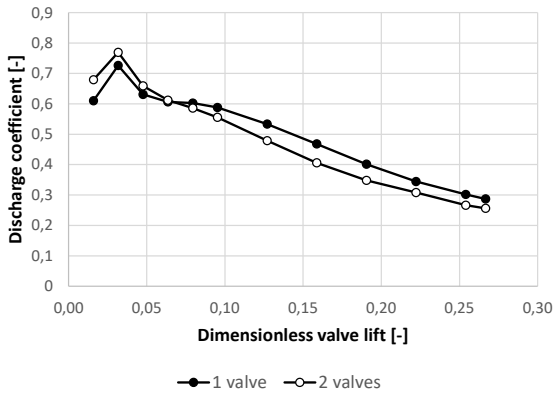

(e) without throttle plate

Figure 5.13: Influence of the valve interference phenomena on the discharge coefficient.

obtained for almost every throttle conditions, as shown in Figures 5.13 (a,b,c and d), but was not attained, at low valve lifts, for the condition without throttle plate, as depicted in Figure 5.13 (e). The first prior results are in line with investigators works [45] and highlight the large negative effect of the valve interference phenomena on the head breathability. This phenomenon creates a significant distortion of the flow field inside the valve gap, being typically greater when both inlet valves are opened. The absence of flow interference between valves results in a better filling of the curtain area and a more uniform flow distribution across the valve gap, which lead to higher discharge coefficients whenever only one inlet valve is opened.

Regarding the different behaviour shown in the setting without a throttle plate, it is believed that flow irregularities created in the bifurcation of the intake port could have played a role in the reduction of the discharge coefficients at low valve lifts since this condition produces the greatest airflows moving through the port-valve assembly. Furthermore, a slightly different MAF sensor positioning could have also contributed to the unexpected early results due to its high position sensitivity. As expected, the presence of the three flow regimes is detected in both valve strategies.

5.6.1.2 Flow coefficient

The flow coefficient must also be evaluated for the different test conditions and valve configurations if the fluid dynamic efficiency of a multi-valve engine is to be studied. This parameter, in contrast with the discharge coefficient, measures the degree of flow restriction across the intake port, and hence, the inlet port efficiency. Figure 5.14 illustrates a comparison between a clean airflow setup and several throttled settings on the inlet ports efficiency when a conventional valve lift is implemented.

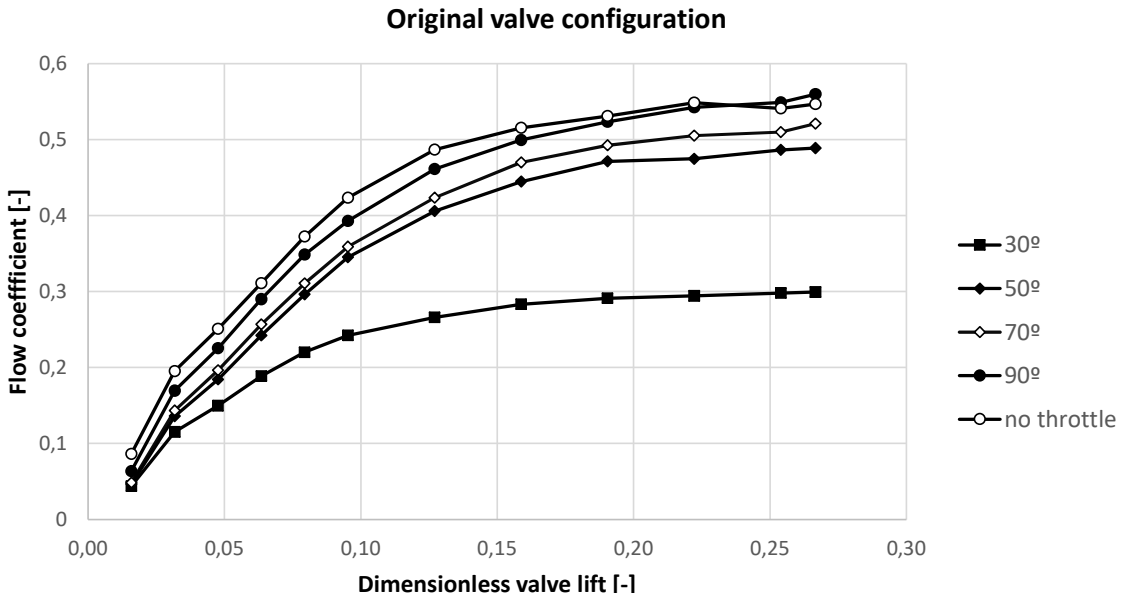

Figure 5.14: The influence of throttled settings on the flow coefficient.

From Figure 5.14, it can be concluded that as the throttle plate angle reduces the flow coefficient also decreases due to the reduction of airflow flowing through the inlet ports. Furthermore, it can be observed that the setup without throttle plate obtains the highest flow

coefficients results by a minor difference in relation to the WOT configuration because the increased airflow from a WOT to the no throttle condition is quite small. Indeed this slim airflow difference between the three highest throttle plate angles and the setup without throttle plate causes big proximity in terms of flow coefficients of these settings, as Figure 5.14 illustrates. It worths point out that after a certain valve lift (L_v/D=0.20), the flow coefficient is approximately constant for all the studied setups probably due to the inlet port dimensions, which limit the amount of airflow entering the cylinder after a specific valve lift.

Likewise in the discharge coefficient case, the alternative valve strategy was also studied in terms of flow coefficient. The results for both valve configurations are illustrated in Figures 5.15 (a) and (b), where only the two most critical setups are shown since the same tendency was verified for the other throttle setups. According to both Figures, the flow coefficient behaves the same for the two valve strategies, as expected. The two valves configuration obtained the greatest flow coefficients for every throttled setup as well as in the no throttle arrangement. The reason is that a double intake valve setup allows much greater airflows and the flow irregularities created in the bifurcation of the intake port are quite lower when compared with the alternative valve strategy.

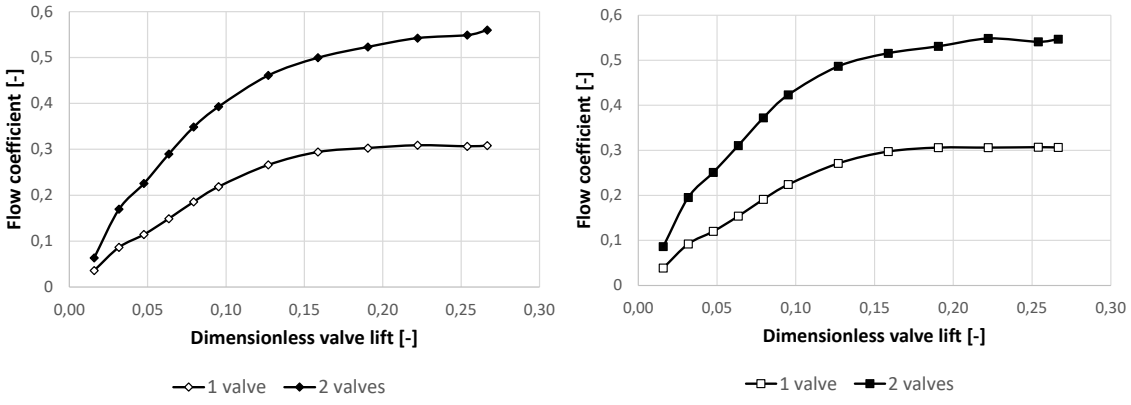

(a) WOT

(b) No throttle plate setup

Figure 5.15: Effect of valve deactivation on the flow coefficient

5.6.2 Dynamic condition

Engine breathability was also investigated during unsteady conditions in order to discover if the studied parameters suffer any changes in relation to the static condition. In order to plot the unsteady data, it was created a code, developed in Python, to determine the camshaft angle and valve lift step using the Trapezoidal method since it was not possible to measure these variables during this operating condition. The code also calculates the mean discharge and flow coefficients according to the cam angle through Equations 5.2 and 5.3 for both valve strategies and the four considered rpm.

$$C_{dmean} = \frac{\int_{\alpha_{IVO}}^{\alpha_{IVC}} C_d(\alpha)\mathrm{d}\alpha}{\alpha_{IVC} - \alpha_{IVO}} \quad (5.2)$$

$$C_{fmean} = \frac{\int_{\alpha_{IVO}}^{\alpha_{IVC}} C_f(\alpha)\mathrm{d}\alpha}{\alpha_{IVC} - \alpha_{IVO}} \quad (5.3)$$

where

C_d and C_f are the discharge and flow coefficients between the IVO and IVC, respectively.
α_{IVO} is the cam IVO angle.
α_{IVC} is the cam IVC angle.

In addition, the code approximates the integral by the Trapezoidal rule and send the mean coefficient values to an excel sheet. The code can be found in Appendix G.

5.6.2.1 Discharge coefficient

The original valve configuration was firstly analysed since it was the first valve strategy to be studied. Figure 5.16 presents the dynamic data in terms of discharge coefficient as a function of the cam angle for the four considered rpm. In each rpm, the four throttle plate angles and the

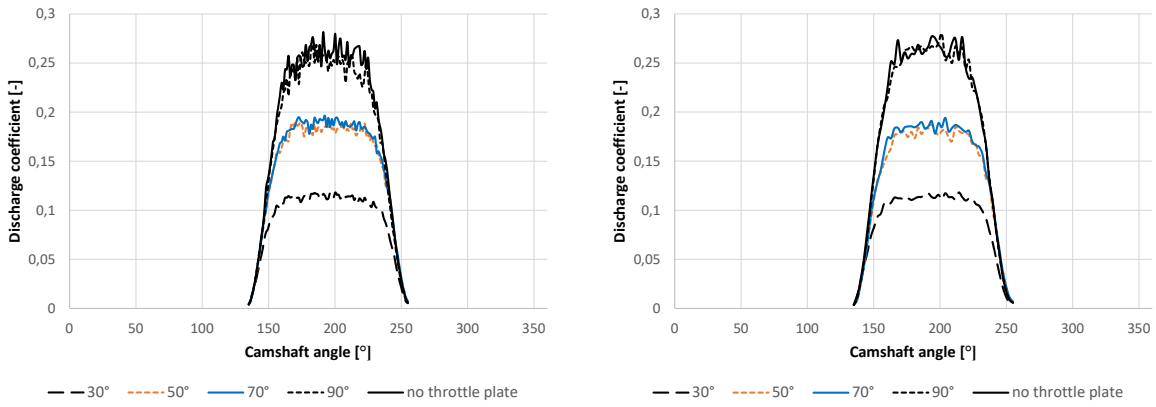

(a) 5rpm

(b) 10rpm

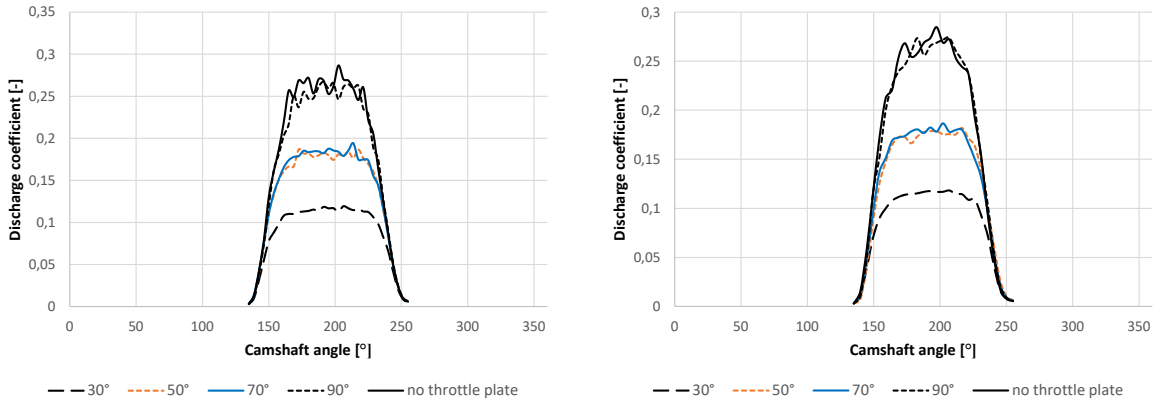

(c) 15rpm

(d) 20rpm

Figure 5.16: Evolution of the dynamic discharge coefficient in each rpm according to the cam angle. Standard valve setup.

clean setup are evaluated. From Figure 5.16, it is evident the sensor's noise in the data which increase with the throttle angle, being maximum for the no throttle setting. This fact makes it difficult to interpret the results, but even so, some conclusions can be drawn. In every studied rpm, the configuration without throttle plate achieves the highest discharge coefficients, followed very closely by the WOT position. The 70º and 50º throttle angles appear next, having a quite noticeable difference between the WOT and the setup without throttle plate. Lastly but not least, it comes the 30º throttle setting which detains the lowest discharge coefficient values. This results support the tendency observed in the static data where a configuration without throttle plate obtains the best discharge coefficients and an increase of the throttle plate angle causes an upsurge of the discharge coefficient.

According to Figure 5.16, as the cam angle increases, the discharge coefficient also gets bigger due to the airflow upsurge, but roughly at about 170º of the camshaft, the airflow becomes stable and cannot increase any more because of the inlet port dimensions. Therefore, after the previous cam angle, the discharge coefficient remains approximately constant, decreasing when the intake valves start closing.

To better notice the variation of the discharge coefficient among the different throttle settings, configuration without the throttle plate and rpm, the mean discharge coefficients were calculated for each previous condition and both valve strategies. This was possible due to the python code which was developed to allow a more accurate comparison among the study variables. Thus, the mean discharge coefficients are presented in Table 5.5, where the "Average coefficient two valve" and "Average coefficient one valve" are the mean coefficients for the original and alternative valve setups, respectively. For the sake of simplicity, the configuration without the throttle plate is shown as NTP.

From Table 5.5 it is possible to conclude that, likewise in the static tests, the alternative valve strategy obtains the highest discharge coefficients comparatively to the conventional valve setup for every evaluated rpm, throttle setting and the no throttle configuration. It is noteworthy that as the camshaft velocity increases the mean discharge coefficient slightly reduces considering the same throttle or the no throttle setting throughout the rpm range. This tendency is observed in both valve strategies and is in line with the literature [48]. It is believed that for higher and more spaced rpm values the mean discharge coefficient will fall more noticeably since in Oh et al. experimental work [42] the flow coefficients fell more sharply as the camshaft velocity increased to greater values.

In order to compare with the static results, the dynamic discharge coefficients for each analysed rpm are presented as a function of the dimensionless valve lift in Figure 5.17. As usual, the four throttle settings and the no throttle setup are evaluated. According to Figure 5.17, the discharge coefficient behaves the same way as in static tests for all studied rpm, increasing until a certain valve lift and decreasing after that lift. As expected, the no throttle setup achieves the highest discharge coefficient values and the lowest throttle angle obtains the worst discharge coefficients. Although the previous conclusions agree with the static tests, it is possible to clearly observe only two flow regimes for all rpm and throttle/no throttle setting. It is suspected that the sensor's noise makes it impossible to perceive the intermediate flow regime.

Table 5.5: Mean discharge coefficients for both valve strategies.

Velocity [rpm]	Throttle setting	Average coefficient two valve	Average coefficient one valve
5	30	0.0919	0.1641
	50	0.1438	0.2166
	70	0.1474	0.2269
	90	0.1844	0.2336
	NTP	0.1928	0.2366
10	30	0.0894	0.1629
	50	0.1367	0.2106
	70	0.1410	0.2198
	90	0.1810	0.2271
	NTP	0.1900	0.2296
15	30	0.0888	0.1597
	50	0.1345	0.2062
	70	0.1365	0.2144
	90	0.1789	0.2178
	NTP	0.1852	0.2180
20	30	0.0855	0.1547
	50	0.1269	0.1910
	70	0.1284	0.2010
	90	0.1759	0.2058
	NTP	0.1778	0.2061

5.6.2.2 Flow coefficient

A dynamic analysis was also performed in terms of flow coefficient to evaluate the inlet ports efficiency during unsteady conditions. Likewise the dynamic discharge coefficients, the unsteady flow coefficients are exhibited in Figure 5.18 as a function of the cam angle for the conventional valve configuration. Only the two furthest camshaft velocities are presented since the same tendency was verified in the two intermediate camshaft speeds.

According to Figure 5.18, the same conclusion as in the static tests can be drawn which is as the blocking of airflow in the inlet system reduces the dynamic and static flow coefficients increase. This way, the no throttle plate setup achieves the highest flow coefficients being followed by the other throttle configurations. The evolution of the unsteady flow coefficients according to the cam angle is approximately the same as the dynamic discharge coefficients probably due to its airflow dependency.

In order to compare the dynamic data obtained for each valve strategy, the mean flow coefficients for both valve setups, each throttle setting and rpm, as well as the no throttle configuration, were determined through the python code. These coefficients are registered in Table 5.6, where ”Mean coefficient 1” and ”Mean coefficient 2” are the mean flow coefficients for the original and alternative valve setups, respectively.

After analysing Table 5.6, it is clear that the two inlet valve configuration for every throttle,

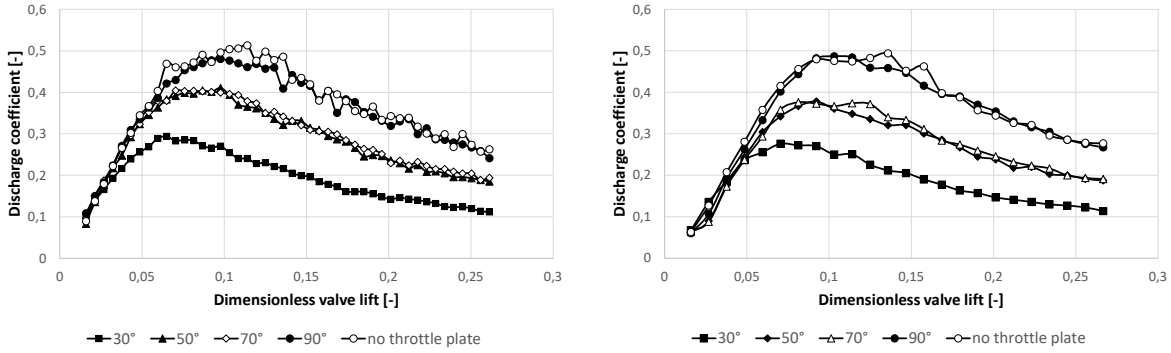

(a) 5rpm

(b) 10rpm

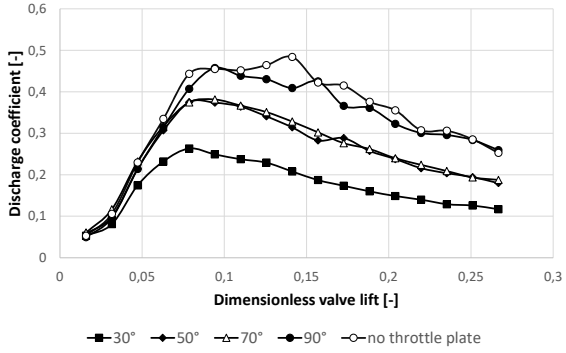

(c) 15rpm

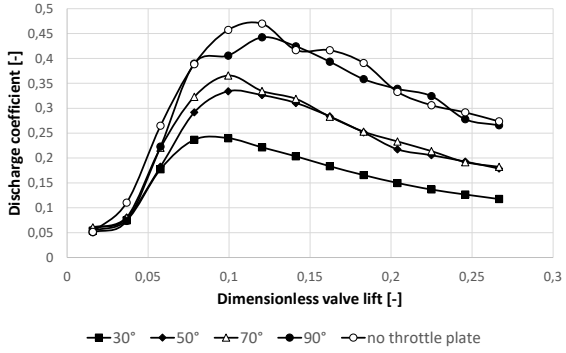

(d) 20rpm

Figure 5.17: Dynamic discharge coefficients as a function of the dimensionless valve lift throughout the rpm range. Original valve configuration.

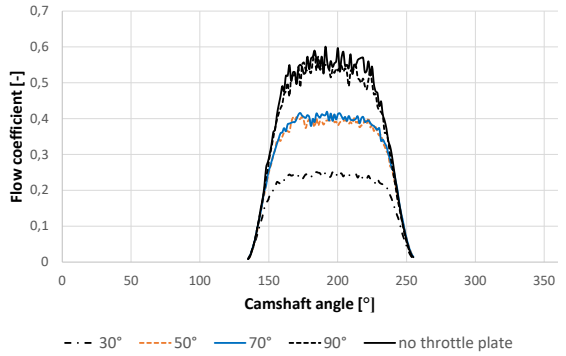

(a) 5rpm

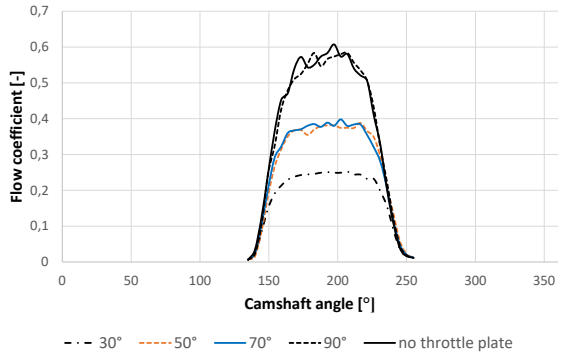

(b) 20rpm

Figure 5.18: Variation of the dynamic flow coefficients in the lowest and highest rpm according to the cam angle. Standard valve setup.

camshaft velocity and for the no throttle configuration obtains the highest flow coefficients when compared to the alternative strategy. This result supports the ones obtained during static tests. Another aspect to point out is the slight reduction of the mean flow coefficient as the camshaft velocity increases when the same throttle/no throttle setting is considered. This

finding is in line with the experimental work of Oh et al. [42] which concluded that unsteady flow coefficients decrease as the camshaft velocity increases and the degree of reduction is proportional to the rpm difference. This way, the small reduction of the mean flow coefficient is justified by the quite narrow studied rpm range .

Table 5.6: Mean flow coefficients for both valve strategies.

Velocity [rpm]	Throttle setting	Mean coefficient 1	Mean coefficient 2
5	30	0.1960	0.1751
	50	0.3067	0.2310
	70	0.3144	0.2420
	90	0.3935	0.2491
	NTP	0.4113	0.2524
10	30	0.1908	0.1738
	50	0.2917	0.2247
	70	0.3008	0.2345
	90	0.3883	0.2422
	NTP	0.4052	0.2449
15	30	0.1894	0.1703
	50	0.2869	0.2200
	70	0.2911	0.2287
	90	0.3817	0.2323
	NTP	0.3952	0.2326
20	30	0.1825	0.1650
	50	0.2708	0.2037
	70	0.2739	0.2144
	90	0.3752	0.2196
	NTP	0.3794	0.2198

Lastly, the dynamic flow coefficients obtained in the lowest and higher rpm are presented in Figure 5.19 as a function of the dimensionless valve lift for the original valve configuration and the different blocking conditions. Only the two extremes of the rpm range are shown since the

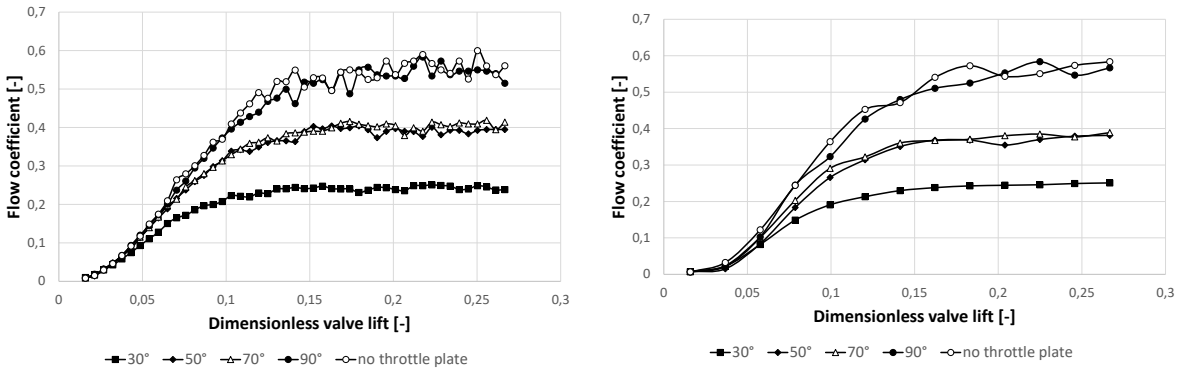

(a) 5rpm

(b) 20rpm

Figure 5.19: Evolution of the dynamic flow coefficient in each extreme of the studied rpm range according to the dimensionless valve lift. Standard valve setup.

same tendency was achieved over all studied rpm. From Figure 5.19, the evolution of the flow coefficient as the valve lift increases is quite similar to the behaviour demonstrated during the static tests. Furthermore, it is possible to observe the same tendency over the course of the experiment which is the no throttle plate setting again detains the best engine breathing characteristics, and as the throttle plate angle decreases the engine breathability gets worse.

5.7 Uncertainty in measurements

Throughout the tests, several sensors were used to determine the experimental discharge and flow coefficients. Since the error of the used sensors cannot be known, the relative uncertainty in measurements of each sensor was calculated through the standard deviation. This parameter was estimated by making an average of a certain amount of values obtained for each sensor (100) and using Equation 5.4 [54].

$$s = \sqrt{\frac{\sum \partial x_i^2}{(N_{sensor} - 1)}}, \qquad \partial x_i = x_i - \bar{x} \quad (5.4)$$

where

x_i is a certain measurement.
$\bar{x}$ is the measurements average.
N_{sensor} is the number of measurements.

The thermocouple readings over the entire set of tests were constant due to the delay being set to a lower value than the minimum withstand by the sensor to allow some variation. For this reason, the standard deviation of this sensor was ignored. The uncertainty associated with the average measurements is the standard deviation of the mean which is given by [54]

$$\sigma_{\bar{x}} = \frac{s}{\sqrt{N}} \quad (5.5)$$

After applying the previous equations, the relative uncertainty of the MAF sensor was roughly 3% and the inlet and cylinder MAP sensors uncertainty was approximately 7% and 2%, respectively. The dial indicator used to calibrate the stepper motor had an absolute uncertainty of 0.05. Since several measurement instruments were used to calculate the discharge and flow coefficients, it becomes required to calculate the propagation of uncertainty. Knowing that both discharge and flow coefficients depend from the airflow and the pressures before and after the inlet valve, in other words, are a function ”f” dependent of ”x”, ”y” and ”z”, the relative uncertainty is determined by [54]

$$\frac{\sigma f}{f} = \sqrt{\left(\frac{\sigma x}{x}\right)^2 + \left(\frac{\sigma y}{y}\right)^2 + \left(\frac{\sigma z}{z}\right)^2} \quad (5.6)$$

The relative uncertainty in the discharge and flow coefficients was roughly 3.3%.

Chapter 6

Conclusions and Future works

As the work evolved, several conclusions were obtained regarding the effect of different conditions and throttle/valve configurations on the discharge and flow coefficients. This chapter focuses on highlighting the achieved goals, difficulties encountered during tests and the conclusions evidenced in the experimental tests. Finally, several recommendations are presented on what could be developed in future works regarding this topic.

6.1 Conclusions

The growing concern about engine emissions and fuel consumption has led to the search for newer ways to improve engine efficiency. The study of the airflow across the inlet system has given several clues to further engine performance improvements by identifying various factors and phenomena which strongly affect engine breathing and efficiency. There are a considerable number of factors that change the inlet flow, and for this reason, it is difficult to design an inlet system that accomplishes every requirement set by these factors. On one hand, it is required a proper design and optimization of the intake manifold for the pulsed flow through intake tuning since it contributes to better engine performance characteristics. On the other hand the fuel system implemented, and the properties of the inlet fluid must also be taken into account at the preliminary designing stage of the inlet system. Therefore, to achieve the best possible flow characteristics at the inlet valves, a compromise must be made at the designing phase of the induction system.

The airflow is also affected by the port and valve geometry, valve timing, lift, and size. To better understand the effect of changing one of these variables, discharge and flow coefficients are defined and evaluated under different intake configurations, conditions and valve/port geometries. These coefficients measure the fluid dynamic efficiency of the inlet valve and port respectively, being indicators of how efficiently air is being drawn into the cylinder during the intake stroke.

In this sense, an investigation was launched having as the main goal the study of the fluid dynamic efficiency of a multi-valve SI engine under static and dynamic conditions for different inlet valve strategies and intake system configurations. Almost every proposed objective was accomplished, namely the analysis of having a throttle body in the inlet system at several throttle positions and compare it with a clean inlet setup, evaluate and compare the original valve configuration with the valve deactivation strategy and obtain the static and dynamic discharge and flow coefficient values for every attainable condition. Nevertheless, some objectives like the study of an asymmetric valve lift condition could not be achieved due to the MAF sensor's inability to send the output voltage to the Arduino board after the valve deactivation strategy was analysed. Furthermore, it was only possible to study the fluid dynamic efficiency of one engine since it is quite a time-consuming task to properly set up the sensors, as well as build

and design a test bench for a specific engine.

Several difficulties were encountered over the experimental tests which, in a certain way, led to inconsistent results. The atmospheric pressure was not always constant, fluctuating throughout the tests. Whenever the atmospheric pressure difference among tests was over 2 kPa, it affected the results, making it impossible to obtain reliable results in all tests. As the tests were being repeated, it was verified that for an atmospheric pressure variation lower than 2 kPa, the results would not be overly influenced. So, a range of valid atmospheric pressure values was set (95 to 97 kPa) and only tests within this pressure range were considered. Curiously, the atmospheric pressure variation enabled us to perceive the influence of the suction pressure on the discharge and flow coefficients which was another goal of this work. A higher atmospheric pressure, around 5 kPa greater, resulted in an increased pressure differential across the inlet valve, leading to considerably higher discharge and flow coefficients.

Another faced obstacle was the MAF sensor's positioning sensibility which was rather high, forcing the repetition of several tests due to the impossibility of ensuring the same MAF positioning for every test, especially for the original valve configuration, which was the first valve configuration to be tested. The connecting element, which made the bridge between the throttle plate set and the MAF sensor, did not fit properly in the throttle plate set, having a slack which made it quite impossible to obtain the exact previous MAF positioning whenever the throttle plate angle was changed. This trouble was significantly reduced by adding thickness to the throttle set.

The research revealed the high sensibility of the discharge and flow coefficients to several inlet and valve conditions. It was found that the valve lift strongly affects both coefficients since the flow coefficient gradually increased with the valve lift, remaining approximately constant for high valve lifts, whereas the discharge coefficient increased until a certain lift (L_v/D=0.032) and progressively decreased as the valve lift continued to increase. Different flow regimes, which correspond to distinct flow patterns across the valve, were identified, as well as the flow separation at the valve head and seat during medium and high valve lifts.

Regarding the effect of throttled flow on the engine head breathability, the experimental results show that the setup without a throttle plate attained the best discharge and flow coefficients and as the throttle plate angle increased, higher discharge and flow coefficients were obtained. This trend was achieved in both valve strategies, as well as in the static and dynamic tests, highlighting the negative effect of adding a throttle plate to the intake system.

In order to study the influence of the valve interference phenomenon on the engine fluid dynamic efficiency, the original and an alternative valve configuration were investigated. It was found that the valve deactivation strategy obtained higher discharge coefficients when compared to the conventional one since the valve interference is typically greater when both inlet valves are opened. In contrast, the two valve configuration achieved higher flow coefficients probably due to the greater airflow it allows and the low flow irregularities created in the bifurcation of the inlet port comparatively to the one valve setup. The latter conclusion was achieved for every studied rpm, throttle setting and the setup without throttle plate. However, the prior outcome was not attained during the static test for the configuration without throttle. It is believed that a slightly different MAF sensor positioning from the other throttle setups may

have contributed to the unexpected result.

Static and dynamic tests were carried out in the studied engine in order to examine if steady discharge and flow coefficients can predict the dynamic performance of the valve-port assembly. Overall, the static and dynamic results agree with each other, proving that steady coefficients can predict with good accuracy the unsteady behaviour of the intake valve and port.

Dynamic results show that according to the cam angle, both coefficients behave the same manner, increasing initially with the cam angle until a certain angle, remain constant and decrease once the inlet valve starts closing.

Regarding the effect of the camshaft velocity on engine breathing, mean discharge and flow coefficients were determined through a python code to allow a more accurate comparison among the studied variables. It was found that for the same throttle angle and setup without a throttle plate, the mean discharge and flow coefficients slightly decrease as the camshaft speed increases. According to the results and some studies, it is hoped that for higher and more spaced camshaft velocities both coefficients fall more sharply.

6.2 Future works

As mentioned in the course of this dissertation, it was not possible to study an asymmetric valve lift. In multi-valve engines, this strategy, as well as the deactivation of one valve, are promising since it appears that a significant improvement in fuel consumption can be achieved in comparison to the conventional valve setup. In this sense, it is suggested the analysis of the fluid dynamic efficiency of the same studied engine for an asymmetric valve lift condition in order to compare with the two different valve strategies already covered in this work.

In the sense to validate this experimental work, it is recommended a numerical study which covers every inlet and valve conditions investigated.

In order to better understand how engine breathability behaves in real engine operating conditions, it is recommended the use of the piston engine to cause the pressure drop across the inlet valve instead of a suction machine or blower and the study of higher engine rpm ranges. Furthermore, it should be also interesting to raise the bar by evaluating engine breathing in more than one cylinder at the same time to understand how the airflow and both coefficients behave in that kind of situation.

Throughout this work, several important variables couldn't be analysed which would give a better idea of what could be improved in future valve-port assemblies in order to maximize both coefficients of interest. This way, it is proposed the experimental study of several engines and inlet ports/valve geometries so that a discharge and flow coefficient database based on experimental coefficients can be created and the valve/port characteristics that optimize engine breathing for a specific engine can be known. In addition, it is suggested the development of a valve-port sizing program, based on the database, that selects the correspondent discharge and flow coefficients according to the engine and valve-port features.

Bibliography

[1] A. Algieri, "Comparative analysis of the fluid dynamic efficiency of standard and alternative intake strategies for multivalve spark-ignition engines," *International Journal of Engineering and Technology*, vol. 2, no. 2, pp. 140–148, 2013. 1, 32, 35, 36, 65, 77, 78

[2] C. Arcoumanis, *Internal Combustion Engines*. Academic Press, 1988. 5, 6

[3] JD Laukkonen, "History of the Internal Combustion Engine," 2013, visited on 03/04/2019. [Online]. Available: http://www.crankshift.com/history-internal-combustion-engine/ 5

[4] B. Sanbongi, "The aircraft engine: An historical perspective of engine development through world war i," *Journal of Aviation/Aerospace Education & Research*, vol. 8, no. 3, p. 7, 1999. 5, 6, 7

[5] C. F. Taylor, *Aircraft propulsion; a review of the evolution of aircraft piston engines*. SMITHSONIAN INSTITUTION PRESS, 1971, vol. 1, no. 4. 5, 6, 7, 8

[6] W. W. Pulkrabek, *Engineering Fundamentals of the Internal Combustion Engine*, united states ed. Prentice Hall, 1997. 5, 6, 9, 10, 11, 12, 17, 20, 21, 22, 24, 25, 26, 29

[7] C. R. Ferguson and A. T. Kirkpatrick, *Internal combustion engines: applied thermosciences*, 3rd ed. John Wiley & Sons, 2015. 5, 6, 8, 16, 17, 20, 25, 26, 28, 29, 30, 32, 33

[8] John B Heywood, *Internal combustion engine fundamentals*, 1st ed. Mcgraw-hill New York, 1988. 6, 9, 10, 11, 16, 17, 21, 22, 30, 31, 32, 33, 39, 40

[9] Science Museum Group Collection, "Crossley Otto 'Silent' Horizontal Engine," visited on 03/04/2019. [Online]. Available: http://collection.sciencemuseum.org.uk/objects/co62004/crossley-otto-silent-horizontal-engine-internal-combusion-engine 6

[10] R. Stone, *Introduction to internal combustion engines*, 4th ed. Palgrave Macmillan, 2012. 6, 10, 11, 13, 15, 16, 18, 20, 21, 22, 24, 25, 26, 27, 29, 30

[11] Pilotfriend, "Piston Engine development," visited on 05/04/2019. [Online]. Available: http://www.pilotfriend.com/aero_engines/aero_pst_eng.htm#r 6, 7, 8

[12] Pilotfriend, "Aircraft engine history," visited on 05/04/2019. [Online]. Available: http://www.pilotfriend.com/aero_engines/aero_early_history.htm 7

[13] National Air and Space Museum in Washington, DC., "Gnome Omega No. 1 Rotary Engine," visited on 05/04/2019. [Online]. Available: https://airandspace.si.edu/collection-objects/gnome-omega-no-1-rotary-engine 7

[14] T.A. Heppenheimer, "Rolls-Royce and Its Aircraft Engines," visited on 06/04/2019. [Online]. Available: https://www.centennialofflight.net/essay/Aerospace/Rolls-Royce/Aero54.htm 8

[15] nick123n, "P-51 Mustang Engine," visited on 06/04/2019. [Online]. Available: https://www.flickr.com/photos/27044274@N06/5654376207 8

[16] Pilotfriend, "Aircraft engine history," visited on 05/04/2019. [Online]. Available: http://www.pilotfriend.com/aero_engines/aero_eng_dvmt.htm#r 8

[17] J. M. M. Barata, *Propulsão: Motores Alternativos de Combustão Interna*. Universidade da Beira Interiror, 2011, vol. 3. 10, 17, 22, 28, 29

[18] J. L. Lumley, *Engines: an introduction*. Cambridge University Press, 1999. 11, 12, 13, 18, 22, 25, 26, 29, 30, 32

[19] W. J. D. Annand and G. E. Roe, *Gas flow in the internal combustion engine: power, performance, emission control, and silencing*. GT Foulis, 1974. 15, 16, 17, 18, 21, 22, 23, 30, 33, 34, 40, 41, 42, 43, 77

[20] S. Aadepu *et al.*, "Design of intake manifold of ic engines with improved volumetric effi ciency," *Internatıonal Journal & Magazıne of Engıneerıng, Technology, Management And Research*, vol. 1, no. 6, pp. 26–33, 2014. 15

[21] J. Benajes *et al.*, "Predesign model for intake manifolds in internal combustion engines," *SAE transactions*, pp. 182–193, 1997. 15

[22] x-engineer org, "How to calculate the volumetric efficiency of an internal combustion engine," visited on 13/05/2019. [Online]. Available: https://x-engineer.org/automotive-engineering/internal-combustion-engines/performance/calculate-volumetric-efficiency/ 16

[23] M. Ceviz, "Intake plenum volume and its influence on the engine performance, cyclic variability and emissions," *Energy Conversion and Management*, vol. 48, no. 3, pp. 961–966, 2006. 17, 18

[24] R. Royo *et al.*, "Optimal Design of the Intake System in 4-S I.C.E." SAE International, Tech. Rep., 1994. 17, 20

[25] J. Bayas *et al.*, "A review paper on effect of intake manifold geometry on performance of ic engine," *International Journal of Advance Research and Innovative Ideas in Education*, vol. 2, no. 2, pp. 101–106, 2016. 17, 18

[26] A. C. Alkidas and G. Sammut, "Relative Contributions of Intake and Exhaust Tuning on SI Engine Breathing - A Computational Study," SAE International, Tech. Rep., 2007. 17, 19

[27] F. Khassaf, "The breathing of four stroke internal combustion engines," Ph.D. dissertation, Loughborough University, 1969. 18, 19, 22, 32

[28] I. Dokadiya, "PERFORMANCE ENHANCEMENT OF 4-STROKE SINGLE CYLINDER SI ENGINE BY VARYING INTAKE LENGTH," *International Research Journal of Engineering and Technology*, vol. 4, no. 4, pp. 1052–1056, 2017. 18

[29] Samuel, "Intake and Exhaust Manifold Design and Tuning - EngineKnowHow," visited on 06/06/2019. [Online]. Available: http://www.engineknowhow.com/the-intake-and-exhaust-systems-and-processes/intake-and-exhaust-manifold-design-and-tuning/ 18

[30] K. JEYOUNG, "A PULSE TURBOCHARGING SYSTEM FOR SMALL SI-ENGINE TO IMPROVE LOW-END TORQUE," Ph.D. dissertation, Technological University of Malaysia, 2019. 19

[31] H. Bettes, "INDUCTION SYSTEM TUNING," visited on 08/06/2019. [Online]. Available: https://performancespecialties.wordpress.com/2011/08/02/induction-system-tuning/ 19

[32] M. Wan, “Intake and Exhaust,” visited on 09/06/2019. [Online]. Available: http://www.autozine.org/technical_school/engine/Intake_exhaust.html 19

[33] University of Misan, “Flow in pipes,” visited on 03/09/2019. [Online]. Available: http://www.uomisan.edu.iq/eng/ar/admin/pdf/26059867395.pdf 23

[34] Samuel, “Valve Design,” visited on 17/09/2019. [Online]. Available: http://www.engineknowhow.com/the-intake-and-exhaust-systems-and-processes/valve-design/ 25

[35] Z. Courts, “Desmo Valves vs. Springs,” visited on 17/09/2019. [Online]. Available: https://www.motorcyclistonline.com/does-ducatis-mechanical-claim-to-fame-live-up-to-hype/ 26

[36] SEAS, “Desmodromic valve system,” visited on 18/09/2019. [Online]. Available: http://www.formula1-dictionary.net/desmodromic.html 26

[37] D. N. Assanis and M. Polishak, “Valve Event Optimization in a Spark-Ignition Engine,” *Journal of Engineering for Gas Turbines and Power*, vol. 112, no. 3, pp. 341–347, 1990. 28, 29

[38] T. W. Asmus, “Valve events and engine operation,” *SAE transactions*, vol. 91, no. 3, pp. 2520–2533, 1982. 28

[39] R. B. R. da COSTA *et al.*, “Experimental methodology and numerical simulation of intake valves discharge coefficients for a single cylinder research engine,” SAE Technical Paper 2015-36-0267, Tech. Rep., 2015. 32, 35

[40] A. F. Bicen *et al.*, “Steady and Unsteady Airflow Through the Intake Valve of a Reciprocating Engine,” *Journal of Fluids Engineering*, vol. 107, no. 3, pp. 413–420, 1985. 32, 37

[41] L. J. Kastner *et al.*, “Poppet inlet valve characteristics and their influence on the induction process,” *Proceedings of the Institution of Mechanical Engineers*, vol. 178, no. 1, pp. 955–975, 1963. 32, 38, 39

[42] D. Oh and C. H. Lee, “Flow coefficient measurements for an engine cylinder head under transient flow conditions with continuous valve lift change,” *International Journal of Engineering and Technology*, vol. 7, no. 3, pp. 1135–1142, 2015. 34, 35, 83, 86

[43] A. Algieri, “An Experimental Analysis of the Fluid Dynamic Efficiency of a Production Spark-Ignition Engine during the Intake and Exhaust Phase,” *ISRN Mechanical Engineering*, vol. 2011, pp. 1–8, 2011. 35, 77, 78

[44] B. Soriano *et al.*, “Steady discharge coefficient in internal combustion engine.” 14th Brazilian Congress of Thermal Sciences and Engineering, 2012. 35, 36, 37

[45] A. Algieri, “Experimental investigation of the fluid dynamic efficiency of a high performance multi-valve internal combustion engine during the intake phase: Influence of valve-valve interference phenomena,” *Thermal Science*, vol. 17, no. 1, pp. 25–34, 2013. 36, 65, 80

[46] K. TANAKA, “Air flow through suction valve of conical seat part 1: Experimental research.” *title Report of Aeronautical Research Institute, Tokyo Imperial University*, vol. 4, no. 50, pp. 259–360, 1929. 37

[47] R. V. Pajkovic and V. S. Petrovic, “SPATIAL FLOW VELOCITY DISTRIBUTION AROUND AN INLET PORT/VALVE ANNULUS,” *THERMAL SCIENCE:*, vol. 12, no. 1, pp. 73–83, 2008. 37, 38

[48] I. Fukutani and E. Watanabe, “Air Flow through Poppet Inlet Valves - Analysis of Static and Dynamic Flow Coefficients,” SAE International, Tech. Rep., 1982. 38, 83

[49] Carfolio, “2002 Toyota Corolla 1.4 VVT-i ,” visited on 18/12/2019. [Online]. Available: https://www.carfolio.com/specifications/models/car/?car=534468 45

[50] Tempsens, “TYPE K THERMOCOUPLE,” visited on 26/12/2019. [Online]. Available: http://www.tempsens.com/pdf/articles/Type_K.pdf 46

[51] Maxim integrated, “MAX6675 Cold-Junction-Compensated K-Thermocoupleto-Digital Converter (0°C to +1024°C),” visited on 17/01/2020. [Online]. Available: https://datasheets.maximintegrated.com/en/ds/MAX6675.pdf 46

[52] H. Xu, “Some critical technical issues on the steady flow testing of cylinder heads,” SAE Technical Paper 2001-01-1308, Tech. Rep., 2001. 47

[53] The-Crankshaft Publishing, “Intake and Exhaust Valves and Mechanisms (Automobile),” visited on 13/01/2020. [Online]. Available: http://what-when-how.com/automobile/intake-and-exhaust-valves-and-mechanisms-automobile/ 62

[54] University of North Carolina, “Introduction to Measurements & Error Analysis,” visited on 18/03/2020. [Online]. Available: https://physics.unc.edu/files/2012/10/uncertainty.pdf 87

Appendix A

Hot-wire MAF sensor specifications

Hot-film air-mass meter, Type HFM 5

Measurement of air-mass throughflow up to 1000 kg/h

Q_m / U

- Compact design.
- Low weight.
- Rapid response.
- Low power input.
- Return-flow detection.

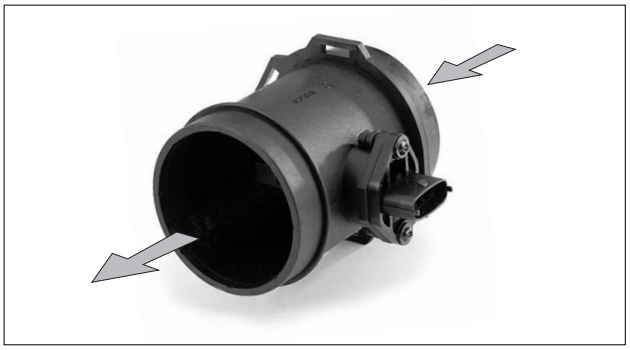

Application
In order to comply with the vehicle emission limits demanded by law, it is necessary to maintain a given air/fuel ratio exactly.
This requires sensors which precisely register the actual air-mass flow and output a corresponding electrical signal to the open and closed-loop control electronics.

Design
The micromechanical sensor element is located in the plug-in sensor's flow passage. This plug-in sensor is suitable for incorporating in the air filter or, using a measurement venturi, in the air-intake passages. There are different sizes of measurement venturi available depending upon the air throughflow. The micromechanical measuring system uses a hybrid circuit, and by evaluating the measuring data is able to detect when return flow takes place during air-flow pulsation.

Operating principle
The heated sensor element in the air-mass meter dissipates heat to the incoming air. The higher the air flow, the more heat is dissipated. The resulting temperature differential is a measure for the air mass flowing past the sensor.
An electronic hybrid circuit evaluates this measuring data so that the air-flow quantity can be measured precisely, and its direction of flow.
Only part of the air-mass flow is registered by the sensor element. The total air mass flowing through the measuring tube is determined by means of calibration, known as the characteristic-curve definition.

Technical data / range

Nominal supply voltage U_N	14 V
Supply-voltage range U_V	8...17 V
Output voltage U_A	0...5 V
Input current I_V	< 0.1 A
Permissible vibration acceleration	≤ 150 ms^{-2}
Time constant τ_{63} [1]	≤ 15 ms
Time constant τ_Δ [2]	≤ 30 ms
Temperature range	–40...+120 °C [3]

Part number	**0 280 217 123**	**0 280 218 019**	**0 280 217 531**	**0 280 218 008**	**0 281 002 421**
Measuring range Q_m	8...370 kg/h	10...480 kg/h	12...640 kg/h	12...850 kg/h	15...1000 kg/h
Accuracy [4]	≤ 3%	≤ 3%	≤ 3%	≤ 3%	≤ 3%
Fitting length L_E	22 mm	22 mm	22 mm	16 mm	22 mm
Fitting length L_A	20 mm	20 mm	20 mm	16 mm	20 mm
Installation length L	96 mm	96 mm	130 mm	100 mm	130 mm
Connection diam. D	60 mm	70 mm	80 mm	86/84 mm [6]	92 mm
Venturi ID	50 mm	62 mm	71 mm	78 mm	82 mm
Pressure drop at nominal air mass [5]	< 20 hPa	< 15 hPa	< 15 hPa	< 15 hPa	< 15 hPa
Temperature sensor	Yes	Yes	Yes	No	Yes
Version	1	2	3	4	5

[1] In case of sudden increase of the air-mass flow from 10 kg · h^{-1} auf 0,7 $Q_{m\,nominal}$, time required to reach 63% of the final value of the air-mass signal.
[2] Period of time in case of a throughflow jump of the air mass | $\Delta\, m/m$ | ≤ 5%.
[3] For a short period up to +130 °C.
[4] $|\Delta Q_m/Q_m|$: The measurement deviation ΔQ_m from the exact value, referred to the measured value Q_m.
[5] Measured between input and output
[6] Inflow/outflow end

Accessories for connector

Plug housing	Contact pins	Individual gaskets	For conductor cross-section
1 928 403 836	**1 987 280 103**	**1 987 280 106**	0.5...1 mm^2
	1 987 280 105	**1 987 280 107**	1.5...2.5 mm^2

Note: Each 5-pole plug requires 1 plug housing, 5 contact pins, and 5 individual gaskets.
For automotive applications, original AMP crimping tools must be used.

Application
In internal-combustion engines, this sensor is used for measuring the air-mass flow so that the injected fuel quantity can be adapted to the presently required power, to the air pressure, and to the air temperature.

Explanation of symbols

Q_m	Air-mass flow rate
ΔQ_m	Absolute accuracy
$\Delta Q_m/Q_m$	Relative accuracy
τ_Δ	Time until measuring error is ≤ 5%
τ_{63}	Time until measured-value change 63%

Function diagram with connector-pin assignment.
1 Additional temperature sensor ϑ_u (not on version 4, Part number 0 280 218 008),
2 Supply voltage U_V, **3** Signal ground, **4** Reference voltage 5 V, **5** Measurement signal U_A.
ϑ Temperature-dependence of the resistor, R_H Heater resistor, U_K Constant voltage

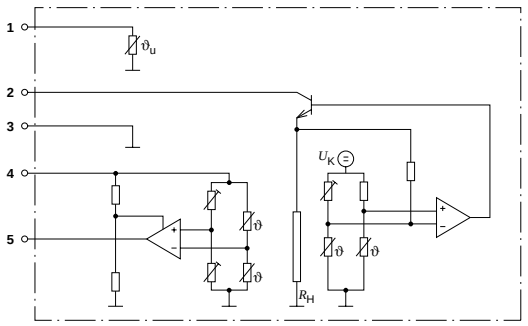

HFM 5 plug-in sensor design.
1 Measuring-passage cover, **2** Sensor,
3 Mounting plate, **4** Hybrid-circuit cover,
5 Hybrid, **6** Plug-in sensor, **7** O-ring,
8 Auxiliary temperature sensor.

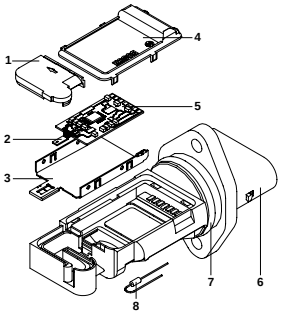

Output voltage U_A = f(Q_m) of the air-mass meter

Part number	0 280 217 123	0 280 218 019	0 280 217 531	0 280 218 008	0 280 002 421
Characteristic curve	1	2	3	4	5
Q_m/kg/h	U_A/V	U_A/V	U_A/V	U_A/V	U_A/V
8	1.4837	1.2390	–	–	–
10	1.5819	1.3644	1.2695	–	–
15	1.7898	1.5241	1.4060	1.3395	1.2315
30	2.2739	1.8748	1.7100	1.6251	1.4758
60	2.8868	2.3710	2.1563	2.0109	1.8310
120	3.6255	2.9998	2.7522	2.5564	2.3074
250	4.4727	3.7494	3.5070	3.2655	2.9212
370	4.9406	4.1695	3.9393	3.6717	3.2874
480	–	4.4578	4.2349	3.9490	3.5461
640	–	–	4.5669	4.2600	3.8432
850	–	–	–	4.5727	4.1499
1000	–	–	–	–	4.3312

Air-mass meter output voltage.

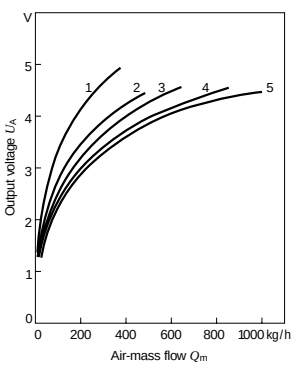

Temperature-dependence R_ϑ = f(ϑ) of the temperature sensor

Temperature ϑ	°C	–40	–30	–20	–10	±0	10	20	30	40
Resistance R_ϑ	kΩ	39.26	22.96	13.85	8.609	5.499	3.604	2.420	1.662	1.166
Temperature ϑ	°C	50	60	70	80	90	100	110	120	130
Resistance R_ϑ	Ω	835	609	452	340	261	202	159	127	102

Temperature-resistance diagram of the temperature sensor.

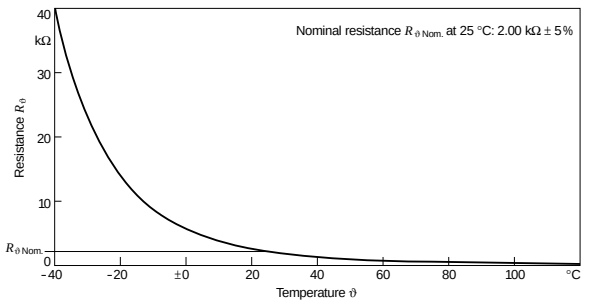

Dimensions overview of the HFM 5.
1 Plug-in sensor, **2** Throughflow direction,
3 Measurement venturi.

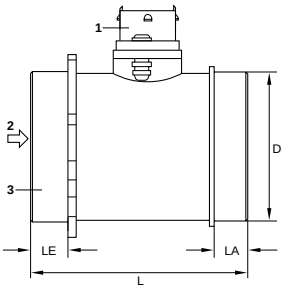

A.1 MAF sensor calibration curve

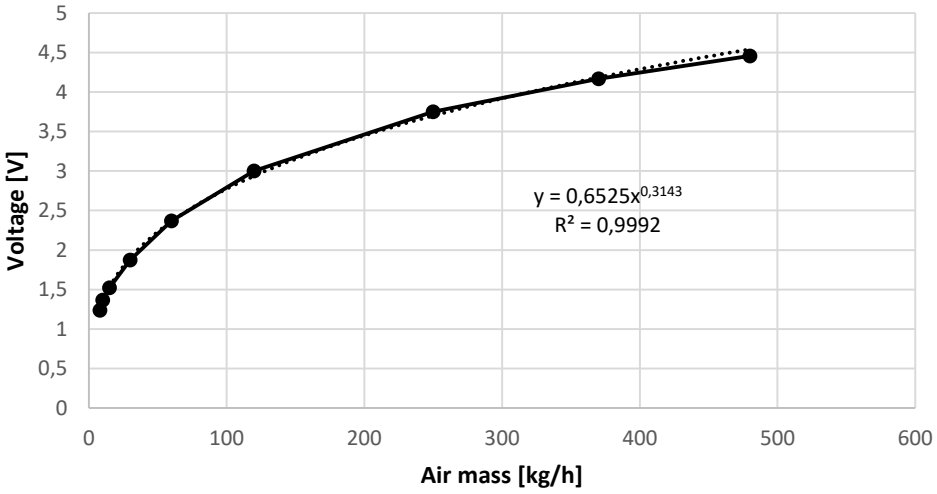

Figure A.1: MAF calibration curve.

Appendix B

MAP sensor data

B.1 Intake MAP sensor calibration graph

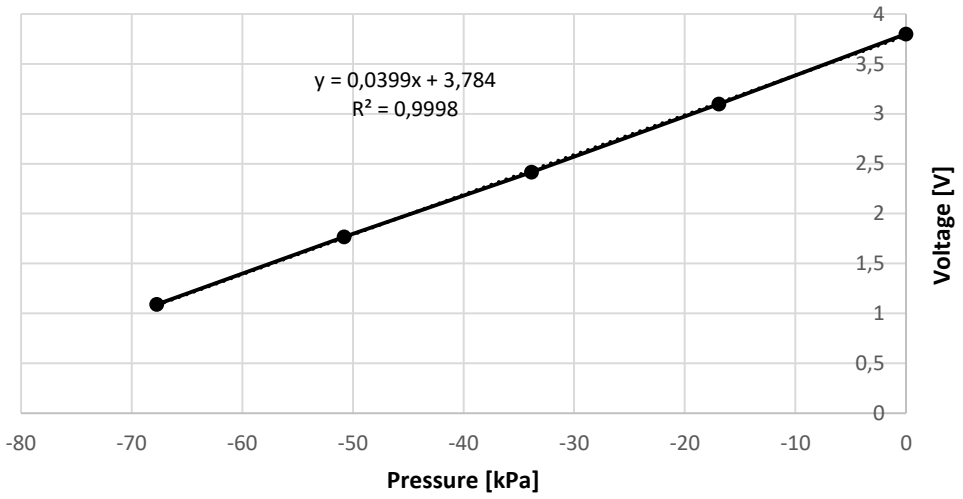

Figure B.1: Inlet MAP sensor calibration line.

B.2 Cylinder MAP sensor calibration graph

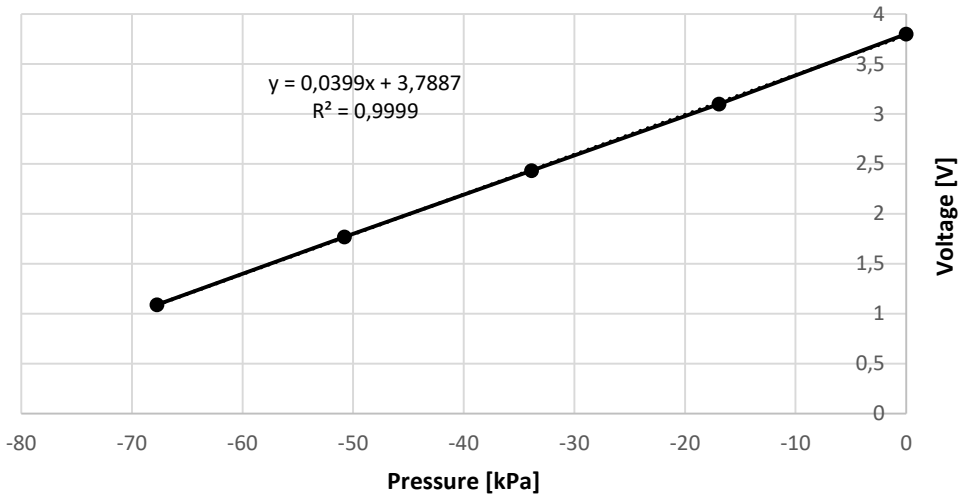

Figure B.2: Cylinder MAP sensor calibration line.

Appendix C

Stepper motor and driver data

C.1 Nema 23 specifications

Table C.1: Stepper motor details

Part number	23HS9430
Phase	2 Phase
Step angle [°]	1.8
Maximum current [A]	3
Inductance [mH/phase]	6.8
Holding torque [Nm]	2.8
Detent torque[Nm]	0.12

C.2 TB6600 v1.2 stepper motor driver specifications

Table C.2: Controller technical data.

Supply voltage [V]	8 to 50
Max output current [A]	4.5
Microstep	1,2,8,16

Appendix D

Custom power supply details

D.1 Pc power supply specifications

Table D.1: PC power supply colour code and specifications

Outputs	Colour	Current Output [A]	Frequency [Hz]	Total output [W]
+3.3V	Orange	24	50/60	350
+5V	Red	35		
-5V	White	0.5		
+12V	Yellow	12		
-12V	Blue	0.8		
PS-ON	Green	-		

D.2 Buck converter data

Table D.2: Buck converter specifications

Input Voltage [V]	6-40
Output Voltage [V]	1.2-36
Output max current [A]	20
Power [W]	300

D.3 Wiring scheme

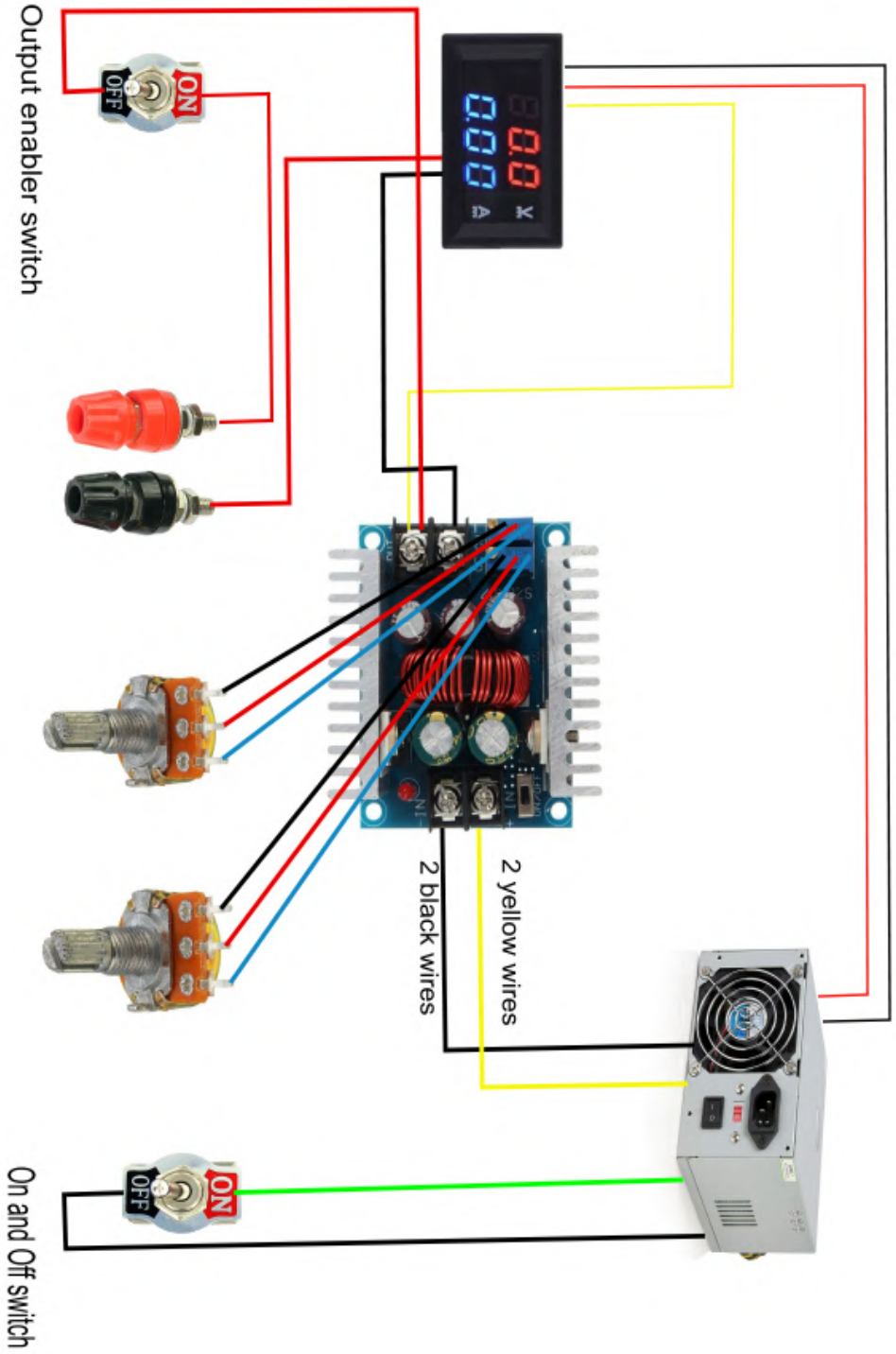

Figure D.1: Variable output wiring scheme of the custom power supply made in Inkscape.

Appendix E

3-view drawings

E.1 Shaft support

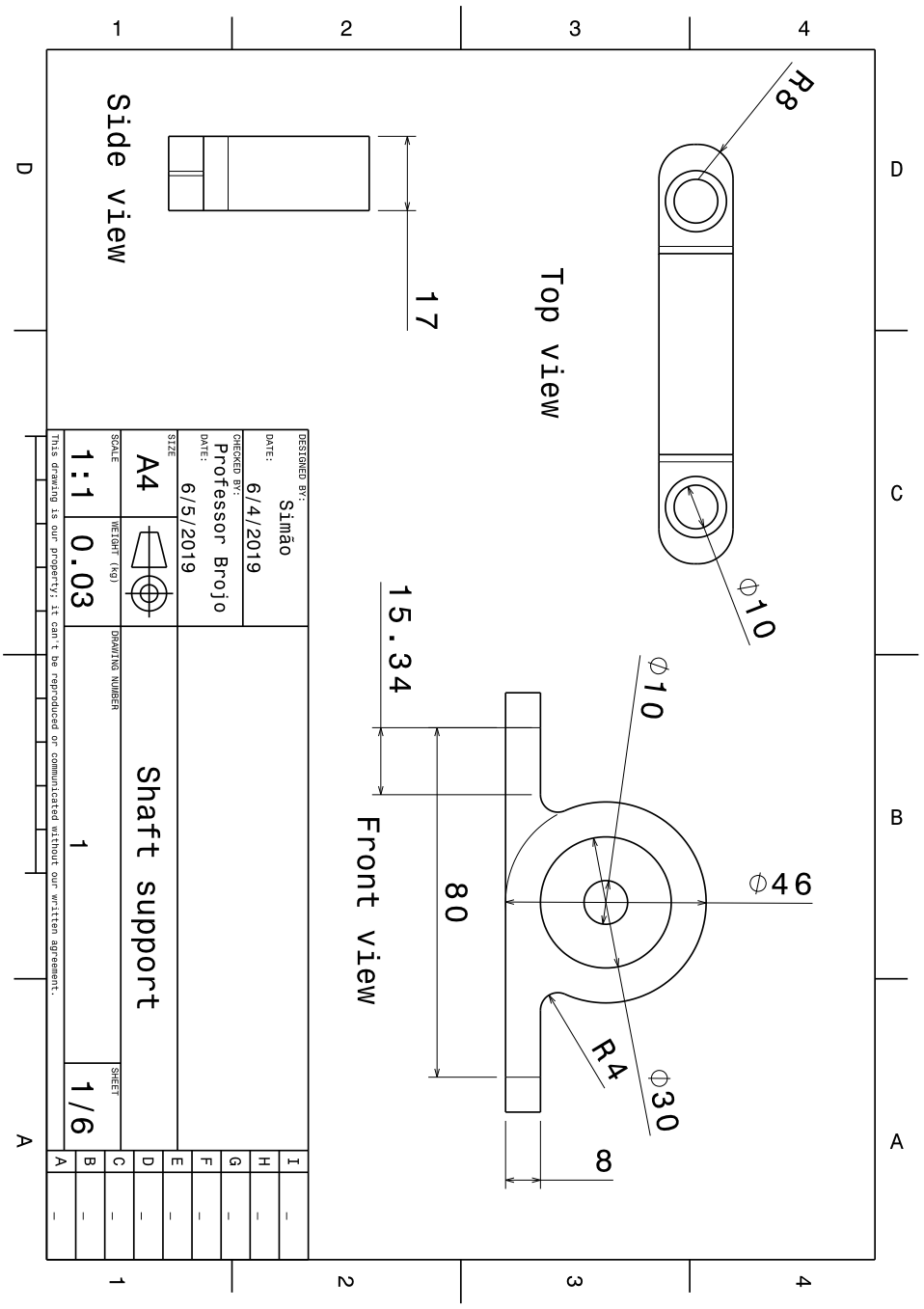

Figure E.1: Shaft support dimensions together with the perspectives.

E.2 Linkage between MAF sensor and throttle holder

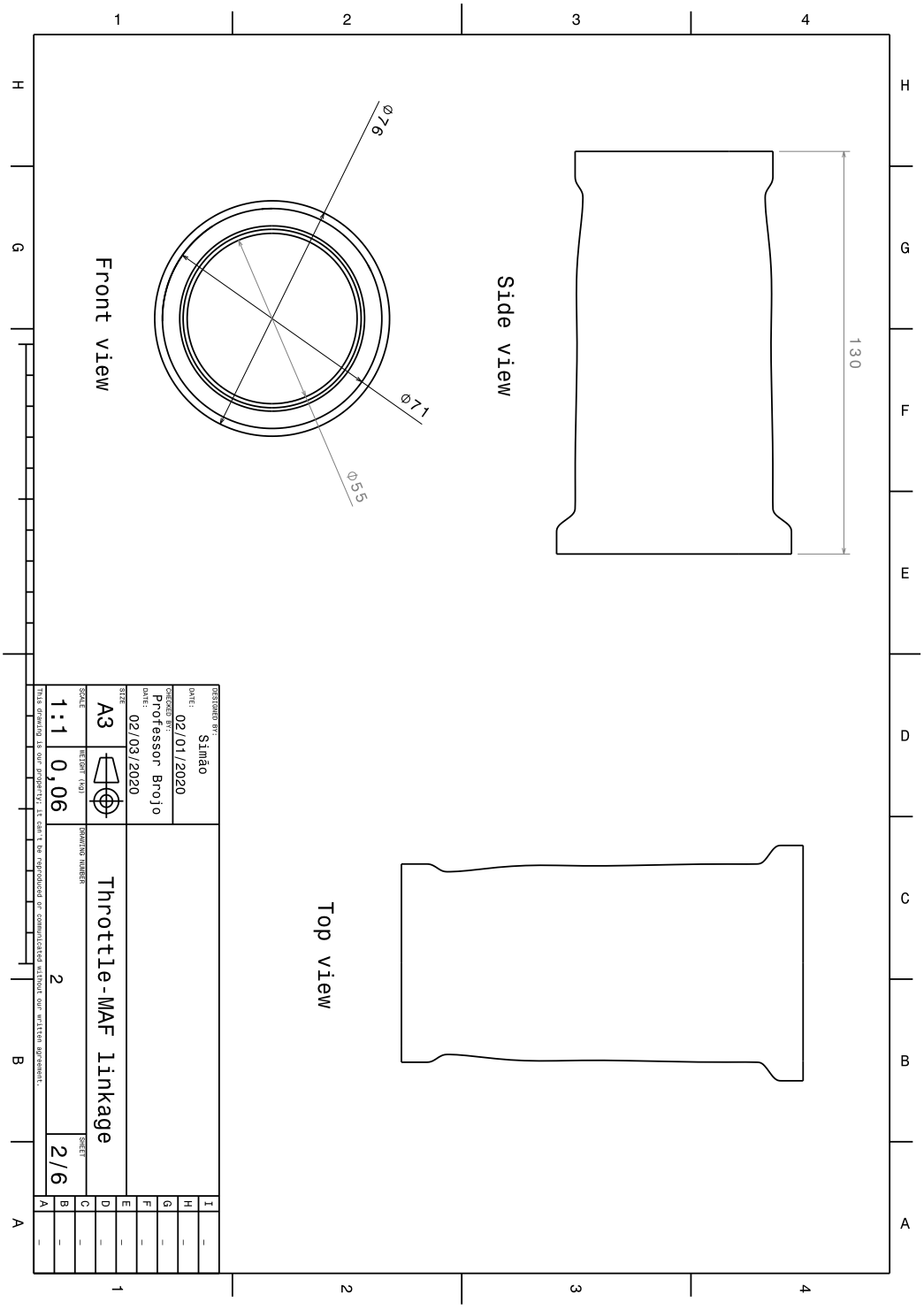

Figure E.2: Connecting piece dimensions and different perspectives.

E.3 Throttle plate holder

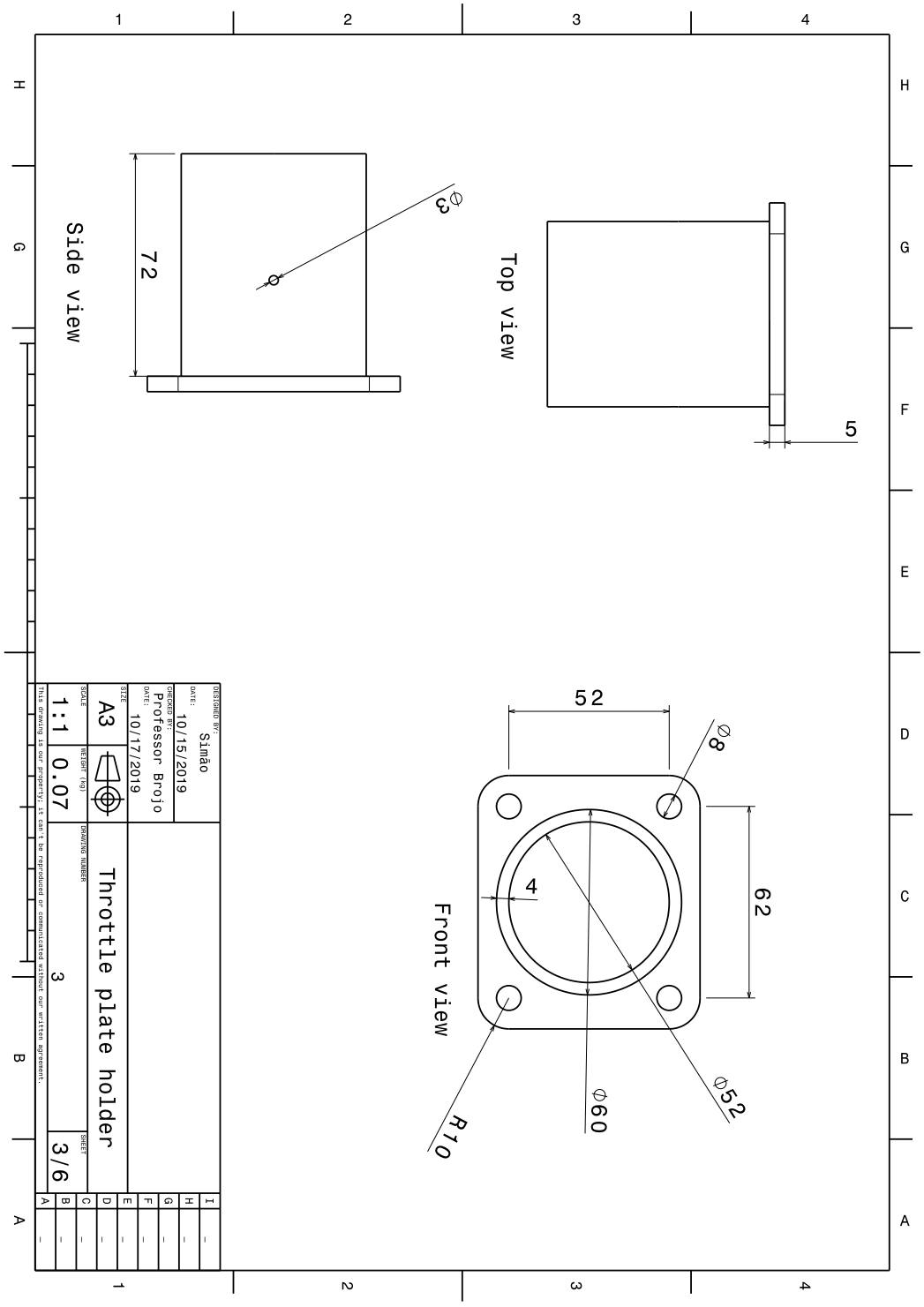

Figure E.3: Throttle plate holder dimensions and views.

E.4 Throttle plate

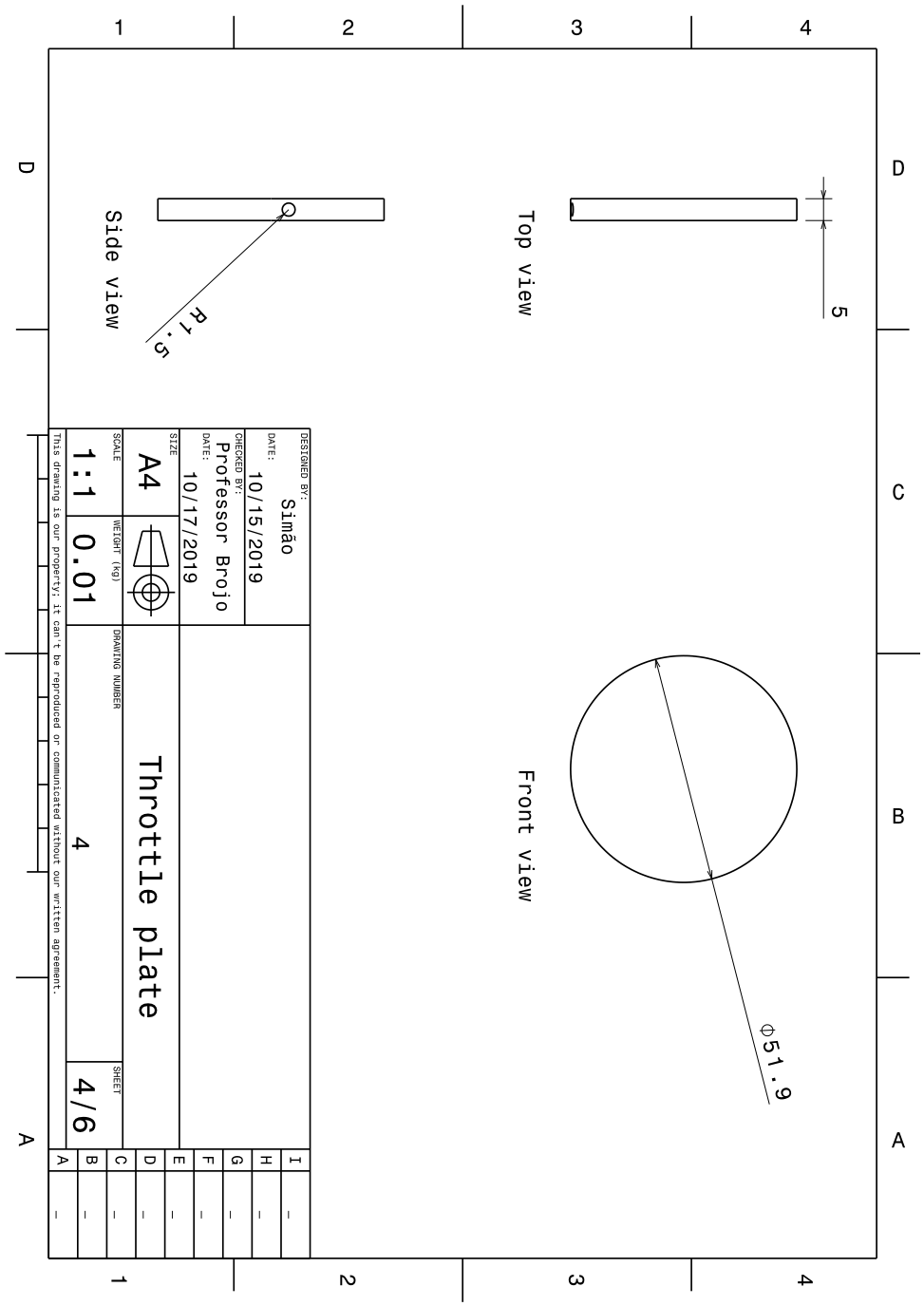

Figure E.4: Throttle plate dimensions and different views.

E.5 Stepper motor support

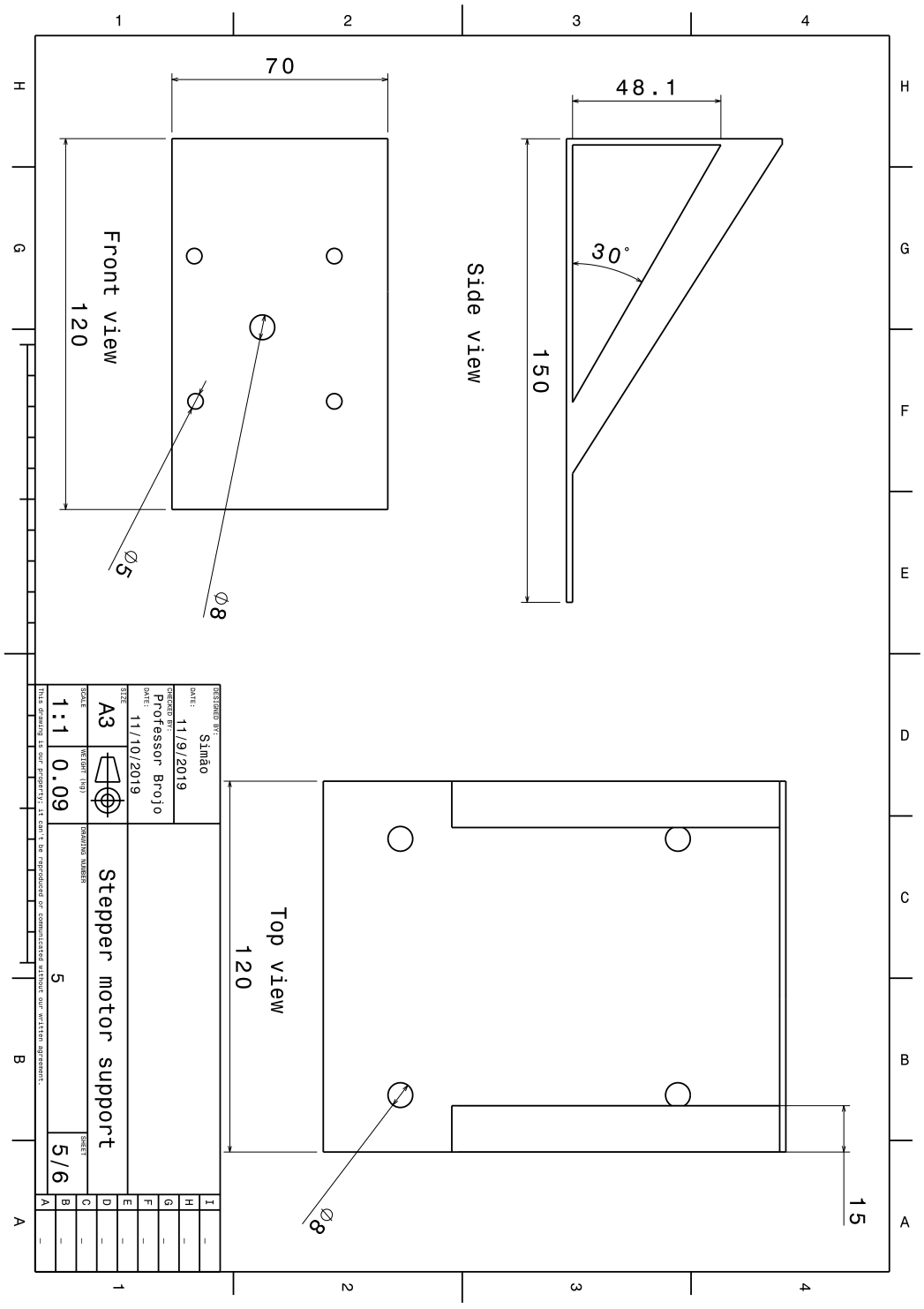

Figure E.5: Nema 23 support dimensions together with the perspectives.

E.6 Test bench final design

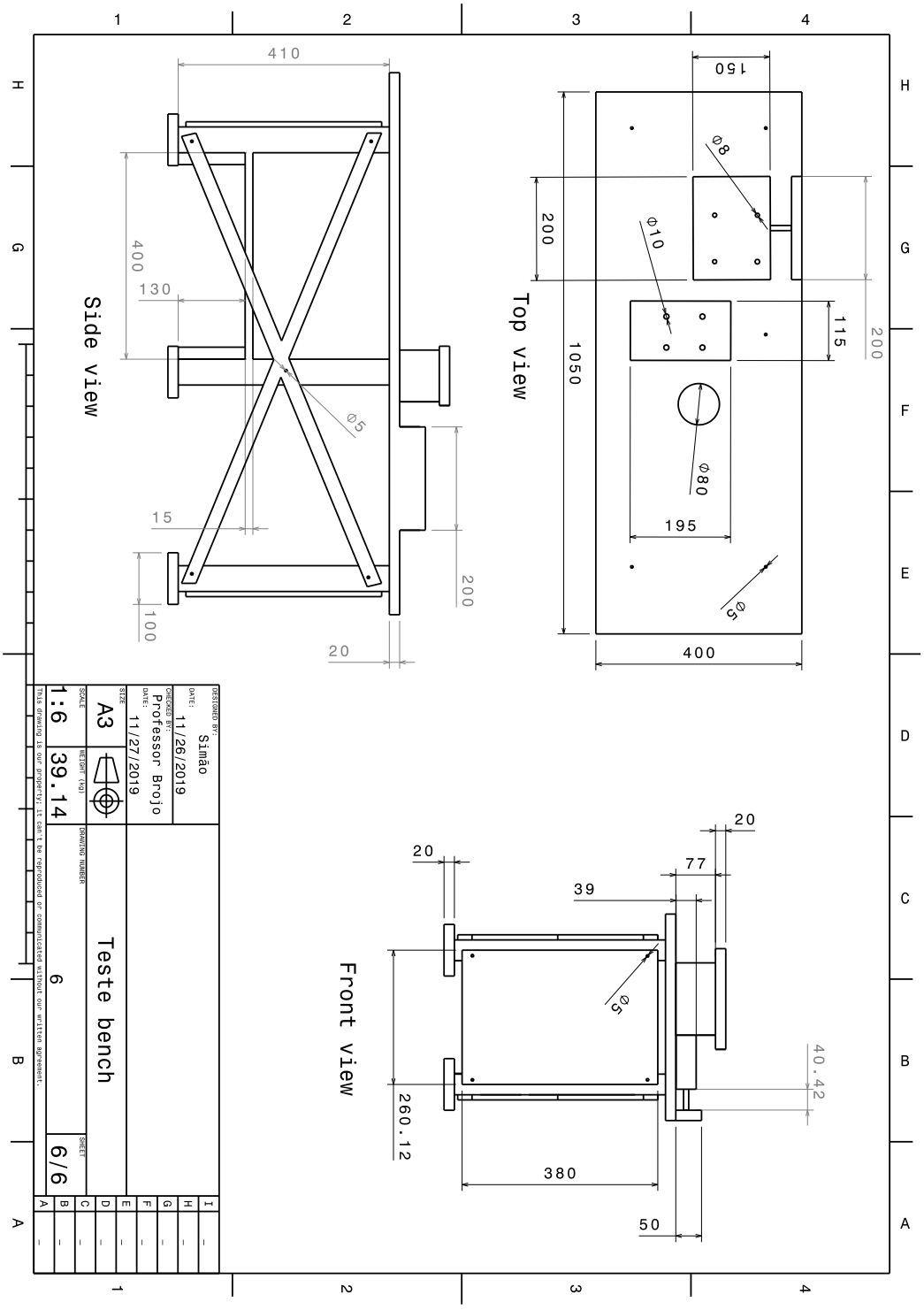

Figure E.6: Test bench dimensions and different views.

Appendix F

Arduino codes

F.1 Sensors readings

```
#include <AccelStepper.h>
#include "max6675.h"

// Thermocouple variables

int soPin = 11;// SO=Serial Out
int csPin = 10;// CS = chip select CS pin
int sckPin = 6;// SCK = Serial Clock pin

MAX6675 thermocouple123(sckPin, csPin, soPin);

//  Low-pass filter variables

float air_filter;
float K = 1;
float alfa = 3; // smoothing
float beta = 1;
float T = 1;   // response time
float air_filter_minus_1 = 0;
float air_mass_minus_1 = 0;
#define ledPin 13

void setup() {
   pinMode(ledPin,OUTPUT);
   Serial.begin(9600);
//   stepper.setMaxSpeed(50);
}


 // MAPS (1 & 2) AND MAF(3)
void loop(){

   int sensorVal_1= analogRead(A1);
   int sensorVal_2= analogRead(A2);
   int sensorVal_3= analogRead(A3);


     // sensor value to voltage conversion
    float voltage_1 = sensorVal_1 *(5.0/1023.0);
    float voltage_2 = sensorVal_2 *(5.0/1023.0);
    float voltage_3 = sensorVal_3 *(5.0/1023.0);
```

```
// voltage to pressure conversion

     float pressure_kpa_5= (voltage_1 - 3.7840)/(0.0399);
     float pressure_kpa_2= (voltage_2 - 3.7887)/(0.0399);
     float pressure_kpa_3= 94.1 + pressure_kpa_5; // Atmospheric pressure in
Covilha according to a barometer
     float pressure_kpa_4= 94.1 + pressure_kpa_2; // Atmospheric pressure in
Covilha according to a barometer


// Voltage to air mass conversion
float  air_mass_1=  pow((voltage_3)/0.6525,1/.3143);

// Low-pass filter applied to the air mass
     air_filter =
1/(2*alfa+beta*T)*((2*alfa-beta*T)*air_filter_minus_1+K*T*air_mass_1+K*T*air_m
ass_minus_1);
     air_filter_minus_1 = air_filter;
     air_mass_minus_1 = air_mass_1;


// Print data in Serial Monitor

Serial.print(thermocouple123.readCelsius());
Serial.print("\t");
Serial.print(pressure_kpa_3);
Serial.print("\t");
Serial.print(pressure_kpa_4);
Serial.print("\t");
Serial.print(air_mass_1);
Serial.print("\t");
Serial.println(air_filter);

   delay(100);   // For dynamic tests delay = 5

}
```

F.2 Stepper motor static conditions

```
#include <AccelStepper.h>

// Stepper motor parameters

#define dirPin 9
#define stepPin 5
#define motorInterfaceType 1
#define ledPin 13

AccelStepper stepper = AccelStepper(motorInterfaceType, stepPin, dirPin);

void setup() {
  Serial.begin(9600);
  stepper.setMaxSpeed(50); // Set stepper motor maximum speed
}

void loop() {
  delay(3000);

  digitalWrite(ledPin,LOW);   // reference to IVO
  motor(120,1,2222,50,10);
  digitalWrite(ledPin,HIGH);
  stepper.runToPosition();
  delay(3000);

  digitalWrite(ledPin,LOW);
  motor(2,1,240,50,10);      // Lv =0.5mm
  digitalWrite(ledPin,HIGH);
  stepper.runToPosition();
  delay(5000);

  digitalWrite(ledPin,LOW);
  motor(2,1,89,50,10);
  digitalWrite(ledPin,HIGH);  // Lv =1mm
  stepper.runToPosition();
  delay(5000);

  digitalWrite(ledPin,LOW);
  motor(2,1,41,40,10);
  digitalWrite(ledPin,HIGH);    // Lv =1.5mm
  stepper.runToPosition();
  delay(5000);
```

```
digitalWrite(ledPin,LOW);
motor(2,1,46,40,10);
digitalWrite(ledPin,HIGH);   // Lv =2mm
stepper.runToPosition();
delay(5000);

digitalWrite(ledPin,LOW);
motor(2,1,46,40,10);
digitalWrite(ledPin,HIGH);   // Lv =2.5mm
stepper.runToPosition();
delay(5000);

digitalWrite(ledPin,LOW);
motor(2,1,46,40,10);
digitalWrite(ledPin,HIGH);     // Lv =3mm
stepper.runToPosition();
delay(5000);

digitalWrite(ledPin,LOW);
motor(2,1,85,40,10);
digitalWrite(ledPin,HIGH);     // Lv =4mm
stepper.runToPosition();
delay(5000);

digitalWrite(ledPin,LOW);
motor(2,1,96,40,10);
digitalWrite(ledPin,HIGH);     // Lv =5mm
stepper.runToPosition();
delay(5000);

digitalWrite(ledPin,LOW);
motor(2,1,96,40,10);
digitalWrite(ledPin,HIGH);     // Lv =6mm
stepper.runToPosition();
delay(5000);

digitalWrite(ledPin,LOW);
motor(2,1,115,40,10);
digitalWrite(ledPin,HIGH);     // Lv =7mm
stepper.runToPosition();
delay(5000);
```

```
  digitalWrite(ledPin,LOW);
  motor(2,1,169,40,10);
  digitalWrite(ledPin,HIGH);     // Lv =8mm
  stepper.runToPosition();
  delay(5000);

  digitalWrite(ledPin,LOW);
  motor(2,1,169,40,10);
  digitalWrite(ledPin,HIGH);     // Lv =8.4mm
  stepper.runToPosition();
  delay(5000);

  digitalWrite(ledPin,LOW);
  motor(120,1,2939,50,10);
  digitalWrite(ledPin,HIGH);  // IVC until reference
  stepper.runToPosition();
  delay(10000);

}

// Stepper motor function


void motor (int spd, int diret,int steps,int fast,int timee){
 stepper.setSpeed(spd*diret);//RPM
 stepper.setAcceleration(fast);
 // Run to target position with set speed and acceleration/deceleration:

  stepper.move(steps*diret);
  delay(timee);  //time without arduino led turns on
}
```

F.3 Stepper motor dynamic conditions

```
#include <Stepper.h>

// Stepper motor parameters

#define STEPS 200   // steps required for one revolution without any
microstepping

Stepper  stepper(STEPS,5,9);

int val = 0;

void setup() {
   Serial.begin(9600);
  stepper.setSpeed(320);  // 80 = 5rpm , 160 = 10rpm , 240 = 15rpm and 320 =
20rpm  // Set the speed of the motor
}

void loop() {

  if (Serial.available()>0)
  {
    val = Serial.parseInt(); // reads the input value in the serial monitor
    stepper.step(val); // Turns the motor the number of steps inserted in the
serial monitor at the defined speed
    Serial.println(val);
  }

}
```

Appendix G

Python data code

File - C:\Users\simao\PycharmProjects\Results\Results.py

```
 1 import pandas as pd
 2 import numpy as np
 3 import xlsxwriter
 4
 5 # Method to determine the camshaft angle step and valve
   lift step
 6
 7 # Amount of results
 8
 9 # Camshaft angle
10 n_1 = 92
11 n_2 = 47
12 n_3 = 32
13 n_4 = 25
14
15 # Valve lifts
16 n_5 = 46
17 n_6 = 23
18 n_7 = 16
19 n_8 = 12
20
21 # IVO Time
22 a_1 = 135
23
24 # IVC Time
25 b_1 = 255
26
27 # Minimum valve lift measured
28 a_2 = 0.0005
29
30 # Maximum valve lift measured
31 b_2 = 0.0084
32
33 #  Camshaft angle step calculation
34 h_1 = float(b_1 - a_1) / n_1
35 h_2 = float(b_1 - a_1) / n_2
36 h_3 = float(b_1 - a_1) / n_3
37 h_4 = float(b_1 - a_1) / n_4
38
39 h_5 = float(b_2 - a_2) / n_5
40 h_6 = float(b_2 - a_2) / n_6
41 h_7 = float(b_2 - a_2) / n_7
42 h_8 = float(b_2 - a_2) / n_8
43
44
45
```

```
46 alphas_list_1 = []  # camshaft angles 5rpm
47 alphas_list_2 = []  # camshaft angles 10rpm
48 alphas_list_3 = []  # camshaft angles 15rpm
49 alphas_list_4 = []  # camshaft angles 20rpm
50
51 valve_lift_list_1 = [] # valve lifts 5rpm
52 valve_lift_list_2 = [] # valve lifts 10rpm
53 valve_lift_list_3 = [] # valve lifts 15rpm
54 valve_lift_list_4 = [] # valve lifts 20rpm
55
56 for k in range(0,93):
57     u_1=a_1+k*h_1
58     alphas_list_1.append(u_1)
59
60 for k in range(0,48):
61     u_2=a_1+k*h_2
62     alphas_list_2.append(u_2)
63
64 for k in range(0,33):
65     u_3=a_1+k*h_3
66     alphas_list_3.append(u_3)
67
68 for k in range(0,26):
69     u_4=a_1+k*h_4
70     alphas_list_4.append(u_4)
71
72 #  Valve lift step calculation
73
74 for k in range(0,47):
75     u_5=a_2+k*h_5
76     valve_lift_list_1.append(u_5)
77
78 for k in range(0,24):
79     u_6=a_2+k*h_6
80     valve_lift_list_2.append(u_6)
81
82 for k in range(0,17):
83     u_7=a_2+k*h_7
84     valve_lift_list_3.append(u_7)
85
86 for k in range(0,13):
87     u_8=a_2+k*h_8
88     valve_lift_list_4.append(u_8)
89
90 #convert the lists to arrays
91
```

File - C:\Users\simao\PycharmProjects\Results\Results.py

```
 92 alphas_array_1 = np.asarray(alphas_list_1)
 93 alphas_array_2 = np.asarray(alphas_list_2)
 94 alphas_array_3 = np.asarray(alphas_list_3)
 95 alphas_array_4 = np.asarray(alphas_list_4)
 96 valve_lift_array_1 = np.asarray(valve_lift_list_1)
 97 valve_lift_array_2 = np.asarray(valve_lift_list_2)
 98 valve_lift_array_3 = np.asarray(valve_lift_list_3)
 99 valve_lift_array_4 = np.asarray(valve_lift_list_4)
100
101 # Exporting to excel the camshaft angles and valve lifts
    steps previously determined
102
103 OutWorkbook = xlsxwriter.Workbook("Outdata.xlsx")
104 OutSheet = OutWorkbook.add_worksheet()
105
106 OutSheet.write("A1", "Camshaft angles for 5 rpm")
107 OutSheet.write("C1", "Camshaft angles for 10 rpm")
108 OutSheet.write("E1", "Camshaft angles for 15 rpm")
109 OutSheet.write("G1", "Camshaft angles for 20 rpm")
110
111 OutSheet.write("I1", "Valve lifts for 5 rpm")
112 OutSheet.write("K1", "Valve lifts for 10 rpm")
113 OutSheet.write("M1", "Valve lifts for 15 rpm")
114 OutSheet.write("O1", "Valve lifts for 20 rpm")
115
116 for item in range(len(alphas_array_1)):
117     OutSheet.write(item + 1, 0, alphas_array_1[item])
118
119 for item in range(len(alphas_array_2)):
120     OutSheet.write(item + 1, 2, alphas_array_2[item])
121
122 for item in range(len(alphas_array_3)):
123     OutSheet.write(item + 1, 4, alphas_array_3[item])
124
125 for item in range(len(alphas_array_4)):
126     OutSheet.write(item + 1, 6, alphas_array_4[item])
127
128
129 for item in range(len(valve_lift_array_1)):
130     OutSheet.write(item + 1, 8, valve_lift_array_1[item])
131
132 for item in range(len(valve_lift_array_2)):
133     OutSheet.write(item + 1, 10, valve_lift_array_2[item])
134
135 for item in range(len(valve_lift_array_3)):
136     OutSheet.write(item + 1, 12, valve_lift_array_3[item])
```

```
137
138 for item in range(len(valve_lift_array_4)):
139     OutSheet.write(item + 1, 14, valve_lift_array_4[item])
140
141 OutWorkbook.close()
142
143 #Selection of the test condition
144
145 print('Choose the test condition ?')
146 begin = int(input())
147
148 if begin == 1:
149     init_1 = pd.read_excel('data_dynamic_standard.xlsx')
150     # convert xlsx format into csv
151     init_1.to_csv('data_1.csv')
152     start_1 = pd.read_csv('data_1.csv')
153     data_1 = np.array(start_1)
154
155 else:
156     if begin == 2:
157         init_2 = pd.read_excel('data_dynamic_onevalve.xlsx
    ')
158         init_2.to_csv('data_2.csv')
159         start_2 = pd.read_csv('data_2.csv')
160         data_1 = np.array(start_2)
161
162 # rpm selection
163 print('which set of rpm?')
164 begin_2 = int(input())
165
166 if begin_2 == 1:
167     # 5rpm
168     Cd_1 = data_1[2:95, 1]
169     Cd_2 = data_1[2:95, 4]
170     Cd_3 = data_1[2:95, 7]
171     Cd_4 = data_1[2:95, 10]
172     Cd_5 = data_1[2:95, 13]
173
174
175     # 20rpm
176     Cd_6 = data_1[2:28, 16]
177     Cd_7 = data_1[2:28, 19]
178     Cd_8 = data_1[2:28, 22]
179     Cd_9 = data_1[2:28, 25]
180     Cd_10 = data_1[2:28, 28]
181
```

```
182
183     # 5rpm
184     Cf_1 = data_1[2:95, 2]
185     Cf_2 = data_1[2:95, 5]
186     Cf_3 = data_1[2:95, 8]
187     Cf_4 = data_1[2:95, 11]
188     Cf_5 = data_1[2:95, 14]
189
190     # 20rpm
191     Cf_6 = data_1[2:28, 17]
192     Cf_7 = data_1[2:28, 20]
193     Cf_8 = data_1[2:28, 23]
194     Cf_9 = data_1[2:28, 26]
195     Cf_10 = data_1[2:28, 29]
196
197 else:
198     if begin_2 == 2:
199         # 10rpm
200         Cd_1 = data_1[2:50, 31]
201         Cd_2 = data_1[2:50, 34]
202         Cd_3 = data_1[2:50, 37]
203         Cd_4 = data_1[2:50, 40]
204         Cd_5 = data_1[2:50, 43]
205
206         # 15rpm
207         Cd_6 = data_1[2:35, 46]
208         Cd_7 = data_1[2:35, 49]
209         Cd_8 = data_1[2:35, 52]
210         Cd_9 = data_1[2:35, 55]
211         Cd_10 = data_1[2:35, 58]
212
213         # 10rpm
214         Cf_1 = data_1[2:50, 32]
215         Cf_2 = data_1[2:50, 35]
216         Cf_3 = data_1[2:50, 38]
217         Cf_4 = data_1[2:50, 41]
218         Cf_5 = data_1[2:50, 44]
219
220         # 15rpm
221         Cf_6 = data_1[2:35, 47]
222         Cf_7 = data_1[2:35, 50]
223         Cf_8 = data_1[2:35, 53]
224         Cf_9 = data_1[2:35, 56]
225         Cf_10 = data_1[2:35, 59]
226
227     #Convert from list to array
```

```
228
229 Cd_1_array= np.array(Cd_1)
230 Cd_2_array = np.array(Cd_2)
231 Cd_3_array = np.array(Cd_3)   # 5 ou 10
232 Cd_4_array = np.array(Cd_4)
233 Cd_5_array = np.array(Cd_5)
234
235 Cd_6_array = np.array(Cd_6)
236 Cd_7_array = np.array(Cd_7)     #15 ou 20
237 Cd_8_array = np.array(Cd_8)
238 Cd_9_array = np.array(Cd_9)
239 Cd_10_array = np.array(Cd_10)
240
241 Cf_1_array = np.array(Cf_1)
242 Cf_2_array = np.array(Cf_2)
243 Cf_3_array = np.array(Cf_3)    # 5 ou 10
244 Cf_4_array = np.array(Cf_4)
245 Cf_5_array = np.array(Cf_5)
246
247 Cf_6_array = np.array(Cf_6)
248 Cf_7_array = np.array(Cf_7)    # 15 ou 20
249 Cf_8_array = np.array(Cf_8)
250 Cf_9_array = np.array(Cf_9)
251 Cf_10_array = np.array(Cf_10)
252
253 # Approximating technique (Trapezoidal Rule)
254
255 s_30_1rpmset_cd = 0
256 s_50_1rpmset_cd = 0
257 s_70_1rpmset_cd = 0
258 s_90_1rpmset_cd = 0
259 s_NTP_1rpmset_cd = 0
260
261 s_30_1rpmset_cf = 0
262 s_50_1rpmset_cf = 0
263 s_70_1rpmset_cf = 0
264 s_90_1rpmset_cf = 0
265 s_NTP_1rpmset_cf = 0
266
267
268
269 s_30_2rpmset_cd = 0
270 s_50_2rpmset_cd = 0
271 s_70_2rpmset_cd = 0
272 s_90_2rpmset_cd = 0
273 s_NTP_2rpmset_cd = 0
```

```
274
275 s_30_2rpmset_cf = 0
276 s_50_2rpmset_cf = 0
277 s_70_2rpmset_cf = 0
278 s_90_2rpmset_cf = 0
279 s_NTP_2rpmset_cf = 0
280
281 # Selection of the camshaft angle array and the associated
     n (number of subintervals)
282
283
284 if begin_2 == 1:
285     N_1set = n_1
286     N_2set = n_4
287     alphas_1set = alphas_array_1
288     alphas_2set = alphas_array_4
289
290 else:
291     if begin_2 == 2:
292         N_1set = n_2
293         N_2set = n_3
294         alphas_1set = alphas_array_2
295         alphas_2set = alphas_array_3
296
297
298 # Discharge and flow coefficients determination taking
    into account the camshaft angle
299
300
301 # first rpm set
302
303 for i in range(0, N_1set):
304     s_30_1rpmset_cd += (alphas_1set[i + 1] - alphas_1set[i
    ]) * (Cd_1_array[i + 1]+ Cd_1_array[i]) * 1 / 2
305     s_50_1rpmset_cd += (alphas_1set[i + 1] - alphas_1set[i
    ]) * (Cd_2_array[i + 1] + Cd_2_array[i]) * 1 / 2
306     s_70_1rpmset_cd += (alphas_1set[i + 1] - alphas_1set[i
    ]) * (Cd_3_array[i + 1] + Cd_3_array[i]) * 1 / 2
307     s_90_1rpmset_cd += (alphas_1set[i + 1] - alphas_1set[i
    ]) * (Cd_4_array[i + 1] + Cd_4_array[i]) * 1 / 2
308     s_NTP_1rpmset_cd += (alphas_1set[i + 1] - alphas_1set[
    i]) * (Cd_5_array[i + 1] + Cd_5_array[i]) * 1 / 2
309
310
311
312     s_30_1rpmset_cf += (alphas_1set[i + 1] - alphas_1set[i
```

```
312 ]) * (Cf_1_array[i + 1] + Cf_1_array[i]) * 1 / 2
313     s_50_1rpmset_cf += (alphas_1set[i + 1] - alphas_1set[i
    ]) * (Cf_2_array[i + 1] + Cf_2_array[i]) * 1 / 2
314     s_70_1rpmset_cf += (alphas_1set[i + 1] - alphas_1set[i
    ]) * (Cf_3_array[i + 1] + Cf_3_array[i]) * 1 / 2
315     s_90_1rpmset_cf += (alphas_1set[i + 1] - alphas_1set[i
    ]) * (Cf_4_array[i + 1] + Cf_4_array[i]) * 1 / 2
316     s_NTP_1rpmset_cf += (alphas_1set[i + 1] - alphas_1set[
    i]) * (Cf_5_array[i + 1] + Cf_5_array[i]) * 1 / 2
317
318
319 # second rpm set
320 for i in range(0, N_2set):
321     s_30_2rpmset_cd += (alphas_2set[i + 1] - alphas_2set[i
    ]) * (Cd_6_array[i + 1] + Cd_6_array[i]) * 1 / 2
322     s_50_2rpmset_cd += (alphas_2set[i + 1] - alphas_2set[i
    ]) * (Cd_7_array[i + 1] + Cd_7_array[i]) * 1 / 2
323     s_70_2rpmset_cd += (alphas_2set[i + 1] - alphas_2set[i
    ]) * (Cd_8_array[i + 1] + Cd_8_array[i]) * 1 / 2
324     s_90_2rpmset_cd += (alphas_2set[i + 1] - alphas_2set[i
    ]) * (Cd_9_array[i + 1] + Cd_9_array[i]) * 1 / 2
325     s_NTP_2rpmset_cd += (alphas_2set[i + 1] - alphas_2set[
    i]) * (Cd_10_array[i + 1] + Cd_10_array[i]) * 1 / 2
326
327     s_30_2rpmset_cf += (alphas_2set[i + 1] - alphas_2set[i
    ]) * (Cf_6_array[i + 1] + Cf_6_array[i]) * 1 / 2
328     s_50_2rpmset_cf += (alphas_2set[i + 1] - alphas_2set[i
    ]) * (Cf_7_array[i + 1] + Cf_7_array[i]) * 1 / 2
329     s_70_2rpmset_cf += (alphas_2set[i + 1] - alphas_2set[i
    ]) * (Cf_8_array[i + 1] + Cf_8_array[i]) * 1 / 2
330     s_90_2rpmset_cf += (alphas_2set[i + 1] - alphas_2set[i
    ]) * (Cf_9_array[i + 1] + Cf_9_array[i]) * 1 / 2
331     s_NTP_2rpmset_cf += (alphas_2set[i + 1] - alphas_2set[
    i]) * (Cf_10_array[i + 1] + Cf_10_array[i]) * 1 / 2
332
333
334 average_cd_1rpmset=[]
335 average_cd_2rpmset=[]
336 average_cf_1rpmset=[]
337 average_cf_2rpmset=[]
338
339 # Mean discharge coefficient
340
341 average_30_1rpmset_cd = s_30_1rpmset_cd/(b_1-a_1)
342 average_30_2rpmset_cd = s_30_2rpmset_cd/(b_1-a_1)
343 average_cd_1rpmset.append(average_30_1rpmset_cd)
```

```
344 average_cd_2rpmset.append(average_30_2rpmset_cd)
345
346 average_50_1rpmset_cd = s_50_1rpmset_cd/(b_1-a_1)
347 average_50_2rpmset_cd = s_50_2rpmset_cd/(b_1-a_1)
348 average_cd_1rpmset.append(average_50_1rpmset_cd)
349 average_cd_2rpmset.append(average_50_2rpmset_cd)
350
351 average_70_1rpmset_cd = s_70_1rpmset_cd/(b_1-a_1)
352 average_70_2rpmset_cd = s_70_2rpmset_cd/(b_1-a_1)
353 average_cd_1rpmset.append(average_70_1rpmset_cd)
354 average_cd_2rpmset.append(average_70_2rpmset_cd)
355
356 average_90_1rpmset_cd = s_90_1rpmset_cd/(b_1-a_1)
357 average_90_2rpmset_cd = s_90_2rpmset_cd/(b_1-a_1)
358 average_cd_1rpmset.append(average_90_1rpmset_cd)
359 average_cd_2rpmset.append(average_90_2rpmset_cd)
360
361 average_NTP_1rpmset_cd = s_NTP_1rpmset_cd/(b_1-a_1)
362 average_NTP_2rpmset_cd = s_NTP_2rpmset_cd/(b_1-a_1)
363 average_cd_1rpmset.append(average_NTP_1rpmset_cd)
364 average_cd_2rpmset.append(average_NTP_2rpmset_cd)
365
366 # Mean flow coefficient
367
368 average_30_1rpmset_cf = s_30_1rpmset_cf/(b_1-a_1)
369 average_30_2rpmset_cf = s_30_2rpmset_cf/(b_1-a_1)
370 average_cf_1rpmset.append(average_30_1rpmset_cf)
371 average_cf_2rpmset.append(average_30_2rpmset_cf)
372
373 average_50_1rpmset_cf = s_50_1rpmset_cf/(b_1-a_1)
374 average_50_2rpmset_cf = s_50_2rpmset_cf/(b_1-a_1)
375 average_cf_1rpmset.append(average_50_1rpmset_cf)
376 average_cf_2rpmset.append(average_50_2rpmset_cf)
377
378 average_70_1rpmset_cf = s_70_1rpmset_cf/(b_1-a_1)
379 average_70_2rpmset_cf = s_70_2rpmset_cf/(b_1-a_1)
380 average_cf_1rpmset.append(average_70_1rpmset_cf)
381 average_cf_2rpmset.append(average_70_2rpmset_cf)
382
383 average_90_1rpmset_cf = s_90_1rpmset_cf/(b_1-a_1)
384 average_90_2rpmset_cf = s_90_2rpmset_cf/(b_1-a_1)
385 average_cf_1rpmset.append(average_90_1rpmset_cf)
386 average_cf_2rpmset.append(average_90_2rpmset_cf)
387
388 average_NTP_1rpmset_cf = s_NTP_1rpmset_cf/(b_1-a_1)
389 average_NTP_2rpmset_cf = s_NTP_2rpmset_cf/(b_1-a_1)
```

```
390 average_cf_1rpmset.append(average_NTP_1rpmset_cf)
391 average_cf_2rpmset.append(average_NTP_2rpmset_cf)
392
393 average_1rpmset_total_cd_array = np.asarray(
    average_cd_1rpmset)
394 average_1rpmset_total_cf_array = np.asarray(
    average_cf_1rpmset)
395
396 average_2rpmset_total_cd_array= np.asarray(
    average_cd_2rpmset)
397 average_2rpmset_total_cf_array = np.asarray(
    average_cf_2rpmset)
398
399 # creates an excel file and writes to it
400
401 OutWorkbook = xlsxwriter.Workbook("Average_coefficients.
    xlsx")
402
403 OutSheet = OutWorkbook.add_worksheet()
404
405 # Selects the header to be written to the excel file
    depending on the rpm set analyzed
406
407 if begin_2 == 1:
408     OutSheet.write("A1", "Mean discharge coefficient  in
    relation to the camshaft angle (5rpm)")
409     OutSheet.write("B1", "Mean flow coefficient in
    relation to the camshaft angle (5rpm) ")
410     OutSheet.write("C1", "Mean discharge coefficient in
    relation to the camshaft angle (20rpm)")
411     OutSheet.write("D1", "Mean flow coefficient in
    relation to the camshaft angle (20rpm) ")
412
413
414 else:
415     if begin_2 == 2:
416         OutSheet.write("A1", "Mean discharge coefficient
    in relation to the camshaft angle (10rpm)")
417         OutSheet.write("B1", "Mean flow coefficient in
    relation to the camshaft angle (10rpm) ")
418         OutSheet.write("C1", "Mean discharge coefficient
    in relation to the camshaft angle (15rpm)")
419         OutSheet.write("D1", "Mean flow coefficient in
    relation to the camshaft angle (15rpm) ")
420
421
```

```
422
423  # writes the values of discharge and flow coefficient to
    the excel file
424
425 for p in range(0,5):
426     OutSheet.write(p + 1, 0,
    average_1rpmset_total_cd_array[p])
427     OutSheet.write(p + 1, 1,
    average_1rpmset_total_cf_array[p])
428     OutSheet.write(p + 1, 2,
    average_2rpmset_total_cd_array[p])
429     OutSheet.write(p + 1, 3,
    average_2rpmset_total_cf_array[p])
430
431 OutWorkbook.close()
432
433
434
435
436
437
438
439
440
441
442
443
444
445
446
447
448
```